

OBSERVATIONS OF ACCRETING PULSARS

LARS BILDSTEN,¹ DEEPTO CHAKRABARTY,² JOHN CHIU,³ MARK H. FINGER,^{4,5} DANNY T. KOH,³
 ROBERT W. NELSON,^{3,6} THOMAS A. PRINCE,³ BRADLEY C. RUBIN,^{4,7} D. MATTHEW SCOTT,^{4,5}
 MARK STOLLBERG,^{4,8} BRIAN A. VAUGHAN,³ COLLEEN A. WILSON,⁴ AND ROBERT B. WILSON⁴

Received 1997 February 5; accepted 1997 June 20

ABSTRACT

We summarize 5 years of continuous monitoring of accretion-powered pulsars with the Burst and Transient Source Experiment (BATSE) on the *Compton Gamma Ray Observatory*. Our 20–70 keV observations have determined or refined the orbital parameters of 13 binaries, discovered five new transient accreting pulsars, measured the pulsed flux history during outbursts of 12 transients (GRO J1744–28, 4U 0115+634, GRO J1750–27, GS 0834–430, 2S 1417–624, GRO J1948+32, EXO 2030+375, GRO J1008–57, A0535+26, GRO J2058+42, 4U 1145–619, and A1118–616), and also measured the accretion torque history during outbursts of six of those transients whose orbital parameters were also known. We have also continuously measured the pulsed flux and spin frequency for eight persistently accreting pulsars (Her X-1, Cen X-3, Vela X-1, OAO 1657–415, GX 301–2, 4U 1626–67, 4U 1538–52, and GX 1+4). Because of their continuity and uniformity over a long baseline, BATSE observations have provided new insights into the long-term behavior of accreting magnetic neutron stars. We have found that all accreting pulsars show stochastic variations in their spin frequencies and luminosities, including those displaying secular spin-up or spin-down on long timescales, which blurs the conventional distinction between disk-fed and wind-fed binaries. Pulsed flux and accretion torque are strongly correlated in outbursts of transient accreting pulsars but are uncorrelated, or even anti-correlated, in persistent sources. We describe daily folded pulse profiles, frequency, and flux measurements that are available through the *Compton Observatory Science Support Center* at NASA/Goddard Space Flight Center.

Subject headings: accretion, accretion disks — binaries: close — pulsars: general — stars: magnetic fields — stars: neutron — X-rays: stars

CONTENTS

1. Introduction	367	6. Summary	398
2. Pulsar Detection and Study with BATSE	368	Appendix A: Pulsed Observations with BATSE	399
3. Overview of Accretion-powered Pulsars	371	A1. Background Subtraction	401
4. BATSE Observations of Individual Sources	375	A2. Optimal Combination of Detectors	402
4.1. Low-Mass Systems	377	Appendix B: BATSE Data Analysis	403
4.2. High-Mass Supergiant Systems	381	B1. Frequency Estimation	403
4.3. High-Mass Transient Systems	383	B1.1. Frequency Estimation using Power Spectra	403
5. Discussion	389	B1.2. Frequency Estimation using Epoch Folding	404
5.1. The Long-Term Spin Evolution of Disk-fed Pulsars	389	B1.3. Frequency Estimation from Fits to Pulse-Phase Measurements	404
5.2. Torque and Luminosity of Transient Pulsars	390	B2. Pulsed Flux Estimation	405
5.3. Accretion Torques in Transient and Wind-fed Pulsars	391	B2.1. What Is Pulsed Flux and Pulsed Fraction?	405
5.4. Power Spectra of Torque Fluctuations	392	B2.2. Peak-to-Peak Pulsed Spectra and Flux	405
5.5. Transients Outbursts in Be Systems	394	B2.3. Daily RMS Flux	405
5.6. The Population of Be Transients	395	References	406
5.7. Be/X-ray Pulsar Orbits	396		

¹ Department of Physics and Department of Astronomy, University of California, Berkeley, Berkeley, CA 94720; bildsten@fire.berkeley.edu.

² Center for Space Research, Massachusetts Institute of Technology, Cambridge, MA 02139; deepcto@space.mit.edu.

³ Space Radiation Laboratory, California Institute of Technology, Pasadena, CA 91125; chiu@srl.caltech.edu, koh@srl.caltech.edu, nelson@tapir.caltech.edu, prince@srl.caltech.edu, brian@srl.caltech.edu.

⁴ Space Science Laboratory, NASA/Marshall Space Flight Center, ES84, Huntsville, AL 35812; finger@gibson.msfc.nasa.gov, rubin@crab.riken.go.jp, scott@gibson.msfc.nasa.gov, stollberg@gibson.msfc.nasa.gov, wilsonc@ssl.msfc.nasa.gov, wilson@gibson.msfc.nasa.gov.

⁵ Universities Space Research Association.

⁶ Theoretical Astrophysics 130-33, California Institute of Technology, Pasadena, CA 91125.

⁷ Current address: Cosmic Radiation Laboratory, Institute for Physical and Chemical Research (RIKEN), Wako-shi, Saitama 351-01, Japan.

⁸ Department of Physics, University of Alabama, Huntsville, AL 35899.

1. INTRODUCTION

Accreting X-ray pulsars were discovered over 25 years ago (Giacconi et al. 1971), and a qualitative description of both the accretion process and the origin of the pulsed emission was understood almost immediately (Pringle & Rees 1972; Davidson & Ostriker 1973; Lamb, Pethick, & Pines 1973). X-ray pulsars are rotating and strongly magnetized ($B \gtrsim 10^{11}$ G) neutron stars that accrete gas from a stellar companion. As the accreting material approaches the neutron star, the plasma is channeled to the magnetic polar caps, where it releases its gravitational energy as X- and γ -radiation; these rotating hot spots are the sources of the pulsed emission. Despite more than two decades of study, however, many details of this scenario remain poorly understood.

The accreting pulsars are also important evolutionary links to other binary systems containing neutron stars. Some young neutron stars with high-mass companions may begin their lives as rotation-powered radio pulsars (Johnston et al. 1992; Kaspi et al. 1994) and become bright X-ray sources only during episodes of significant mass transfer later in life. On the other hand, there is some evidence that extended episodes of accretion onto neutron stars with low-mass companions can cause their magnetic fields to decay (Bhattacharya & Srinivasan 1995). If the inner accretion disk can then extend nearly down to the stellar surface, these neutron stars should spin up to millisecond rotation periods (Alpar et al. 1982); there is mounting evidence that the low-mass X-ray binaries contain rapidly rotating neutron stars (see, for example, Strohmayer et al. 1996) and are the birthplace of the millisecond radio pulsars. Perhaps most importantly, the qualitative picture developed in the early 1970s to explain the behavior of X-ray pulsars has become the paradigm for accretion onto other types of magnetic stars, such as magnetic cataclysmic variables (CVs) and T Tauri stars (Warner 1990; König 1991). It is thus becoming increasingly important that the standard picture of X-ray pulsars developed more than 20 years ago be tested critically.

Much of our understanding of accretion-powered pulsars originates from accurate timing of the pulsed emission. Just as in binary radio pulsars, the orbital motion causes a modulation in the observed pulse frequency, which allows measurement of the binary orbital parameters. The small moment of inertia of a neutron star makes it possible to measure the intrinsic changes in the pulsar spin frequency caused by angular momentum gained (or lost) during the accretion process on timescales of approximately days. This can potentially reveal the nature of the accretion flow—a persistent trend in the spin frequency indicates the presence of an accretion disk, while short-term changes with no persistent trend are usually indicative of a wind-fed system. As of this writing, there are 44 known accreting pulsars in our Galaxy and the Magellanic Clouds, with spin periods ranging from 0.069 s through 1413 s. Approximately half of these objects are observed only during episodes of transient accretion.

The physics and astronomy of accretion-powered pulsars have been reviewed previously. White, Nagase, & Parmar (1995) reviewed accreting X-ray binaries in general. Nagase (1989) reviewed observations of accreting pulsars. Hayakawa (1985) provided a theoretical overview of accretion physics and spectral formation in strong magnetic fields. Joss & Rappaport (1984) reviewed neutron stars in binaries. White, Swank, & Holt (1983) presented energy spectra and pulse profiles. Rappaport & Joss (1977a, 1977b) reviewed the “standard model” for accretion torques and pulse profiles.

In this paper we summarize over 5 years of observations of accreting binary pulsars with the all-sky BATSE instrument on the *Compton Gamma Ray Observatory*. BATSE’s principal advantage over previous instruments for studying accreting pulsars is its continuous monitoring capability. The timing data we present here represents a ~ 100 -fold increase in the time resolution of spin frequency histories of persistent pulsars and the first long-term, spatially uniform monitoring program for the detection of new pulsars and recurrent transients. We have detected and studied nearly half of the known accreting pulsars and determined

accurate orbital parameters for 13 of these systems. Table 1 lists all known accreting pulsars along with their positions in galactic coordinates, spin and orbital periods, and companion type (where known).

BATSE’s continuous timing of X-ray pulsars gives the neutron star spin period history over timescales of days to years and is ideally suited for detailed studies of the accretion torque. Our observations give a qualitatively different picture of the spin behavior of disk-fed pulsars on long timescales (\sim years) than understood from pre-BATSE measurements (see Nagase 1989 and references therein). Moreover, BATSE has been able to test theories of accretion torque on short timescales (\sim days). This has led to several unexpected discoveries in disk-fed pulsars: (1) the transition between spin-up and spin-down in 4U 1626–67 (Chakrabarty et al. 1997a) and Cen X-3, (2) anticorrelated behavior of torque and luminosity in GX 1+4 (Chakrabarty et al. 1997b), and (3) evidence that transient accretion disks sometimes form in GX 301–2 (Koh et al. 1997). By monitoring these changes along with variations in the pulsed luminosity, we may be able to learn about the complex interaction between the magnetosphere and the accretion flow—physics that is at work in a broad variety of accreting systems but can only be measured dynamically in accretion-powered pulsars.

Five of the 13 transient systems detected by BATSE are new binaries. Combining these discoveries with the “recovery” of previously known transients yields new information on the population and typical distance of these sources. In addition to the recent discovery that the bursting transient GRO J1744–28 is a 2 Hz pulsar (Finger et al. 1996a), the discovery of quasi-periodic oscillations in the accreting transient A0536+26 (Finger, Wilson, & Harmon 1996c) gave us the best evidence yet for periodic phenomena originating from the magnetospheric radius.

Section 2 outlines how we take maximum advantage of the BATSE instrument by actively processing the standard data sets (DISCLA and CONT). We also summarize our data analysis methods and give our typical flux sensitivity as a function of spin period. Appendices A and B contain additional details about our data analysis technique. A summary and brief review of the science that can be done by pulse timing of accreting pulsars is provided in § 3. Section 4 presents a synopsis of BATSE observations with frequency and flux histories for each accreting pulsar we detected. We also provide pointers to the literature where more details can be found. Section 5 is a discussion of how the BATSE observations have changed our understanding of the long-term spin evolution of accreting pulsars and the nature of transient sources. We conclude in § 6 with a brief summary of our primary discoveries.

2. PULSAR DETECTION AND STUDY WITH BATSE

The BATSE detectors have provided unprecedented continuous all-sky monitoring for both pulsed and unpulsed sources above 20 keV since 1991. This section briefly summarizes our methods and describes the resulting flux sensitivity as a function of pulse frequency. This is the most crucial quantity for determining the detection sensitivity for new sources and shapes our discussion in § 5 of what BATSE has learned about the populations of X-ray transients.

BATSE consists of eight detector modules facing outward from the corners of the *CGRO* spacecraft. Each

TABLE 1
KNOWN ACCRETION-POWERED PULSARS (AS OF 1997 FEBRUARY)

System	Discovered/ Detected ^a	l_{II}	b_{II}	P_{spin} (s)	$P_{\text{orb}}^{\text{b}}$ (days)	Companion (MK Type)	References
Low-Mass Binaries							
GRO J1744–28	Dis	0.0	+0.3	0.467	11.8		1
Her X-1	Det	58.2	+37.5	1.24	1.70	HZ Her (A9-B)	2, 3
4U 1626–67	Det	321.8	–13.1	7.66	0.0289	KZ TrA (low-mass dwarf)	4, 5
4U 1728–247 (GX 1+4)	Det	1.9	+4.8	120		V2116 Oph (M6 III)	6, 7
High-Mass Supergiant and Giant Systems							
SMC X-1		300.4	–43.6	0.717	3.89	Sk 160 (B0 I)	8
Cen X-3	Det	292.1	+0.3	4.82	2.09	V779 Cen (O6–8f)	9, 10
RX J0648.1–4419		253.7	–19.1	13.2	1.54	HD 49798 (O6p)	11
LMC X-4		276.3	–32.5	13.5	1.41	Sk-Ph (O7 III–V)	12
OAO 1657–415	Det	344.4	+0.3	37.7	10.4	(B0–6 Iab)	13
Vela X-1	Det	263.1	+3.9	283	8.96	HD 77581 (B0.5 Ib)	14
1E 1145.1–6141		295.5	–0.0	297		V830 Cen (B2 Iae)	15
4U 1907+09		43.7	+0.5	438	8.38	(B I)	16
4U 1538–52	Det	327.4	+2.1	530	3.73	QV Nor (B0 Iab)	17, 18
GX 301–2	Det	300.1	–0.0	681	41.5	Wray 977 (B1.5 Ia)	19, 20
Transient Be-Binary Systems							
A0538–67		276.9	–32.2	0.069	16.7	(B2 III–IVe)	21
4U 0115+63	Det	125.9	+1.0	3.61	24.3	V635 Cas (Be)	22, 23
V0332+53		146.1	–2.2	4.37	34.2	BQ Cam (Be)	24
2S 1417–624	Det	313.0	–1.6	17.6	42.1	(OBe)	25
EXO 2030+375	Det	77.2	–1.3	41.7	46.0	(Be)	26, 27
GRO J1008–57	Dis	283.0	–1.8	93.5	≈248	(Be)	28, 29
A0535+26	Det	181.4	–2.6	105	110	HDE 245770 (O9.7 IIe)	30
GX 304–1		302.1	+1.2	272	133 (?)	V850 Cen (B2 Vne)	31
4U 1145–619	Det	295.6	–0.2	292	187	Hen 715 (B1 Vne)	32
A1118–616	Det	292.5	–0.9	405		He 3-640 (O9.5 III–Ve)	33
4U 0352+309		163.1	–17.1	835		X Per (O9 III–Ve)	34
RX J0146.9+6121		129.9	–0.5	1413		LS I+61° 235 (B5 IIIe)	35
Persistent Systems with an Undetermined Companion							
RX J1838.4–0301		28.8	+1.5	5.45			36
1E 1048–593		288.2	–0.5	6.44			37
1E 2259+586		109.1	–1.0	6.98			38
RX J0720.4–3125		244.2	–8.2	8.38			39
4U 0142+614		129.4	–0.4	8.69			40
Transient Systems with an Undetermined Companion							
RX J0059.2–7138 ^c	Det	302.1	–45.5	2.76			41
RX J0502.9–6626		277.0	–35.5	4.06			42
GRO J1750–27	Dis	2.4	+0.5	4.45	29.8		43
2E 0050.1–7247		302.9	–44.6	8.9			11
2S 1553–54		327.9	–0.9	9.26	30.6		44
GS 0834–430	Det	262.0	–1.5	12.3	106		45, 46
GRO J1948+32	Dis	64.9	1.8	18.7			47
GS 1843+00		33.1	+1.7	29.5			48
GS 2138+56 (Cep X-4?)		99.0	+3.3	66.2			49
GS 1843–024		30.2	–0.0	94.8			50
Sct X-1		24.5	–0.2	111			51
GRO J2058+42	Dis	83.6	–2.7	198	≈110		52, 53
GPS 1722–363		351.5	–0.6	414			54

^a Sources marked Det have been detected with BATSE; sources marked Dis were discovered by BATSE.

^b In those cases in which no orbital parameters are given in Table 3, the orbital period has been inferred from pulse timing and/or outburst recurrence times and/or optical photometry.

^c This source was detected by both BATSE and *ROSAT* on MJD 49,120. It has not been studied with BATSE and is not discussed in this paper.

REFERENCES.—(1) Finger et al. 1996a; (2) Deeter et al. 1991; (3) Wilson et al. 1994a; (4) Chakrabarty et al. 1997a; (5) Middleditch et al. 1981; (6) Chakrabarty et al. 1997b; (7) Makishima et al. 1988; (8) Levine et al. 1993; (9) Finger et al. 1993; (10) Nagase et al. 1992; (11) Israel et al. 1995; (12) Safi-Harb, Ögelman, & Dennerl 1996; (13) Chakrabarty et al. 1993; (14) Deeter et al. 1987; (15) Ilovaisky, Chevalier, & Motch 1982; (16) Makishima et al. 1984; (17) Rubin et al. 1994; (18) Corbet et al. 1993; (19) Koh et al. 1997; (20) Sato et al. 1986; (21) Skinner 1981; (22) Cominsky, Roberts, & Finger 1994; (23) Rappaport et al. 1978; (24) Stella et al. 1985; (25) Finger et al. 1996b; (26) Stollberg et al. 1994; (27) Parmar et al. 1989; (28) Wilson et al. 1994b; (29) Coe et al. 1994a; (30) Finger et al. 1996c; (31) Priedhorsky & Terrell 1983; (32) Cook & Warwick 1987; (33) Ives et al. 1975; (34) Murakami et al. 1987; (35) Hellier 1994; (36) Schwentker 1994; (37) Seward, Charles, & Smale 1986; (38) Iwasawa, Koyama, & Halpern 1992; (39) Haberl et al. 1996; (40) Israel, Mereghetti, & Stella 1994; (41) Hughes 1994; (42) Schmidtke et al. 1995; (43) Scott et al. 1997; (44) Kelley, Rappaport, & Ayasli 1983; (45) Wilson et al. 1997; (46) Aoki et al. 1992; (47) Chakrabarty et al. 1995a; (48) Koyama et al. 1990a; (49) Koyama et al. 1991a; (50) Koyama et al. 1990b; (51) Koyama et al. 1991b; (52) Wilson et al. 1996; (53) Wilson et al. 1995a; (54) Tawara et al. 1989.

module contains a large area detector (LAD) (with geometric area of 2025 cm² and an energy range of 20–1800 keV) and a smaller spectroscopy detector. The LADs are non-imaging NaI(Tl) scintillators with 2π sr fields of view. Our pulsar studies primarily use the background data from these detectors, which are folded on board or available continuously at 1.024 s time resolution with four energy channels (DISCLA data) and at 2.048 s time resolution with 16 energy channels (CONT data). The large field of view allows for multiple contributions to the background, which varies by factors of 2 during each ≈ 93 minute satellite orbit. Figure 1 shows a selected orbit of DISCLA data from a single BATSE LAD detector. The large pulses every 141.5 s are from the bright accreting pulsar Vela X-1 [$P_{\text{spin}} = 283.2185(18)$ s on this day], which has a double-peaked pulse profile. Very few sources are persistently bright enough to observe directly in this ≈ 2000 counts s⁻¹ background.

Accreting pulsars are typically detected in the lowest DISCLA channel, covering 20–50 keV, and in CONT channels 1–4, typically covering 20–70 keV, with detections sometimes extending to energies as high as 160 keV. In this sense, BATSE is measuring only the high-energy spectral tails of accreting pulsars. Often, most of the flux from these objects is at lower energies, so that our flux measurements are subject to a large (and often unknown) bolometric correction. The pulsed flux histories we provide thus reflect the history of the bolometric luminosity only when the overall

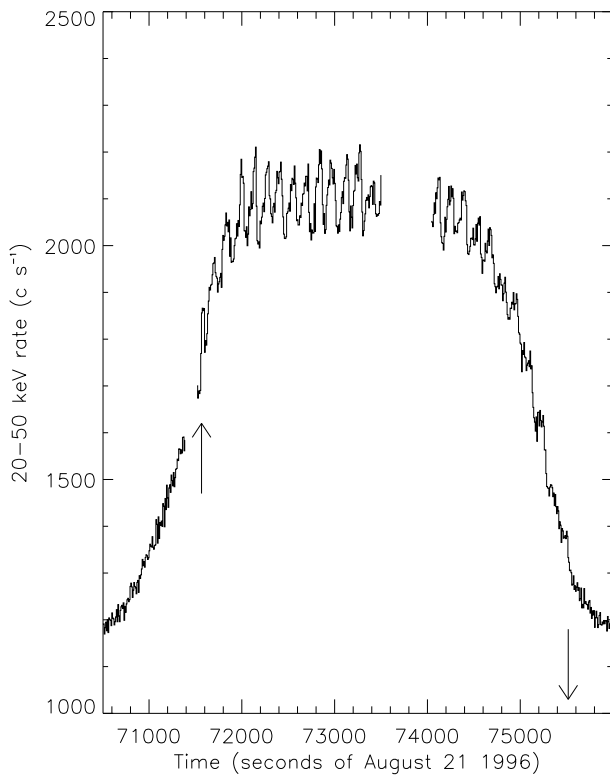


FIG. 1.—DISCLA data from a single BATSE detector for a full spacecraft orbit. The rates are from the 20–50 keV channel of Large Area Detector 2, on 1996 August 21 when Vela X-1 was in a high state. Shown are 8.2 s average rates, with errors < 16 counts s⁻¹. The 800 counts s⁻¹ modulation is due to the difference between the cosmic diffuse background and the diffuse background from Earth's atmosphere. The lowest rates are when the detector mainly sees Earth, while at the highest rates, it sees the sky. The data gaps are due to a loss of telemetry. Vela X-1 rises above the horizon at 71,566 s and sets at 75,517 s, as noted by the arrows.

spectral shape and the pulsed fraction in the BATSE energy band are independent of time.

The signal C_S (in counts s⁻¹) in the BATSE detectors from most accreting pulsars is 10^2 – 10^3 times smaller than the background count rate C_B , so that a Fourier or epoch-folding analysis proves to be the best way to detect them. For pulse periods shorter than a few minutes, the signal-to-noise ratio (S/N) for an observation of length t is just governed by the Poisson variations of the background, $S/N \propto C_S t / (C_B t)^{1/2}$. The background variations on timescales longer than a few minutes are mostly due to the satellite orbit and other effects (see Appendix A) and hence exceed the Poisson variations. Our sensitivity for detecting long-period pulsars would be substantially degraded if nothing was done to remedy this. Our solution (presented in Appendix A) is to fit a phenomenological model to these background variations and subtract it prior to scientific analysis. Though this does not bring the sensitivity down to the Poisson level at all frequencies (see Fig. 41 in Appendix A), it is a great improvement relative to the raw count rates.

The resulting 1 day pulsed-intensity sensitivities of the CONT data as a function of energy are shown in Figure 2 for three representative pulse frequencies. The upper panel

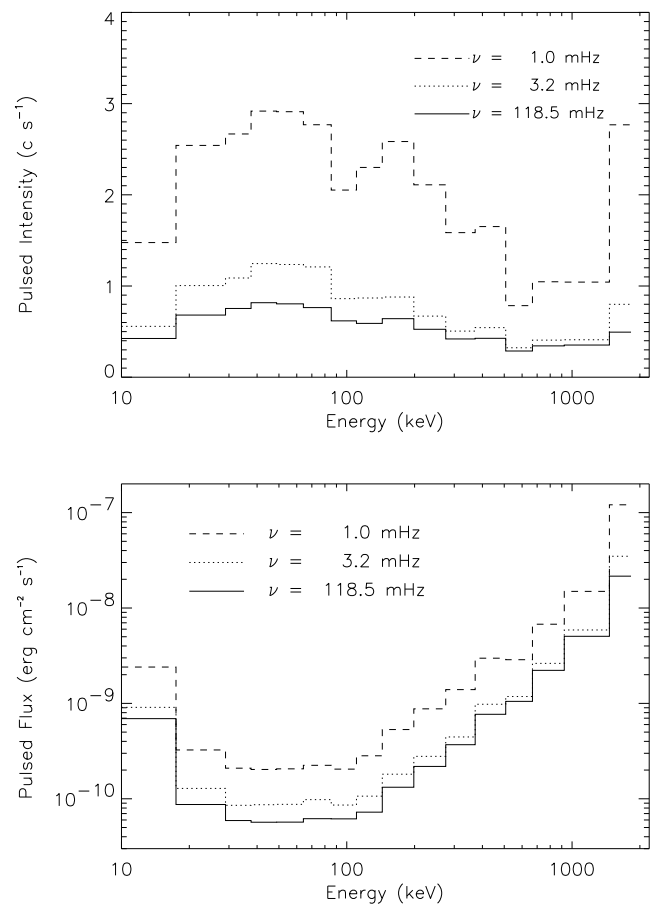


FIG. 2.—The 1 day BATSE sensitivity for a single large-area detector to an unocculted pulsed source at three pulse frequencies. We define the threshold pulsed intensity (*upper panel*) as the count rate where the error in the measured rate is 20%. The degradation in sensitivity at low frequencies is due to residual background not fully accounted for by the background subtraction process. The lower panel shows the energy flux corresponding to these threshold count rates, assuming that the source has a power-law spectrum with photon number index $\alpha = 4.0$ and is viewed at normal incidence. A typical live time of $\sim 42,000$ s is obtained per day.

shows the minimum count rate needed so that the count rate of the pulse is found to within 20% accuracy. This is a more stringent criterion than that for detecting the pulse in a narrow frequency range. As is evident from the figure, the excess noise at low frequencies strongly reduces our sensitivity to long-period pulsars. The lower panel is the resulting pulsed flux assuming that the pulsar has a power-law energy spectrum with index $\alpha = 4$ (see the figure legend). Most of our searches are carried out with combinations of various channels. Figure 3 shows the 1 day sensitivity in a single detector for the sum of CONT channels 1–4. When Poisson-limited, the resulting sensitivity to a pulsed source of high frequencies is

$$C_s \approx 1.1 \text{ counts s}^{-1} \left(\frac{C_B}{2000 \text{ counts s}^{-1}} \right)^{1/2} \left(\frac{42,000 \text{ s}}{t} \right)^{1/2}. \quad (1)$$

Depending on how steep the spectrum is (see Table 2 for the conversion from BATSE LAD counts s^{-1} to flux units) this is a flux of $\approx 10^{-10} \text{ ergs cm}^{-2} \text{ s}^{-1}$ in the 20–60 keV band. The corresponding luminosity at the Galactic center (8.5 kpc) is $L(20\text{--}60 \text{ keV}) \approx 8 \times 10^{35} \text{ ergs s}^{-1}$, which allows for detection of the majority of the known accreting pulsars. For the purposes of comparison, the 1 day sensitivity for detection using occultation steps is about 10 counts s^{-1} (Harmon et al. 1992), a factor of 10 worse than the pulsed sensitivity. This is basically due to the difference in effective exposure time in 1 day for both methods.

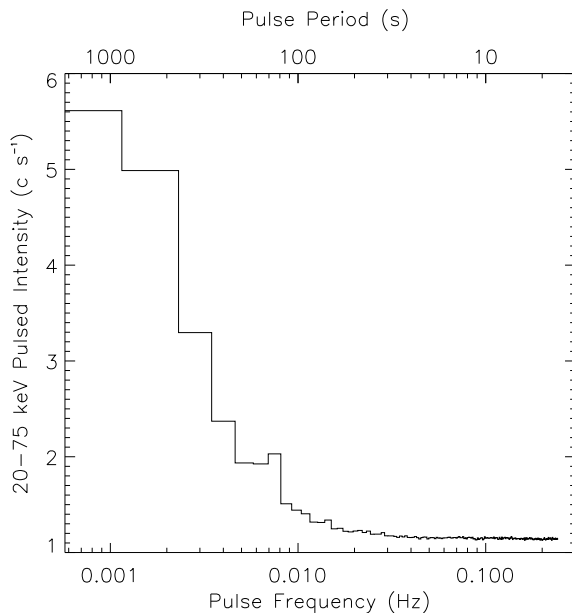


FIG. 3.—The 1 day BATSE 5σ detection threshold for an unocculted source (CONT channels 1–4 summed) following background subtraction. The thresholds plotted were obtained by averaging the thresholds for each of the eight BATSE detectors from MJD 49,081 to 49,093. A typical day is characterized by a mean background rate (CONT channels 1–4 summed) of $\approx 2000 \text{ counts s}^{-1}$ and $\approx 42,000 \text{ s}$ of useful data. At frequencies $\nu \gtrsim 0.02 \text{ Hz}$, the background noise is essentially Poisson, and the threshold is simply that given by eq. (1). The thresholds at lower frequencies are found by assuming local Gaussian statistics for the measured noise strength. The anomalous rise in the thresholds at $\nu \approx 0.007 \text{ Hz}$ is attributable to the second harmonic of Vela X-1, which was not accounted for in the background subtraction model.

TABLE 2
CONVERSION TO PULSED FLUX FROM COUNTS

Power Law			
α^a	DISCLA ^b	CONT ^c	Percentage of Error ^d
2.0.....	0.84	0.79	5
3.0.....	0.94	0.87	10
4.0.....	1.05	0.95	15
5.0.....	1.17	1.02	20
OTTB			
kT (keV) ^e	DISCLA ^b	CONT ^c	Percentage of Error ^d
10.....	1.18	1.03	15
25.....	0.94	0.88	8
40.....	0.89	0.84	6
55.....	0.87	0.82	5

NOTE.—These conversions are for normal incidence. For other incident photon angles, see Appendix A and Fig. 42

^a Spectral model used is $dN/dE \propto E^{-\alpha}$.

^b Energy flux in units of $10^{-10} \text{ ergs cm}^{-2} \text{ s}^{-1}$ corresponding to a pulsed intensity of 1 count s^{-1} in DISCLA Channel 1 (20–50 keV).

^c Energy flux in units of $10^{-10} \text{ ergs cm}^{-2} \text{ s}^{-1}$ corresponding to a pulsed intensity of 1 count s^{-1} in CONT Channels 1–4 (20–70 keV) summed.

^d Percentage of error in energy flux due to variations in energy edges for different detectors.

^e Spectral model used is $dN/dE \propto (1/E) \exp(-E/kT)g_{\text{ff}}(E, kT)$.

We have performed a uniform, standard analysis on all pulsars viewable with BATSE that have spin periods longer than about 4 s, the Nyquist frequency of the CONT data. Power spectra are computed using the fast Fourier transform for a daily estimate of the spin frequency ν of each system, followed by epoch folding at ν for a daily pulse profile. The profiles are then used to determine the pulsed count rate in each CONT energy channel, which are then fitted with standard models to determine the spectral shape and pulsed flux (see Appendix B). These folded profiles form the basis of detailed timing studies. Frequency, pulsed flux, and folded pulse profile histories generated by this analysis are available from the BATSE pulsed source database at the *Compton Observatory* Science Support Center. This database forms the basis of many of the figures displayed in this paper. For systems with spin periods comparable to or shorter than 4 s (GRO J1744–28 [0.467 s], Her X-1 [1.24 s], 4U 0115+63 [3.6 s], GRO J1750–27 [4.4 s], and Cen X-3 [4.8 s]), we utilize a combination of DISCLA and folded-on-board data, also described in Appendix B.

3. OVERVIEW OF ACCRETION-POWERED PULSARS

The discovery of orbitally modulated, periodic X-ray pulsations from Cen X-3 by *Uhuru* (Giacconi et al. 1971; Schreier et al. 1972) quickly led to a qualitative understanding of X-ray pulsars as rotating magnetized neutron stars accreting matter from a binary companion (Pringle & Rees 1972; Davidson & Ostriker 1973; Lamb et al. 1973). The neutron star accretes matter either by capturing material from the stellar wind of the companion or through Roche lobe overflow of the mass-donating star. The strong surface magnetic field (typically $B \sim 10^{12} \text{ G}$) controls the accretion flow close to the neutron star, where, in the simplest picture,

the ionized matter follows the field lines onto the magnetic poles. The resulting accretion luminosity from the polar regions is

$$L_{\text{acc}} = \frac{GM_{\text{x}}\dot{M}}{R_{\text{x}}} \simeq 1.2 \times 10^{36} \text{ ergs s}^{-1} \times \left(\frac{\dot{M}}{10^{-10} M_{\odot} \text{ yr}^{-1}} \right) \left(\frac{M_{\text{x}}}{1.4 M_{\odot}} \right) \left(\frac{10 \text{ km}}{R_{\text{x}}} \right), \quad (2)$$

where \dot{M} is the instantaneous mass accretion rate, and M_{x} and R_{x} are the neutron star mass and radius. Both the misalignment of the rotation axis with the dipolar field and asymmetric emission from the accreting polar cap lead to pulsed emission at the neutron star spin period. Many of these accreting pulsars were known and studied prior to the launch of the BATSE instrument, and this section is mostly an overview of the “standard” picture of these objects developed with pre-BATSE observations. We discuss, in § 5, how our understanding of accreting pulsars has been reshaped by BATSE observations.

The simple blackbody temperature estimate (i.e., $L_{\text{acc}} = A_{\text{cap}} \sigma_{\text{SB}} T_{\text{eff}}^4$, where $A_{\text{cap}} \sim \text{km}^2$ is the typical polar cap area) gives $kT_{\text{eff}} \sim 3 \text{ keV}$, comparable to where the peak in νF_{ν} usually appears in the X-ray spectrum. The observed 2–100 keV X-ray spectra are much harder than a blackbody and have been represented by a variety of models, most commonly a power law with an exponential cutoff or a broken power law (see, e.g., White et al. 1983; Mihara 1995). The exponential cutoff energy falls in the 5–25 keV range, while the power-law photon index is typically $\alpha \lesssim 1.5$ below the cutoff energy. It is the hard power-law tail that we typically detect with the BATSE instrument. The pulse profiles of accreting pulsars are relatively smooth and simple (i.e., single- or double-peaked) above 20 keV. The pulsed fraction (see Appendix B, § B2) is typically greater than 50% and normally increases with photon energy (see Fig. 7 for examples of pulse profiles in the BATSE energy range). The pulse profiles at lower energies are generally more complex (see White et al. 1983 for examples).

Table 1 shows the presently known accreting pulsars, which are generally classified according to the mass of the donor star as either *low-mass* ($M_c \lesssim 2.5 M_{\odot}$) or *high-mass* ($M_c \gtrsim 6 M_{\odot}$) systems (Shore, Livio, & van den Heuvel 1994). Systems that have been detected by BATSE are marked “Det.,” and those discovered by BATSE are marked “Dis.” Table 3 shows the presently known orbital parameters. There are only four known low-mass binaries with accreting pulsars: Her X-1, 4U 1626–67, GX 1+4, and GRO J1744–28. The overwhelming majority of low-mass X-ray binaries are not pulsars and thus evidently have fields too weak to strongly affect the accretion flow ($B \lesssim 10^9 \text{ G}$). The high-mass binaries may be divided into those with main-sequence Be star companions and those with evolved OB supergiant companions. The Be systems, which account for more than half of the known accreting pulsars, are generally observed during transient outbursts. The mass donor in these systems is an O or B star still on the main sequence and lying well inside its Roche surface. The episodic outbursts are often correlated with periastron passage of the neutron star in its eccentric orbit. These systems are thought to undergo a “propeller” phase during X-ray quiescence (Stella, White, & Rosner 1986).

The supergiant binaries may be further subdivided into two groups according to the dominant mode of mass transfer: Roche lobe overflow or capture from the stellar wind. In some systems, both types of mass transfer may be taking place (Blondin, Stevens, & Kallman 1991). Most OB supergiants have stellar winds driven by the radiation pressure from resonance lines of highly ionized atoms, with mass loss rates of $\dot{M} \sim 10^{-6} M_{\odot} \text{ yr}^{-1}$ being quite typical. Although capture from a high-velocity wind is inefficient, the large mass-loss rate in the wind can result in an appreciable mass accretion rate onto the neutron star. Vela X-1 is the best known example of a wind-fed supergiant pulsar binary.

If the mass donor fills its Roche lobe, material from the companion flows with high specific angular momentum through the first Lagrange point and forms an accretion disk around the neutron star. This is a very efficient form of accretion and results in a mass transfer rate much larger than by capture of the wind alone. The large persistent accretion rates in SMC X-1, Cen X-3, and LMC X-4 make them prime candidates for disk-fed (via Roche lobe overflow) supergiant pulsar binaries. Optical photometric observations of these systems show both ellipsoidal variations consistent with a tidally distorted companion and excess light owing to the presence of an accretion disk (van Paradijs & McClintock 1995 and references therein). As we discuss later, the accretion torque magnitude and temporal behavior is also indicative of accretion from a Keplerian disk.

A convenient organization of the high-mass systems emerges by plotting those with known orbital periods on a $P_{\text{spin}}-P_{\text{orb}}$ diagram (Corbet 1986; Waters & van Kerkwijk 1989), where P_{spin} is the neutron star spin period. As is evident in Figure 4, the neutron stars orbiting Roche lobe-filling supergiants (*asterisks*) have short spin periods ($P_{\text{spin}} \lesssim 10 \text{ s}$) and short orbital periods ($P_{\text{orb}} \lesssim 4 \text{ days}$). They are quite luminous ($L \gtrsim 10^{37} \text{ ergs s}^{-1}$) and tend to show

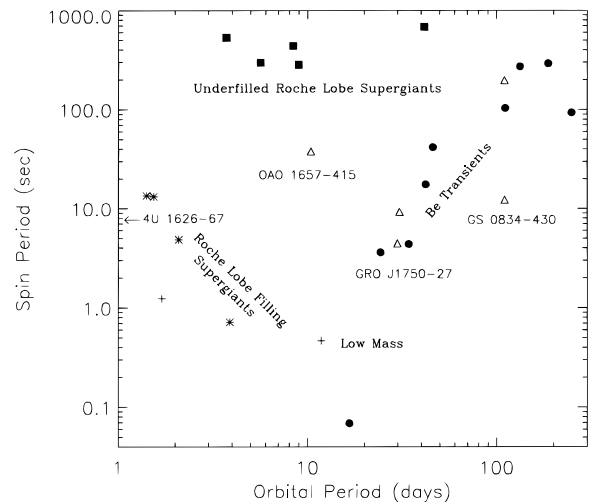


FIG. 4.—Spin period of the accreting neutron stars vs. the binary period (the Corbet diagram). The different symbols refer to the type of binary the neutron star resides in. Asterisks are supergiant companions that are Roche lobe filling, squares are supergiant companions that underfill their Roche lobe, circles are confirmed Be-transient binaries, and plus signs are those with low-mass ($\lesssim 2 M_{\odot}$) companions (Her X-1, GRO J1744–28, and 4U 1626–67). Triangles refer to sources for which the companion type is unknown, though the orbital period has been determined. (GS 0834–430, OAO 1657–415, GRO J1750–27, 2S 1553–54, and GRO J2058+42.)

TABLE 3
ORBITAL PARAMETERS OF ACCRETION-POWERED PULSAR SYSTEMS^a

Source Name	Orbital Epoch (MJD)	P_{orb} (days)	$a_x \sin i$ (lt-sec)	e	ω (deg)	$f_x(M)$ (M_{\odot})	References
Low-Mass Systems							
GRO J1744–28	50079.1552(18) ^b	11.8337(13)	2.6324(12)	$< 1.1 \times 10^{-3}$ (90%)	...	$1.3638(17) \times 10^{-4}$	1
Her X-1	48799.61235(1) ^b	1.700167412(40) ^c	13.1853(2)	$< 1.3 \times 10^{-4}$ (3 σ)	...	0.85145(4)	2, 3
High-Mass Supergiant Systems							
LMC X-4	47741.9904(2) ^b	1.40841(2) ^d	26.31(3)	0.006(2)	...	9.86(3)	4
Cen X-3	48561.656702(71) ^b	2.08706533(49) ^e	39.627(18)	$< 1.6 \times 10^{-3}$ (90%)	...	15.343(21)	5, 22
4U 1538–52	45625.719(18) ^b	3.72839(2) ^f	53.5(14)	< 0.058 (95%)	...	11.8(9)	6
SMC X-1	47740.35906(3) ^b	3.892116(1) ^g	53.4876(4)	$< 4 \times 10^{-5}$ (2 σ)	...	10.8481(2)	7
4U 1907+09	45578.75(35) ^b	8.3745(42)	80.2(72)	$0.16_{-0.11}^{+0.14}$	330_{-56}^{+18}	7.9(21)	8
Vela X-1	48895.2186(12) ^b	8.964368(40)	113.89(13)	0.0898(12)	152.59(92)	19.74(07)	9
OA0 1657–415	48515.99(5) ^b	10.44809(30) ^h	106.0(5)	0.104(5)	93(5)	11.7(2)	10, 11
GX 301–2	48802.79(12) ⁱ	41.498(2)	368.3(37)	0.462(14)	310.4(14)	31.1(9)	12
Be-Binary Systems							
4U 0115+63 ^j	49279.2677(34) ⁱ	24.317037(62)	140.13(8)	0.3402(2)	47.66(9)	5.00(1)	11, 13, 14
V0332+53	45651.5(10) ⁱ	34.25(10)	48(4)	0.31(3)	313(10)	0.10(2)	15
2S 1417–624	49713.62(5) ⁱ	42.12(3)	188(2)	0.446(2)	300.3(6)	3.9(1)	16
EXO 2030+375	48936.5(3) ⁱ	46.01(2)	264(21)	0.37(2)	223.4(39)	9.1(22)	17
A0535+26	49058.7(6) ⁱ	110.3(3)	267(13)	0.47(2)	130(5)	1.64(23)	18
System with Undetermined Companion							
2S 1553–54	42596.67(3) ^b	30.2(1)	162.7(10)	< 0.09 (2 σ)	...	5.0(1)	19
GRO J1750–27	49931.02(1) ⁱ	29.817(9)	101.8(5)	0.360(2)	206.3(3)	1.24(2)	20
GS 0834–430	48809.6(15) ^k	105.8(4)	128_{-38}^{+47}	$0.12_{-0.04}^{+0.05}$	140_{-53}^{+35}	$0.20_{-0.10}^{+0.30}$	21

^a All confidence intervals are quoted at the 1 σ level, except where noted. Epochs are quoted in TDB at the solar system barycenter. P_{orb} = orbital period, $a_x \sin i$ = projected semimajor axis, e = eccentricity, ω = longitude of periastron, and $f_x(M)$ = X-ray mass function.

^b $T_{\pi/2}$ = epoch of 90° mean orbital longitude.

^c Orbital period for specified orbital epoch, computed using $\dot{P}_{\text{orb}} = (-6.16 \pm 0.74) \times 10^{-11}$ days day⁻¹ from Deeter et al. 1991.

^d Orbital period for specified orbital epoch, computed using $\dot{P}_{\text{orb}} = (4.2 \pm 3.1) \times 10^{-9}$ days day⁻¹ from Levine et al. 1991.

^e $P_{\text{orb}} = (-9.93 \pm 0.02) \times 10^{-9}$ days day⁻¹ reported by Nagase et al. 1992.

^f Orbital period derivative constrained to -4.0×10^{-8} days day⁻¹ $< \dot{P}_{\text{orb}} < 2.1 \times 10^{-8}$ days day⁻¹ (95% confidence) by Rubin et al. 1997.

^g Orbital period for specified orbital epoch, computed using $\dot{P}_{\text{orb}} = (-3.58 \pm 0.02) \times 10^{-8}$ days day⁻¹ from Levine et al. 1993.

^h Revised orbital period from § 4, this work.

ⁱ T_0 = epoch of periastron passage.

^j $a_x \sin i$ and e are from Rappaport et al. 1978 and were held fixed by Cominsky et al. 1994. ω is from Cominsky et al. 1994. The epoch and P_{orb} are from § 4, this work.

^k $T_2 = T_0 - \omega P_{\text{orb}}(4\pi)^{-1}$, where T_0 = epoch of periastron passage.

REFERENCES.—(1) Finger et al. 1996a; (2) Deeter et al. 1991; (3) Wilson et al. 1994a; (4) Levine et al. 1991; (5) Finger et al. 1993; (6) Rubin et al. 1997; (7) Levine et al. 1993; (8) Cook & Page 1987; (9) Finger et al. 1997; (10) Chakrabarty et al. 1993; (11) § 4, this work; (12) Koh et al. 1997; (13) Rappaport et al. 1978; (14) Cominsky et al. 1994; (15) Stella et al. 1985; (16) Finger et al. 1996b; (17) Stollberg et al. 1997; (18) Finger et al. 1994a; (19) Kelley et al. 1983; (20) Scott et al. 1997; (21) Wilson et al. 1997; (22) Nagase et al. 1992.

long episodes ($\gtrsim P_{\text{orb}}$) of relatively steady torques. On the other hand, the wind-fed supergiant binaries (*squares*) have longer orbital periods (as required to avoid Roche lobe overflow), longer spin periods, and are less luminous ($L_x \sim 10^{35}$ – 10^{37} ergs s⁻¹). In addition, the observed accretion torque on these wind-fed objects often fluctuates (even between spin-up and spin-down) on timescales much shorter than the orbital period. Finally, the Be transients (*circles*) populate a third region of the diagram, displaying a marked correlation between their spin and orbital periods. It has been suggested that this correlation arises from the fact that, given identical companion masses and mass-loss rates, neutron stars in systems with longer orbital periods are farther away from their companions, which thus leads to lower mass accretion rates and higher equilibrium periods. In addition, Waters & van Kerkwijk (1989) argue that selection effects favor the detection of Be systems that are in equilibrium with the slow equatorial wind of the companion. The observed anticorrelation of spin and orbital periods for the Roche lobe–filling supergiants is not understood. As Figure 5 shows, most of the high-mass systems are

found in the Galactic plane, consistent with the short lifetime of the massive companions.

The torque exerted on an accreting star depends on the nature of the angular momentum transfer during the accretion of matter. Accreting pulsars are the only objects in which such measurements have been made repeatedly. The much larger moment of inertia of an accreting magnetic white dwarf (in particular, the DQ Her systems; Patterson 1994) requires a decade-long baseline to measure the change in spin period, and so only one torque measurement has typically been made for each object. Patterson's (1994) Table 1 shows five that are spinning up and one (V1223 Sgr) that is spinning down. BATSE's ability to measure repeatedly the spin frequency of accreting pulsars has allowed us to *monitor* the torque exerted during accretion. We have found that spin-up and spin-down are nearly equally prevalent in these systems, contrary to the picture in the 1970s, when most accreting pulsars were then observed to be spinning up steadily (see Fig. 5 in Joss & Rappaport 1984).

Assuming the gas deposits its angular momentum at the magnetospheric boundary and that field lines transport all

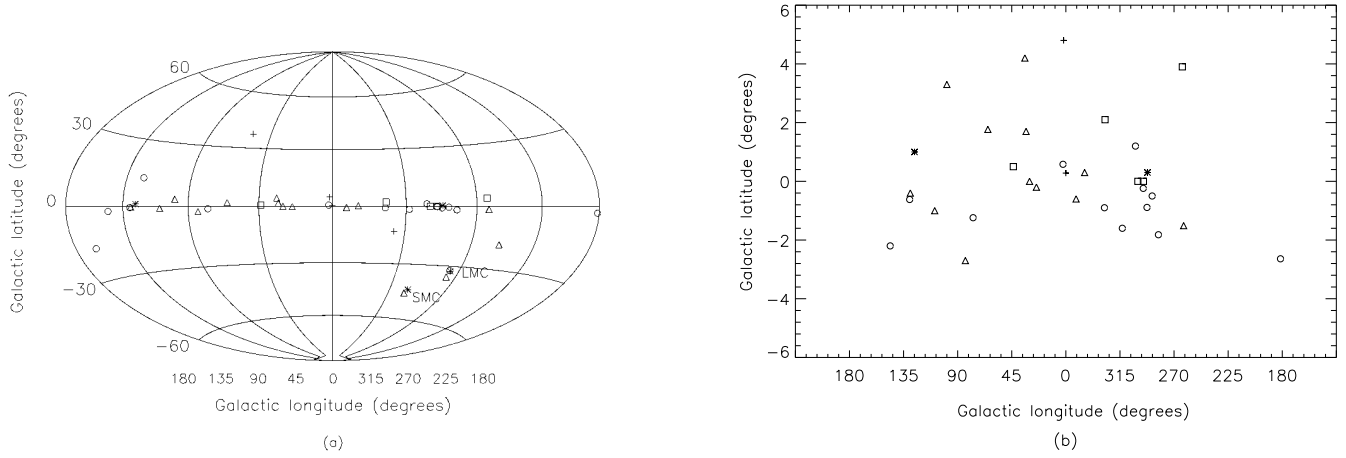


FIG. 5.—Galactic distribution of accreting pulsars. We plot the known Be transients as open circles, the low-mass objects as pluses, the disk-fed OB supergiants as asterisks, and the wind-fed OB supergiants as squares. This contains all pulsars listed in Table 1. Triangles denote sources with unknown companions and orbit. This symbol convention is the same as in Fig. 4, except here the symbols are not filled.

of this angular momentum to the star (Pringle & Rees 1972; Rappaport & Joss 1977b), a pulsar accreting from a disk will experience a spin-up torque

$$N \approx \dot{M} \sqrt{GM_X r_m}, \quad (3)$$

where $r_m = \xi r_A$ is the magnetospheric radius with the Alfvén radius

$$r_A = \left(\frac{\mu^4}{2GM_X \dot{M}^2} \right)^{1/7} \simeq 6.8 \times 10^8 \text{ cm} \left(\frac{\mu}{10^{30} \text{ G cm}^3} \right)^{4/7} \times \left(\frac{10^{-10} M_\odot \text{ yr}^{-1}}{\dot{M}} \right)^{2/7} \left(\frac{1.4 M_\odot}{M_X} \right)^{1/7} \quad (4)$$

being a characteristic length found by equating magnetic and fluid stresses for a neutron star with magnetic moment μ . Estimates for the model-dependent dimensionless number ξ range from 0.52 (Ghosh & Lamb 1979) to ≈ 1 (Arons 1993; Ostriker & Shu 1995; Wang 1996) for the case at hand, where $r_m \sim 10^8$ cm. The detailed physics by which material at this magnetospheric boundary loses its orbital angular momentum, becomes entrained on the magnetic field lines, and makes its way to the magnetic polar caps is thought to involve magnetohydrodynamical versions of Rayleigh-Taylor and Kelvin-Helmholtz instabilities (Lamb et al. 1973; Arons & Lea 1976, 1980; Elsner & Lamb 1977). For direct wind accretion, equation (3) gives an upper limit to the torque.

Accretion will be inhibited by a centrifugal barrier if the pulsar magnetosphere rotates faster than the Kepler frequency at the inner disk boundary. For accretion to occur, the magnetospheric radius should thus lie inside the corotation radius

$$r_{\text{co}} = \left(\frac{GM_X P_{\text{spin}}^2}{4\pi^2} \right)^{1/3} \simeq 1.7 \times 10^8 \text{ cm} \times \left(\frac{P_{\text{spin}}}{1 \text{ s}} \right)^{2/3} \left(\frac{M_X}{1.4 M_\odot} \right)^{1/3}. \quad (5)$$

For the case that $r_m < r_{\text{co}}$ while accreting, there is a characteristic torque,

$$N_0 \equiv \dot{M} \sqrt{GM_X r_{\text{co}}}, \quad (6)$$

which is a convenient fiducial as it depends only on the observable spin period of the pulsar and the inferred accre-

tion rate. The fiducial torque sets a scale, and the actual torque may be significantly smaller. A pulsar subject to the torque in equation (3) will spin up at a rate

$$\dot{\nu} = \frac{N}{2\pi I} \simeq 1.6 \times 10^{-13} \text{ s}^{-2} \left(\frac{\dot{M}}{10^{-10} M_\odot \text{ yr}^{-1}} \right) \times \left(\frac{P_{\text{spin}}}{\text{s}} \right)^{1/3} \left(\frac{r_m}{r_{\text{co}}} \right)^{1/2} \quad (7)$$

where $I \simeq 0.4 M_X R_X^2$ is the neutron star's moment of inertia (Ravenhall & Pethick 1994). The timescale for spinning up the neutron star is then

$$t_{\text{spin up}} \equiv \frac{\nu}{\dot{\nu}} \simeq 2 \times 10^5 \text{ yr} \left(\frac{10^{-10} M_\odot \text{ yr}^{-1}}{\dot{M}} \right) \times \left(\frac{1 \text{ s}}{P_{\text{spin}}} \right)^{4/3} \left(\frac{r_{\text{co}}}{r_m} \right)^{1/2}, \quad (8)$$

much shorter than the ages of most X-ray binaries (Elsner, Ghosh, & Lamb 1980). Hence, in this simple picture, the neutron star spins up until the spin frequency matches the Kepler frequency at the magnetosphere (or where $r_m \approx r_{\text{co}}$)

$$P_{\text{spin,eq}} \approx 8 \text{ s} \left(\frac{10^{-10} M_\odot \text{ yr}^{-1}}{\langle \dot{M} \rangle} \right)^{3/7} \left(\frac{\mu}{10^{30} \text{ G cm}^3} \right)^{6/7}. \quad (9)$$

Here $\langle \dot{M} \rangle$ is an appropriately averaged mass accretion rate. Presumably, neutron stars with periods shorter than $P_{\text{spin,eq}}$ cannot accrete easily and may experience a strong spin-down torque—the so-called propeller effect (Illarionov & Sunyaev 1975). If the observed accreting pulsars are near their equilibrium spin periods, then one infers magnetic field strengths from equation (9) in the range 10^{11} – 10^{14} G. The instantaneous accretion rates and observed torques can be much different than their long-term averages, however, so one obtains only a rough measure of the pulsar magnetic field in this way.

A more complex picture of accretion torques emerged as more systems were discovered and spin histories were extended. Her X-1 and LMC X-4 were found to be spinning up on a much longer timescale than predicted by equation (8). Some pulsars show secular spin-down behavior while

continuing to accrete (4U 1626–67, GX 1+4, 1E 1048.1–5937, 1E 2259+586, E1145.1–6141, and 4U 1538–52), while others show more erratic variations in spin period (Cen X-3, Vela X-1, and X Per). More sophisticated theories of accretion torque were developed to explain these observations, which take into account the magnetic interaction between the inner accretion disk and the neutron star magnetosphere (Ghosh & Lamb 1979; Anzer & Borner 1980; Arons et al. 1984). However, as we show in § 4, the continuous monitoring of accreting pulsars by the BATSE instrument has now substantially changed our view of many of these systems. We discuss these new observations and their implication for theories of accretion torque in § 5.

4. BATSE OBSERVATIONS OF INDIVIDUAL SOURCES

BATSE continuously monitors the spin frequency and pulsed flux of three low-mass systems (Her X-1, 4U 1626–67, and GX 1+4) and five high-mass systems (Cen X-3, OAO 1657–415, Vela X-1, 4U 1538–52, and GX 301–2). BATSE has also observed one or more outbursts from seven known transient systems (4U 0115+63, GS 0834–430, 2S 1417–624, EXO 2030+375, A0535+26, 4U 1145–619, and A1118–616). In addition, it has discovered five new transients (GRO J1744–28, GRO J1750–27, GRO J1948+32, GRO J1008–57, and GRO J2058+42). In Figure 6, we display long-term frequency histories of all sources seen with BATSE that were known prior to BATSE, including archival data.

In this section, intrinsic spin frequency and flux histories for the persistently accreting binaries are presented for the

first 4 years of BATSE monitoring, 1993 April 23–1995 February 11 (MJD 48,370–49,760). We also show frequency and flux histories of the outbursts for the transient sources. For those transients for which we have yet to measure the orbital parameters, we display the observed frequencies, whereas we display the intrinsic spin frequencies for neutron stars with measured orbital parameters. Up-to-date results on these sources are being made available through the public archive at the *Compton Observatory Science Support Center*.

In the following subsections, we categorize the accreting pulsars by the type of star from which they are accreting: low-mass stars ($M \lesssim 2 M_{\odot}$), OB supergiants, and main-sequence Be stars. We then briefly summarize the BATSE observations of each individual binary, focusing on those results obtained from continuous timing and pulsed flux monitoring.

Spectral fits to the pulsed flux are tabulated in Table 4 for most sources. These are typical spectra. Exposure varies from source to source. The interval used for spectral fitting is not always the brightest that the source displayed. For some sources, spectra could not be determined because the spin frequency was too high, the pulse profile varied with energy and/or luminosity, or the source was too weak.

Pulse profiles for all sources seen with BATSE are displayed in Figure 7. High-energy pulse profiles in accretion-powered pulsars are generally simpler and smoother than those $\lesssim 10$ keV, as they are less affected by circumstellar scattering and absorption. Thus, they may be more indicative of the intrinsic radiation pattern from the neutron star.

TABLE 4
SPECTRAL PARAMETERS MEASURED WITH BATSE

Source Name	Start (MJD)	End (MJD)	C_{30}^a (PL)	α^b (PL)	C_{30}^c (EXP)	kT^d (EXP)	Energy Range ^e	Pulsed Flux ^f
Low-Mass Systems								
Her X-1 ^g	48,376	50,114	62–199	3.5–5.8	61–201	7.7–19	25–165	7.4–25
4U 1626–67.....	48,450	48,715	17.6(6)	4.66(17)	17.7(6)	10.8(6)	26–76	2.2
GX 1+4.....	48,450	48,715	57.3(6)	2.95(2)	49.6(5)	28.4(3)	26–126	6.2
High-Mass Supergiant and Giant Systems								
OAO 1657–415.....	48,450	48,715	45.6(6)	3.12(3)	40.7(6)	24.7(4)	26–125	5.1
Vela X-1.....	48,450	48,715	249(1)	4.05(1)	254(1)	13.56(3)	24–97	30.8
GX 301–2.....	48,450	48,715	127(1)	4.26(2)	130(1)	12.1(1)	25–74	15.8
Transient Be-Binary Systems								
GRO J1750–27.....	49,960	49,967	22(4)	5(1)	23(4)	10(3)	26–72	2.9(7)
2S 1417–624.....	49,623	49,698	37.8(7)	2.92(3)	33.9(6)	28.1(6)	26–124	4.3
EXO 2030+375.....	49,170	49,360	54.8(17)	3.60(8)	46.6(15)	23.0(1)	23–71	12.1
GRO J1008–57.....	49,182	49,215	103(1)	3.11(2)	99(1)	22.1(3)	25–96	12.2
A0535+26.....	49,379	49,430	451(1)	2.99(1)	392(1)	26.3(1)	27–100	49.2
4U 1145–619.....	49,428	49,439	219(1)	3.48(1)	205(1)	19.3(2)	26–123	25.1
A1118–616.....	48,621	48,633	114(1)	3.66(4)	113(2)	16.2(3)	24–76	13.7
Transient Systems with an Undetermined Companion								
GRO J1948+32.....	49,448	49,482	25.8(10)	2.88(8)	25.5(8)	22.9(11)	24–76	3.2
GRO J2058+42.....	49,987	49,993	113(8)	4.35(16)	87(6)	15.3(9)	35–100	10.5

^a Normalization: 10^{-5} photons $\text{cm}^{-2} \text{s}^{-1} \text{keV}^{-1}$ at 30 keV, photon power-law (PL) model $C_{30}(E/30 \text{ keV})^{-\alpha}$.

^b Photon index, PL model.

^c Normalization: 10^{-5} photons $\text{cm}^{-2} \text{s}^{-1} \text{keV}^{-1}$ at 30 keV, exponential (EXP) model $C_{30}(30 \text{ keV}/E) \exp [(E - 30 \text{ keV})/kT]$.

^d Temperature (keV), EXP model.

^e Energy range used in fitting (keV).

^f 10^{-10} ergs $\text{cm}^{-2} \text{s}^{-1}$, 20–50 keV, from EXP model. Highly variable for most sources.

^g Fitted during Main Highs. Spectral shape varies. Table gives range of observed values.

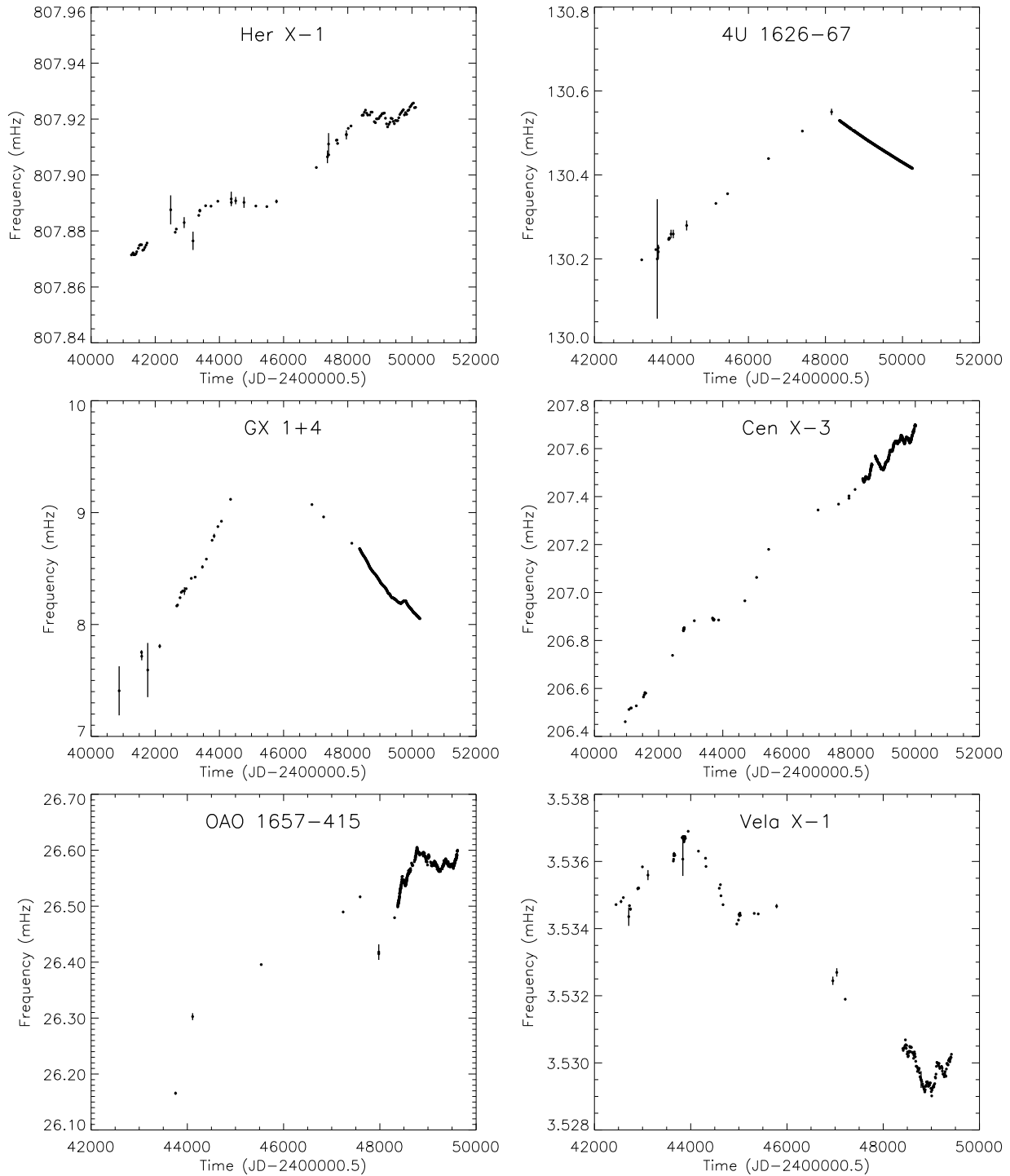


FIG. 6.—Long-term frequency history for all pulsars detected by BATSE that were previously known. The squares show the pre-BATSE data taken from Nagase (1989) and additional references. The line is the BATSE data, which we discuss later in great detail. The long-term frequency history for X-ray pulsars observed by BATSE that were known prior to the *Compton Observatory* launch commences 1991 April. For Her X-1, Cen X-3, Vela X-1, 4U 1538–52, GX 301–2, 4U 0115+634, and EXO 2030+375, all frequencies have been orbitally corrected. For OAO 1657–415, GS 0834–430, 2S 1417–62, and A0535+262, orbital corrections have been applied only to the BATSE observations. No orbital corrections have been applied for 4U 1626–67, GX 1+4, 4U 1145–619, or A1118–615, which have unknown, or incompletely known, orbital elements. The BATSE frequencies for OAO 1657–415, GS 0834–430, EXO 2030+375, 4U 1145–619, and A1118–615 are from the daily frequency history files we have deposited at the *Compton Observatory* archive. For the remainder of the objects, the frequencies are from source-specific studies: Her X-1 (Wilson et al. 1997), 4U 1626–67 (Chakrabarty et al. 1997a), GX 1+4 (Chakrabarty et al. 1997b), Cen X-3 (Finger et al. 1997), Vela X-1 (Finger et al. 1997), 4U 1538–52 (Rubin et al. 1997), GX 301–2 (Koh et al. 1997), 4U 0115+634 (Cominsky et al. 1997), 2S 1417–624 (Finger et al. 1996b), and A0535+262 (Finger et al. 1996c).

The profiles in Figure 7 can be classified broadly as single or double peaked. Aside from 4U 1145–619 and Her X-1, the profiles are essentially featureless, although they are visibly asymmetric, as can be seen clearly in OAO 1657–415 and

Vela X-1. Cases in which the pulse shape changes dramatically with energy or flux are discussed individually. Fluxes measured with BATSE have been found using both power-law and simple exponential models.

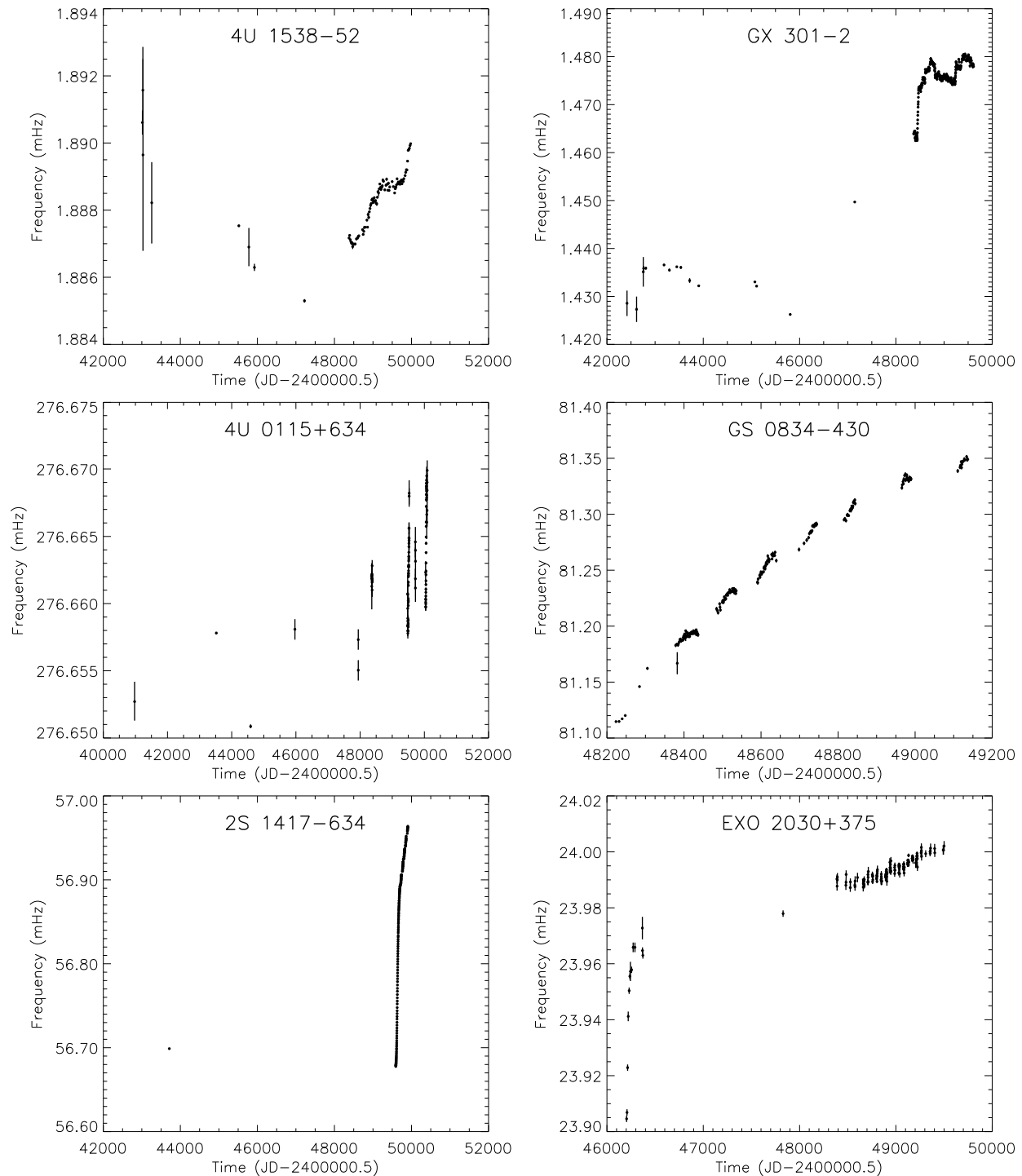


FIG. 6—Continued

4.1. Low-Mass Systems

Only four accreting pulsars are definitely known to be orbiting low-mass ($M \lesssim 2 M_{\odot}$) stars: Her X-1 and GRO J1744-28 on the basis of timing-based measurements of their companions' mass functions (Tananbaum et al. 1972; Finger et al. 1996a), 4U 1626-67 from optical photometry (Middleditch et al. 1981; Chakrabarty 1997), and GX 1+4 from spectroscopy (Davidsen, Malina, & Bowyer 1977; Chakrabarty & Roche 1997). This is a very heterogeneous class of objects: the mass donors are a main-sequence A star (Her X-1), a $<0.1 M_{\odot}$ helium or carbon-oxygen degenerate

dwarf (4U 1626-67), and two red giants (GX 1+4 and GRO J1744-28). The absence of an observable companion in very deep optical and IR searches and the lack of orbital detections also suggest low-mass companions for 4U 0142+61, 1E 1048.1-5937, RX J1838.4-0301, and 1E 2259+589 (see Mereghetti & Stella 1995 and references therein). We now discuss the BATSE observations of Her X-1, 4U 1626-67, GX 1+4, and GRO J1744-28.

Hercules X-1.—*Uhuru* discovered 1.2 s pulsations from Her X-1 (4U 1656+354) in 1971 (Tananbaum et al. 1972), and the pulsar was subsequently found to be in an eclipsing,

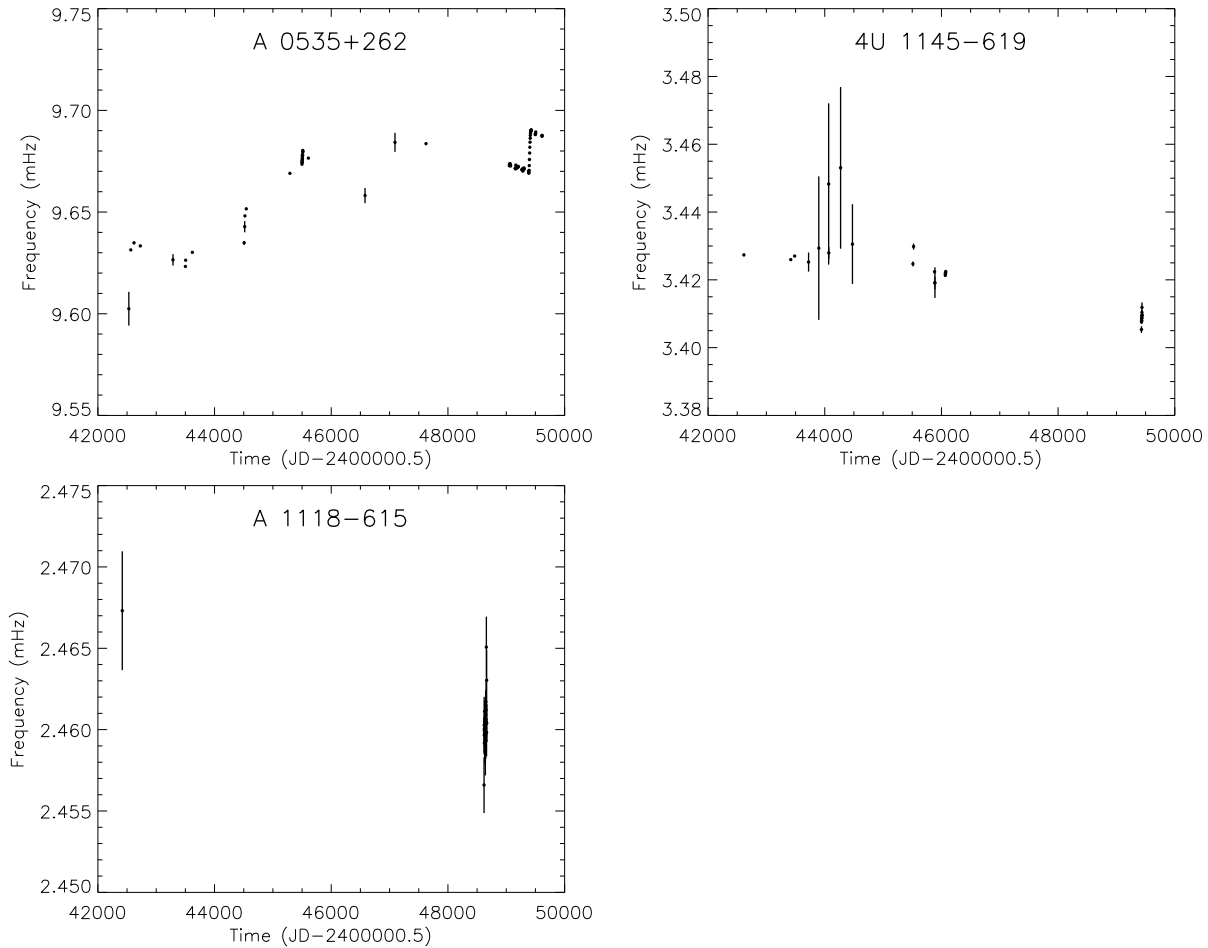


FIG. 6—Continued

circular, 1.7 day orbit (Deeter, Boynton, & Pravdo 1981) around the low-mass companion HZ Her (Doxsey et al. 1973; Gottwald et al. 1991). This disk-fed system exhibits “supercycles” of intensity modulated with a period of ≈ 35 days (Giacconi et al. 1973; Soong et al. 1990). At energies of 1–10 keV, the source is observed during both a “Main High” and “Short High” interval of the 35 day cycle. Detailed discussion of BATSE observations have appeared elsewhere (Wilson et al. 1994d, 1994c).

BATSE detects pulsations for 5–10 days during each Main High interval. We report an average frequency for each Main High interval since reliable measurements of $\dot{\nu}$ within a Main High are hampered by the low signal-to-noise ratio of the BATSE data as well as pulse shape variations. Analyses of 20 Her X-1 Main High observations through 1993 July found that the pulsed 20–70 keV luminosity varied by a factor of ~ 4 and that the pulsar was spinning down during 35 day cycles when the immediately preceding Main High interval luminosity (averaged over the peak days of the interval), and presumably the mass accretion rate, was low (Wilson et al. 1994d). Subsequent observations do not universally show a significant correlation of luminosity and $\dot{\nu}$, with some episodes of spin-down following intervals with high flux levels. The neutron star is usually spinning up with $\dot{\nu}$ between zero and a maximum of $5 \times 10^{-13} \text{ Hz s}^{-1}$ between 32 of the 48 observed intervals. As is evident in Figure 8, the maximum spin-down rates are larger in magnitude, reaching $7 \times 10^{-13} \text{ Hz s}^{-1}$.

4U 1626–67.—SAS-3 discovered 7.68 s pulsations from 4U 1626–67 in 1977 (Rappaport et al. 1977), and the optical counterpart was later identified to be KZ TrA (McClintock et al. 1977). See Figure 9. X-ray timing limits imply an ultracompact binary with an extremely low-mass companion (Levine et al. 1988; Chakrabarty et al. 1997a). There is optical photometric evidence for a 42 minute orbital period (Middleditch et al. 1981; Chakrabarty 1998), which suggests a mass of $< 0.1 M_{\odot}$ for the mass donor.

Detailed discussions of BATSE observations have appeared elsewhere (Bildsten et al. 1994; Chakrabarty et al. 1997a). The neutron star was observed to spin up steadily during 1977–1991 and made a transition to steady spin-down at nearly the same rate of $|\nu/\dot{\nu}| \approx 5000 \text{ yr}$ by the start of BATSE observations in 1991. Despite this torque reversal, there is no evidence for a large change in the bolometric flux from the source. The torque exerted on the neutron star is quiet, in the sense that the torque-fluctuation power measured by BATSE is the lowest measured for any X-ray pulsar and is comparable to the timing noise observed in young rotation-powered radio pulsars.

GX 1+4.—An 18–50 keV X-ray balloon experiment discovered ≈ 2 minute pulsations from GX 1+4 in 1970 (Lewin, Ricker, & McClintock 1971). See Figure 10. It is now known to be orbiting an M5 III giant (Davidsen et al. 1977; Chakrabarty & Roche 1997), which makes it the only verified accreting pulsar with a red giant donor. The binary period is unknown but is believed to be of order years

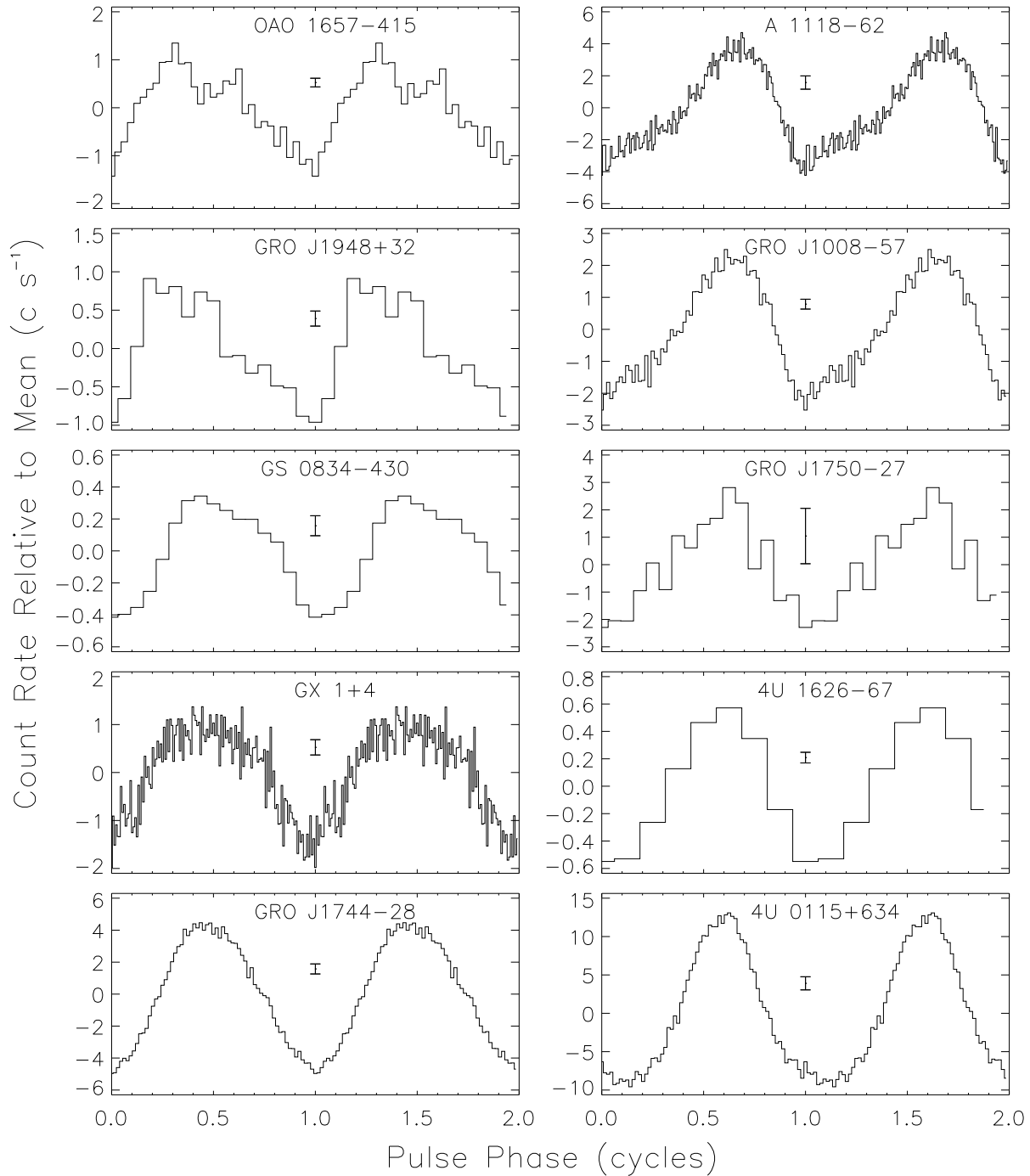


FIG. 7.—Pulse profiles of accreting pulsars from BATSE, in 20–35 keV except as noted. The 1σ error bar in each phase bin is also shown. The range of days (in MJD) summed to construct the profiles for each of the sources (and energy range if different from above) are (a) OAO 1657–415 (48,450–48,715), A1118–62 (48,621–48,633), GRO J1948+32 (49,448–49,482), GRO J1008–57 (49,182–49,215), GS 0834–430 (48,518–48,522), GRO J1750–27 (49,960–49,967; 20–70 keV), GX 1+4 (48,450–48,715), 4U 1626–67 (48,450–48,715), GRO J1744–28 (50,092–50,098), 4U 0115+634 (50049–50057; 20–40 keV) and (b) 4U 1145–619 (49,428–49,439), EXO 2030+375 (48,450–48,715), 4U 1538–52 (49,350–49,421; 20–50 keV), A0535+262 (49,379–49,430), GRO J2058+42 (49,987–49,993; 20–40 keV), GX 301–2 (48,450–48,715), Cen X-3 (48,985–48,992), Vela X-1 (48,450–48,715), Her X-1 (49,586–49,593; 20–40 keV), 2S 1417–62 (49,623–49,698).

(Chakrabarty & Roche 1997). Throughout the 1970s, GX 1+4 was persistently bright and was spinning up on a timescale $|\dot{\nu}/\nu| \sim 40$ yr, increasing in frequency from ~ 7.5 mHz to ~ 9 mHz between 1970 and 1980 (Nagase 1989). After decreasing in flux by at least 2 orders of magnitude in the early 1980s, GX 1+4 was found by *Ginga* to be rapidly spinning down (Makishima et al. 1988).

Detailed discussions of the BATSE observations of GX 1+4 have appeared elsewhere (Chakrabarty et al. 1994a, 1997b). These observations found GX 1+4 to have the hardest spectrum of any accretion-powered pulsar, with pulsations clearly detected up to energies of 160 keV (Chakrabarty et al. 1997b). GX 1+4 is spinning down, on average, on a timescale $|\dot{\nu}/\nu| \approx 40$ yr. During 1991–1994,

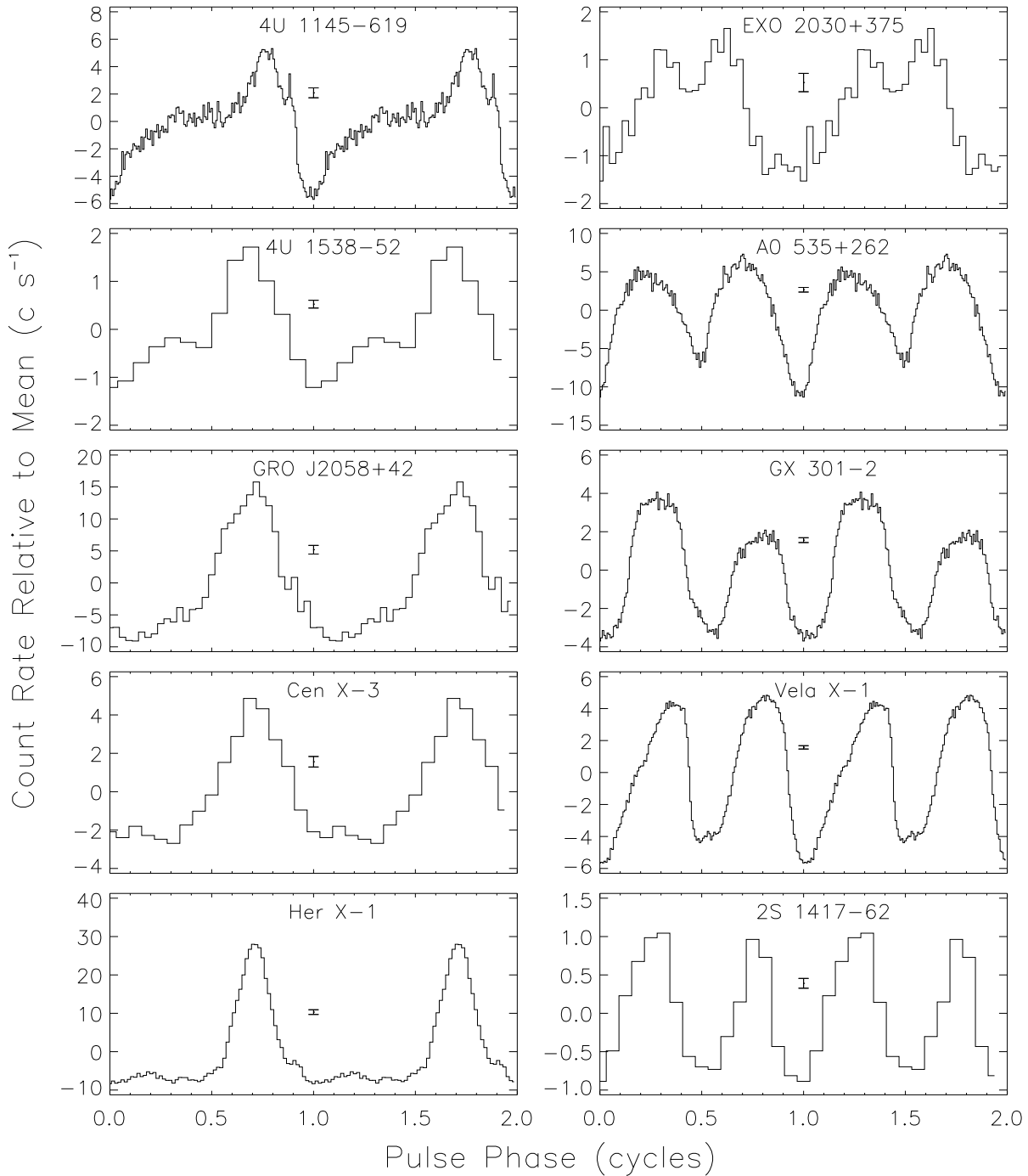


FIG. 7—Continued

BATSE observed a number of bright flares in the hard X-ray (20–100 keV) band that were accompanied by episodes of enhanced spin-down. A smooth torque reversal to spin-up accompanied an extended bright state during late 1994 and early 1995 (Chakrabarty et al. 1994b), followed by a return to spin-down and a lower average hard X-ray flux (Chakrabarty et al. 1995b). During spin-down, the torque fluctuations exhibit a $1/f$ power density spectrum, similar to that seen in Cen X-3.

GRO J1744–28.—GRO J1744–28 was initially discovered by BATSE as an unusual bursting source in the direction of the Galactic center (Kouveliotou et al. 1996). See Figure 11. The discovery of coherent 467 ms pulsations

by BATSE and subsequent pulse timing unambiguously established GRO J1744–28 to be a neutron star in a circular 11.8 day orbit around a low-mass companion and indicated that the neutron star was spun up by an accretion disk during the outburst (Finger et al. 1996a). These are the first persistent pulsations seen in a bursting X-ray source.

Detailed discussions of the BATSE observations of GRO J1744–28 have appeared elsewhere (Finger et al. 1996a). One major outburst has been observed to date, spanning \approx MJD 50,053–50,223. Another outburst which began on \approx MJD 50,253 lasted for only \approx 1 week. The initial outburst showed enough dynamic range that the relation between accretion torque and pulsed flux could be tested directly

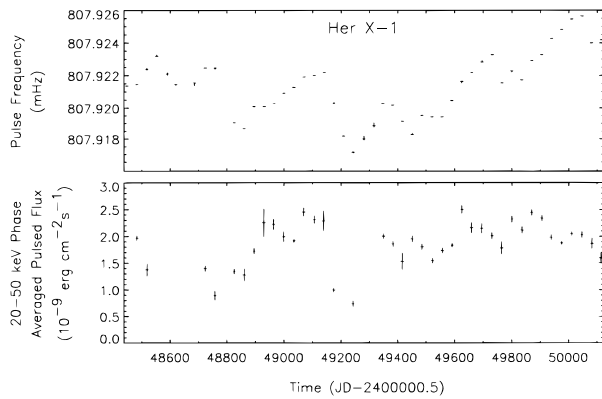


FIG. 8.—Her X-1 frequency and pulsed flux measurements from BATSE. A mean frequency has been determined for each Main High state for which adequate scheduled folded-on-board data were available. The frequencies, which have been orbitally corrected using parameters from Wilson et al. (1994a), were obtained using linear fits to pulse phases of 20–70 keV data (see Appendix B, § 1.3). Pulsed fluxes are the pulse phase-averaged flux obtained during one orbital period (averaged from eclipse egress to eclipse ingress) during the brightest portion of each available Main High state. An exponential model, with the e -folding energy allowed to vary, was used to obtain the fluxes (see Appendix B, § 2.3).

(see § 5.2). The 20–40 keV pulse profile is nearly sinusoidal, in stark contrast to the more complicated pulse shapes seen in other accretion powered pulsars (see Fig. 7). Simultaneous 20–40 keV pulsed and Earth occultation DC flux measurements on 10–16 January 1996 (MJD 50,092–50,098) yielded a peak-to-peak pulsed fraction of $\approx 25\%$ (Finger et al. 1996a).

4.2. High-Mass Supergiant Systems

BATSE continuously monitors five pulsars that accrete from high-mass evolved supergiants: Cen X-3, OAO 1657–415, Vela X-1, 4U 1538–52, and GX 301–2. The long-term spin frequency evolution of these pulsars has revealed several surprises that challenge the standard model of such systems, as we discuss in § 5. For example, Cen X-3 (the only Roche lobe-filling, high-mass supergiant system

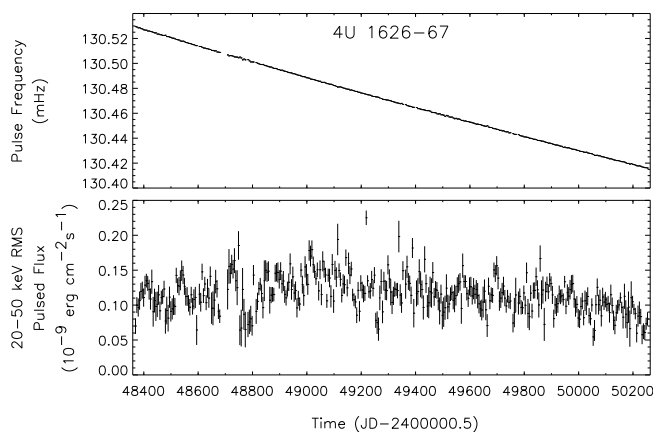


FIG. 9.—4U 1626–67 frequency and pulsed flux measurements from BATSE. The spin frequencies, which have not been orbitally corrected since the orbit is unknown, were determined at 5 day intervals by searching the Fourier power spectrum of the 20–50 keV DISCLA data for the strongest signal in a small range around 7.7 s (see Appendix B, § 1.1). The pulsed fluxes were obtained by assuming a power-law spectral model with a photon number index of 4.9 (see Appendix B, § 2.3).

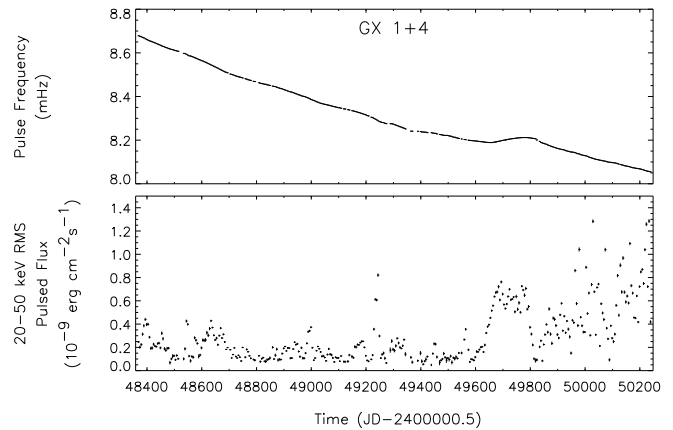


FIG. 10.—GX 1+4 frequency and pulsed flux measurements from BATSE. The spin frequencies, which have not been orbitally corrected since the orbit is unknown, were determined at 5 day intervals by searching the Fourier power spectrum of the 20–50 keV DISCLA data for the strongest signal in the pulse period range $110 \text{ s} \lesssim P_{\text{spin}} \lesssim 130 \text{ s}$ (see Appendix B, § 1.1). The pulsed fluxes were determined at 5 day intervals by assuming a power-law spectral model with a photon number index of 2.5 (see Appendix B, § 2.3).

observed by BATSE) exhibits short-term (~ 50 day) spin-up and spin-down episodes. Moreover, the underfilled Roche lobe system GX 301–2 exhibits transient spin-up episodes, also of ~ 50 day durations.

Centaurus X-3.—*Uhuru* discovered 4.8 s pulsations from Cen X-3 in 1971, the first observation of an accreting pulsar (Giacconi et al. 1971). See Figure 12. This bright, persistent, eclipsing pulsar is in a 2.1 day orbit (Kelley et al. 1983) around the O6–8 supergiant V779 Cen (Krzeminski 1974; Rickard 1974; Hutchings et al. 1979). An accretion disk is apparent from the optical light curve (Tjemkes, Zuiderwijk, & van Paradijs 1986). Pre-BATSE observations by numerous pointed instruments found the neutron star to be gradually spinning up, although episodes of spin-down have been observed (Nagase 1989).

Detailed discussions of the BATSE observations of Cen X-3 have appeared elsewhere (Finger et al. 1992; Finger,

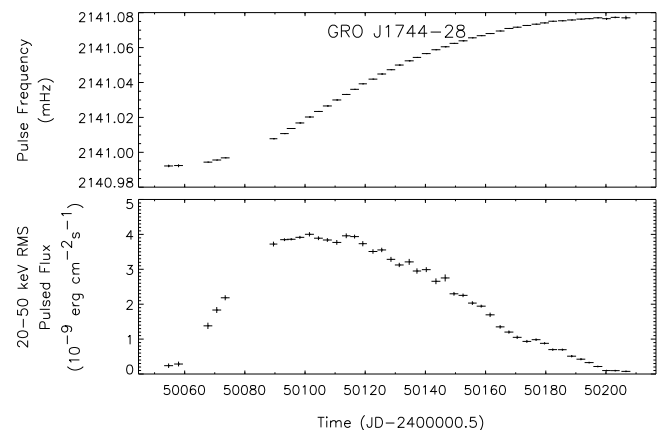


FIG. 11.—GRO J1744–28 frequency and pulsed flux measurements from BATSE. The spin frequencies, which have been orbitally corrected using parameters from Finger et al. (1996a), were determined at 2 day intervals by fitting pulse phases derived from pulsar folded-on-board data in the 20–40 keV band (see Appendix B, § 1.3). The pulsed fluxes were obtained by assuming a spectra of the form $F(E) = AE^{-\lambda} \exp(-E/kT)$ with $\lambda = 2.0$ and $kT = 15 \text{ keV}$, as determined by OSSE measurements (Strickman et al. 1996) (see Appendix B, § 2.3).

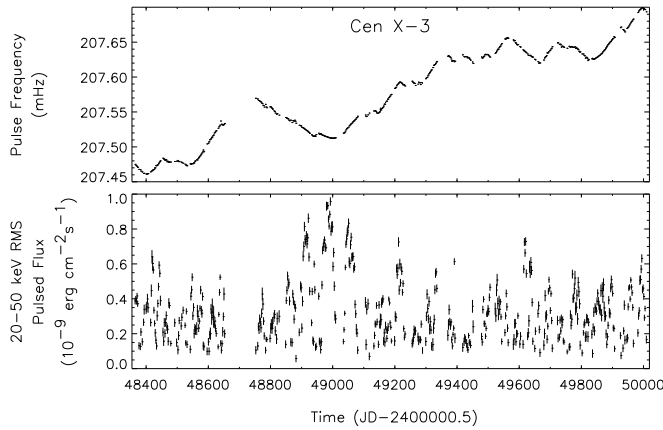


FIG. 12.—Cen X-3 frequency and pulsed flux measurements from BATSE. The intrinsic spin frequencies, which have been orbitally corrected using parameters from Finger et al. (1993), were determined at 2.1 day intervals by epoch-folding the 20–50 keV DISCLA data (see Appendix B, § 1.2). The pulsed fluxes were determined at 2.1 day intervals by assuming an exponential spectrum with an e -folding energy of 12 keV (see Appendix B, § 2.3).

Wilson, & Fishman 1994b). These continuous observations found that the long-term (\sim years) spin-up trend is actually the average effect of alternating about 10 to about 100 day intervals of spin-up and spin-down at a constant rate (Finger et al. 1994b). Large excursions in the X-ray intensity occur on timescales of days to weeks, including bright flares lasting 10–40 days. A comparison of the orbital measurements made over the last 20 years reveals that the orbital period is decreasing (Kelley et al. 1983; Nagase et al. 1992). BATSE confirms this orbital decay (Finger et al. 1993), which is thought to be due to the tidal interaction of the neutron star with its companion.

OAo 1657–415.—*HEAO 1* discovered 38.22 s pulsations from OAO 1657–415 in 1978 (White & Pravdo 1979). See Figure 13. BATSE observations revealed a 10.4 day binary orbit with a 1.7 day eclipse by the stellar companion (Chakrabarty et al. 1993), making it the seventh eclipsing

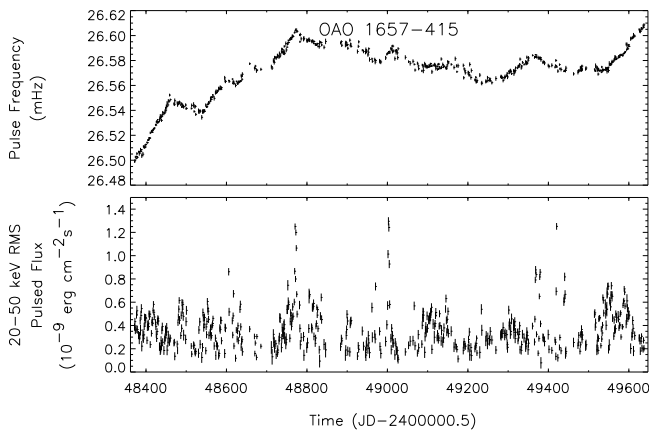


FIG. 13.—OAo 1657–415 frequency and pulsed-flux measurements from BATSE. The intrinsic spin frequencies, which have been orbitally corrected using parameters from Chakrabarty et al. (1993) and a refined orbital period of $P_{\text{orb}} = 10.44809(30)$ days (see text below for details), were measured at 1 day intervals from the power spectra of the 15–55 keV CONT data (see Appendix B, § 1.1). The pulsed fluxes were measured at 1 day intervals by assuming an exponential spectrum with a e -folding energy of 20 keV (see Appendix B, § 2.3).

X-ray pulsar discovered. The intrinsic spin frequency history reveals strong, stochastic variability and alternating episodes of steady spin-up and spin-down lasting 10–200 days, similar to what is seen in Cen X-3. Although the companion remains unidentified, it is inferred to be an OB supergiant from the neutron star orbit (Table 3) and eclipse duration (Chakrabarty et al. 1993).

Chakrabarty et al. (1993) measured the binary orbital parameters using BATSE data spanning 1991 April 24 to 1992 July 23 (MJD 48,370–48,460). For the spin frequency history presented here, which extends far beyond the data used in the original orbital analysis, it was necessary to refine the orbital period. For this purpose, the pulse frequencies obtained between 1991 April 24 and 1994 September 20 (MJD 48,370–49,615) were fitted using the Chakrabarty et al. (1993) orbital elements, with P_{orb} as a free parameter. The contribution to the uncertainty in P_{orb} from stochastic variations in accretion torque was estimated by assuming that ν performed a random walk with a strength of $2.5 \times 10^{-17} \text{ Hz}^2 \text{ s}^{-1}$, as estimated from the power spectrum of the frequency derivative measured at P_{orb} (see Fig. 34). The revised orbital period is $P_{\text{orb}} = 10.44809(30)$ days, consistent with the value measured by Chakrabarty et al. (1993) but of improved accuracy.

Vela X-1.—*SAS-3* discovered 283 s pulsations from the eclipsing binary Vela X-1 in 1975 (McClintock et al. 1976), and pulse timing revealed this pulsar to be in an 8.96 day eccentric orbit (Rappaport, Joss, & McClintock 1976; Finger et al. 1997) around the B0.5 Ib supergiant HD 77581 (Hiltner, Werner, & Osmer 1972; van Kerkwijk et al. 1995). See Figure 14. The optical light curve of the companion shows ellipsoidal variations, which indicates that the star is substantially distorted by the tidal field from the neutron star (Tjemkes et al. 1986).

Vela X-1 is the brightest persistent accretion-powered pulsar in the 20–50 keV energy band. Individual pulses are often visible in the raw data (Fig. 1). BATSE observations showed Vela X-1 alternating between spin-up and spin-down, with no long-term trend in spin frequency, consistent with pre-BATSE observations of a random walk in spin

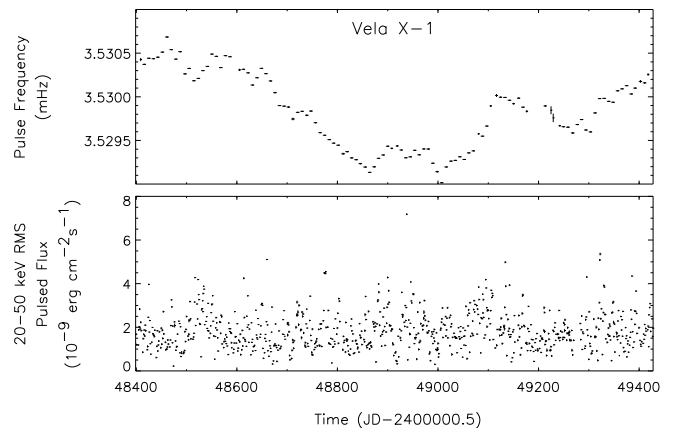


FIG. 14.—Vela X-1 spin frequency and pulsed flux measurements from BATSE. The intrinsic spin frequencies, which have been orbitally corrected using parameters from Finger et al. (1997), were determined by fitting pulse phase measurements (see Appendix B, § 1.3). Each point uses the uneclipsed data of the 8.96 day binary orbit. The pulsed fluxes were determined at 1 day intervals by assuming an exponential spectrum with an e -folding energy of 20 keV (see Appendix B, § 2.3).

frequency (Deeter et al. 1989). Pulse profiles in the BATSE energy range are double peaked and vary slightly with both energy and time, with some evidence for a correlation between luminosity and pulse shape. At lower energies, the pulse profiles are more complex, showing dramatic changes with energy (Raubenheimer 1990).

4U 1538–52.—*Ariel 5* discovered 530 s pulsations from 4U 1538–52 in 1976 (Davison, Watson, & Pye 1977), and pulse timing revealed this pulsar to be in a 3.7 day circular orbit (Davison et al. 1977; Corbet, Woo, & Nagase 1993) around the B0 supergiant companion, QV Nor (Parkes, Murdin, & Mason 1978), which most likely underfills its Roche lobe (Crampton, Hutchings, & Cowley 1978). See Figure 15. Pre-BATSE data show a long-term spin-down trend with random pulse period variations on shorter timescales (Makashima et al. 1987; Nagase 1989).

Detailed BATSE observations of 4U 1538–52 have appeared in Rubin et al. (1994). These observations revealed a reversal of the secular torque to long-term spin-up at an average rate of $\dot{\nu} = 1.8 \times 10^{-14} \text{ Hz s}^{-1}$. However, the change in ν is comparable in magnitude to what one would predict from the observed torque noise strength of $\sim 10^{-20} \text{ Hz}^2 \text{ s}^{-2} \text{ Hz}^{-1}$ (Fig. 34) and is thus consistent with being the result of a random walk in frequency. Combining orbital epochs measured with BATSE with those determined from previous experiments has led to an improved value for the orbital period (see footnote f to Table 3) and a 95% confidence limit on the rate of change of \dot{P}_{orb} of $-3.9 \times 10^{-6} < \dot{P}_{\text{orb}}/P_{\text{orb}} < 2.1 \times 10^{-6} \text{ yr}^{-1}$ (Rubin et al. 1997).

GX 301–2.—*Ariel 5* discovered 700 s pulsations from GX 301–2 (4U 1223–62) (White et al. 1976), and subsequent observations revealed the neutron star to be in a 41.5 day eccentric ($e = 0.47$) orbit (Sato et al. 1986) around the supergiant Wray 977 (Parkes et al. 1980; Kaper et al. 1995). See Figure 16. Between 1975 and 1985, the neutron star was, on average, neither spinning up nor spinning down, which is indicative of wind accretion. However, a prolonged period of spin-up at $\dot{\nu} \approx 2 \times 10^{-13}$ began in 1985 (Nagase 1989).

Detailed discussion of BATSE observations have appeared elsewhere (Koh et al. 1997). BATSE observed two

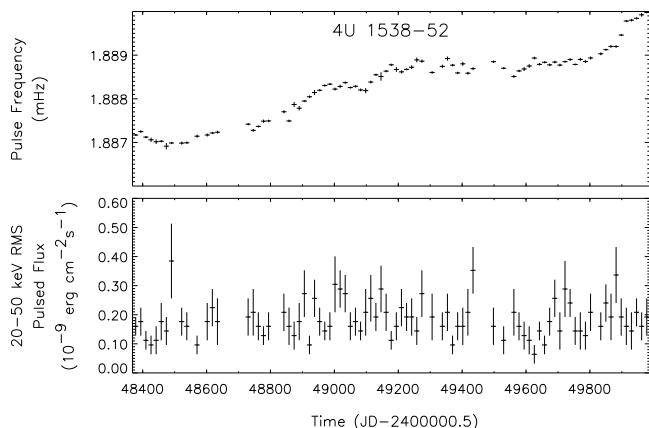


FIG. 15.—4U 1538–52 spin frequency and pulsed flux measurements from BATSE. The intrinsic spin frequencies, orbitally corrected using parameters from Rubin et al. (1997), were determined at 16 day intervals by epoch-folding the 20–50 keV DISCLA data at a range of trial frequencies after subtracting the background model of Rubin et al. (1996) (see Appendix B, § 1.2). Measurements are obtained only once every 16 days owing to the low flux from the object and BATSE’s poor sensitivity at long periods.

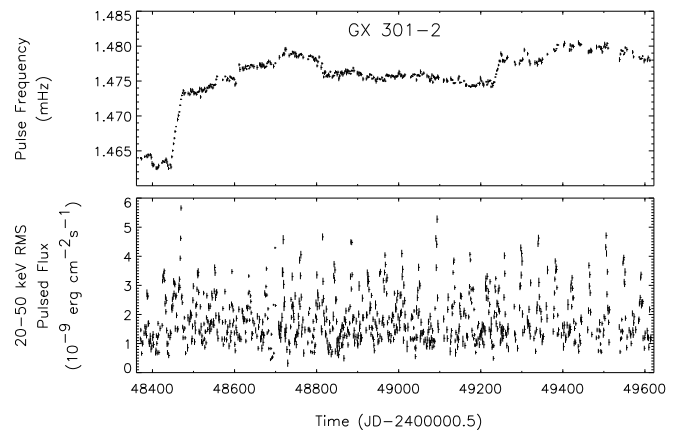


FIG. 16.—GX 301–2 frequency and pulsed flux measurements from BATSE. The intrinsic spin frequencies, which have been orbitally corrected using parameters from Koh et al. (1997), were measured at 2 day intervals by searching the Fourier power spectrum of the 15–55 keV CONT data for the strongest signal in a range around the previously observed pulse frequency (see Appendix B, § 1.1). The pulsed fluxes were measured at 2 day intervals by assuming an exponential spectrum with an e -folding energy of 10 keV (see Appendix B, § 2.3).

rapid spin-up episodes with $\dot{\nu} \approx (3–5) \times 10^{-12} \text{ Hz s}^{-1}$, each lasting ~ 30 days, probably indicating the formation of a transient accretion disk. Except for these spin-up episodes, there are virtually no net changes in ν on long timescales, which suggests that the long-term spin-up trend observed since 1985 may be due entirely to brief (≈ 30 day) spin-up episodes similar to those we have discovered. In addition to confirming the previously known flare that occurs ≈ 1.4 days before periastron, BATSE occultation and pulsed-flux measurements folded at the orbital period reveal a smaller flare near apastron (Pravdo et al. 1995; Koh et al. 1997). Orbital parameters measured with BATSE are consistent with previous measurements, with improved accuracy in the orbital epoch (Koh et al. 1997, Table 3). Simultaneous pulsed and occultation fluxes measured near periastron yield a 20–55 keV peak-to-peak pulsed fraction of ≈ 0.5 (Koh et al. 1997).

4.3. High-Mass Transient Systems

BATSE has discovered four new high-mass, transient accreting pulsars (GRO J1008–57, GRO J1948+32, GRO J2058+42, and GRO J1750–27), two of which (GRO J2058+42 and GRO J1008–57) have repeated. In addition, BATSE has observed multiple outbursts of the previously known transient accreting pulsars 4U 0115+63, GS 0834–43, 2S 1417–62, A0535+26, 4U 1145–619, and EXO 2030+375, and a single outburst from A1118–615. Outburst times and durations are shown in Figure 17.

BATSE has observed a series of regularly spaced outbursts from several transient pulsars. This was the case for GRO J1008–57 (five outbursts), GRO J2058+42 (five outbursts), A0535+26 (six outbursts), 4U 0115–634 (eight outbursts), 2S 1417–62 (eight outbursts), EXO 2030+375 (17 outbursts), 4U 1145–619 (seven outbursts), and GS 0834–430 (seven outbursts). In some cases, one or more outbursts were missing from the sequence. In the case of GS 0834–43, the spacing of the final two outbursts was irregular.

4U 0115+634.—*SAS-3* discovered 3.6 s pulsations from 4U 0115+634 in 1978 (Cominsky et al. 1978), and sub-

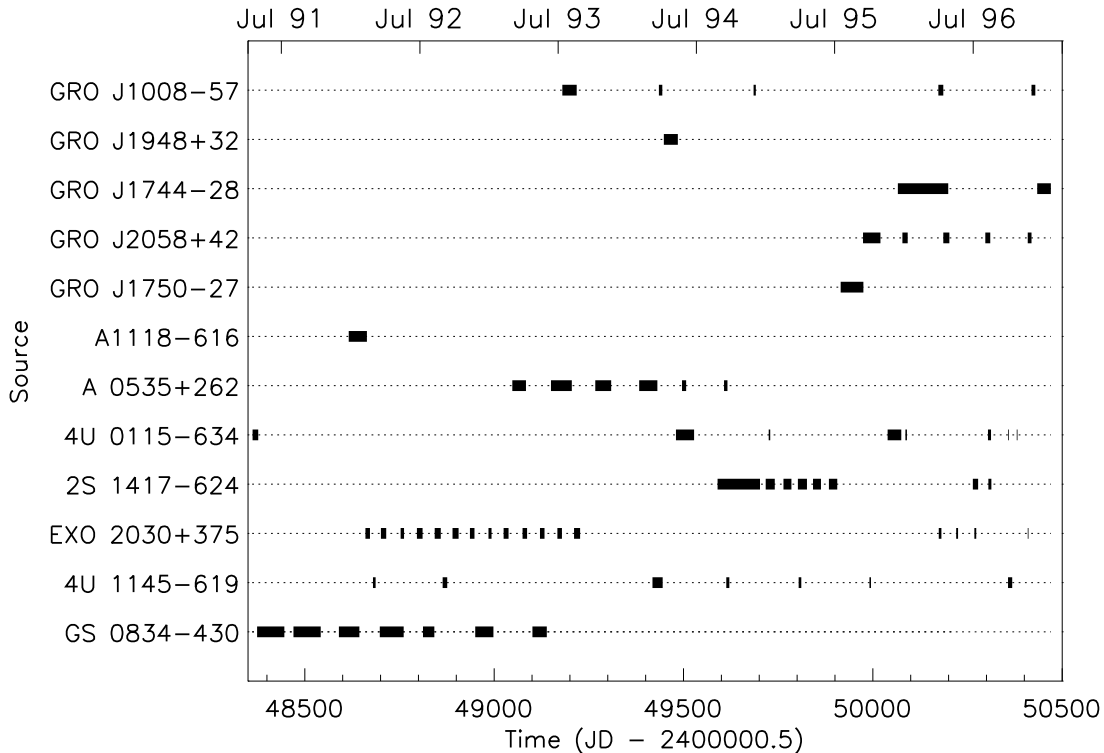


FIG. 17.—Outburst times for all transient accreting pulsars observed by BATSE

sequent pulse timing revealed the pulsar to be in a 24 day eccentric orbit (Rappaport et al. 1978) around the heavily reddened Be star, V635 Cas (Johns et al. 1978). See Figure 18. To date, BATSE has observed five outbursts from 4U 0115+634. A 48 day outburst from 1994 May 7 to June 24 (MJD 49,480–49,528) (Scott et al. 1994; Wilson, Finger, & Scott 1994) showed a sudden rise in pulsed flux at the middle of the outburst, shortly following periastron passage (MJD 49,498.1). A 36 day outburst from 1995 November 17 to December 27 (MJD 50,039–50,075) (Finger et al. 1995) was also seen by *Granat*/WATCH (Sazonov & Sunyaev

1995). This was immediately followed in 1996 January by a short weak outburst. Not shown in Figure 18 is a 10 day outburst in 1996 August (Scott et al. 1996).

We estimated the epoch of periastron for the outbursts in 1991 April, 1994 May–June, and 1995 November–December by fitting the phase measurements for each data set with a polynomial in pulse emission time using the orbital elements from Rappaport et al. (1978) but allowing the epoch of periastron to vary. This resulted in periastron epochs of MJD 48,355.44(7), 49,498.1232(15), and 50,057.4015(32), which are plotted in Figure 19 along with previous determinations. The *Ginga* result (Tamura et al. 1992) deviates from the trend of the other points. This may be due to an incorrect phase connection in that poorly sampled data set. Discarding this point, we find a best-fit linear ephemeris of the periastron epoch $T_p = \text{MJD } 49,279.2677(34) + n \times 24.317037(62)$. The frequencies in Figure 18 are orbitally corrected using this ephemeris in combination with the remaining Rappaport et al. (1978) elements.

GRO J1750–27.—BATSE discovered and observed a single 60 day outburst from the 4.4 s accreting pulsar GRO J1750–27 from 1995 July 7 to September 18 (MJD 49,915–49,978) (Wilson et al. 1995b; Scott et al. 1997). See Figure 20. Pulse timing revealed an eccentric 29.82 day orbit. A 0°5 localization with BATSE (Koh et al. 1995) motivated an *ASCA* target of opportunity that successfully localized the object to $\approx 2'$ (Dotani et al. 1995). Although no optical counterpart has been reported, the orbital period and pulse period of GRO J1750–27 place it squarely in the Be-transient region of the Corbet diagram (Fig. 4). Steady spin-up with a peak value of $3.8 \times 10^{-11} \text{ Hz s}^{-1}$ coupled with a correlation between the spin-up rate and the pulsed flux strongly suggests accretion from a disk (Scott et al. 1997).

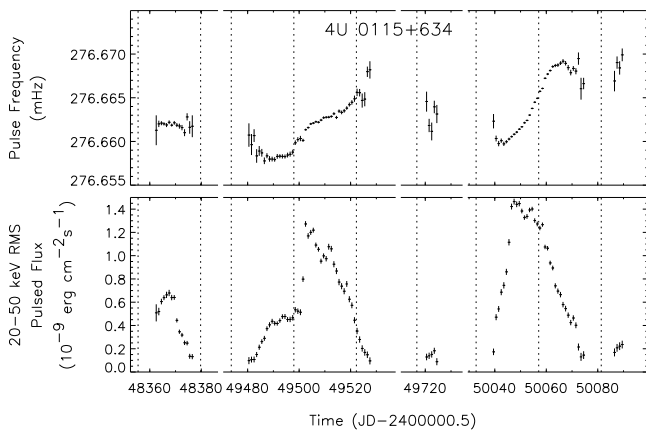


FIG. 18.—4U 0115+634 frequency and flux measurements from BATSE. The intrinsic spin frequencies, which have been orbitally corrected using the orbital parameters discussed in the text, were determined at 1 day intervals by epoch-folding the 20–50 keV DISCLA data at a range of trial frequencies (see Appendix B, § 1.2). The pulsed fluxes were determined at 1 day intervals by assuming an exponential spectrum with an e -folding energy of 15 keV (see Appendix B, § 2.3). The gaps in Fig. 18 are extended intervals when the source was undetectable with BATSE.

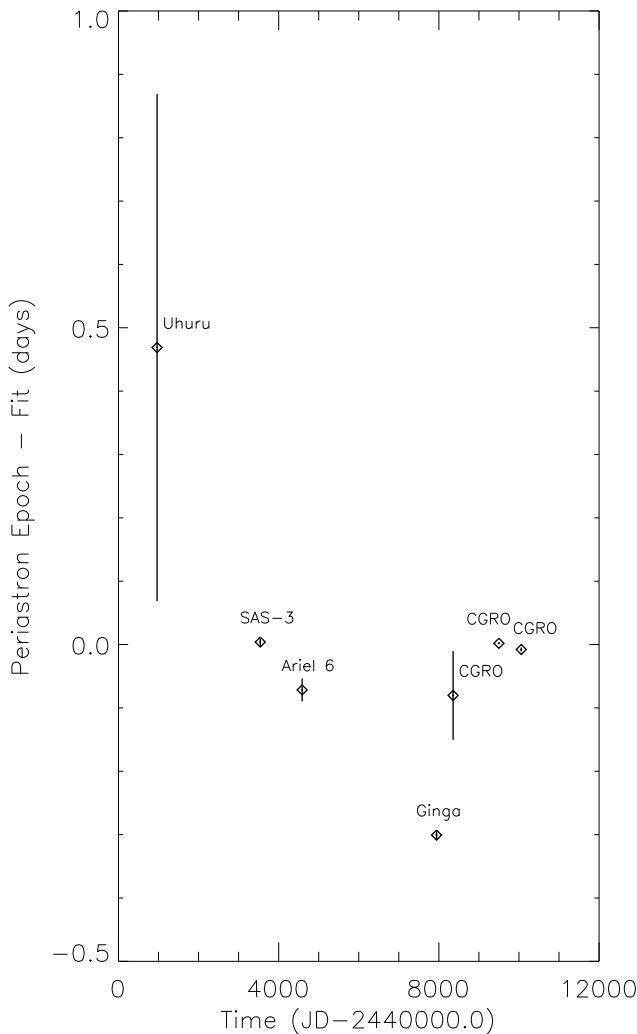


FIG. 19.—Measurements of the 4U 0115+63 periastron epoch. The plot shows the periastron epochs minus the linear ephemeris $\text{MJD } 49,279.2677 + 24.317037 \times n$, where n is an integral number of orbits. This ephemeris is discussed in the text. The epoch measurements have been determined from *Uhuru* (Kelley et al. 1981b), *SAS-3* (Rappaport et al. 1978), *Ariel 6* (Ricketts et al. 1981), *Ginga* (Tamura et al. 1992), and this work. Excluding the *Ginga* measurement, the observations are consistent with a constant orbital period.

GS 0834–430.—GS 0834–430 was first detected in 1990 February by *Granat*/WATCH, but confusion with the X-ray burster MX 0836–42 made unambiguous identification difficult (Lapshov et al. 1992). See Figure 21. Subsequent observations with *Ginga* revealed 12.3 s pulsations (Aoki et al. 1992). The optical counterpart is still unknown. A detailed discussion of BATSE observations has appeared elsewhere (Wilson et al. 1997). To date, BATSE has observed seven outbursts with durations of 30–70 days, the first five of which were spaced at 105–107 day intervals and the last two of which were unevenly spaced (Wilson et al. 1997). The eccentricity e and semimajor axis $a_x \sin i$, given in Table 3, are individually poorly determined owing to large spin-up torques during the outbursts, but $e \times a_x \sin i = 15_{-1}^{+6}$ lt-s is well constrained, thus establishing that the orbit is eccentric. This and the recurrent outburst behavior is strongly reminiscent of the Be transients, although GS 0834–430 falls below the Be-binary trend on the Corbet diagram (Fig. 4). Pulsations are seen in the energy range

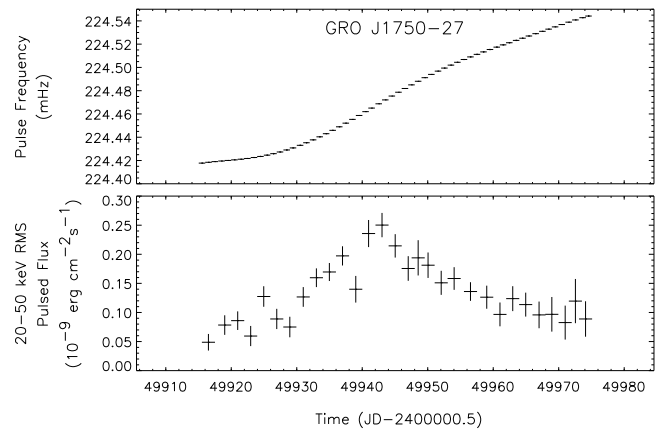


FIG. 20.—GRO J1750–27 spin frequency and pulsed flux measurements from BATSE. The intrinsic spin frequencies, which have been orbitally corrected using parameters from Scott et al. (1997), were determined at 1 day intervals from fits of phase measurements of the 20–50 keV DISCLA data (see Appendix B, § 1.3). The pulsed fluxes were determined at 1 day intervals by assuming an exponential spectrum with an e -folding energy of 20 keV (see Appendix B, § 2.3).

20–70 keV, and simultaneous 20–70 keV pulsed and Earth occultation DC flux measurements on 1991 June 15–28 (MJD 48,422–48,435), September 19–October 3 (MJD 48,518–48,532), December 15–27 (MJD 48,605–48,617), and 1992 July 16–29 (MJD 48,819–48,832) yielded consistent peak-to-peak pulsed fractions of 10%–15% and marginal evidence for an increase of pulsed fraction with energy. The pulse profiles vary with both energy and time (Wilson et al. 1997).

2S 1417–624.—*SAS-3* discovered 17.6 s pulsations from 2S 1417–624 in 1978 (Kelley et al. 1981a), and the companion was later identified to be a 17th mag OB star (Grindlay, Petro, & McClintock 1984). See Figure 22. Detailed discussion of BATSE observations have appeared elsewhere (Finger, Wilson, & Chakrabarty 1996b). BATSE observed a large outburst of 2S 1417–624 from 1994 August 29 to December 11 (MJD 49,593–49,697), followed by a sequence of five smaller outbursts of diminishing amplitudes occurring approximately every 40 days (Finger et al. 1996b),

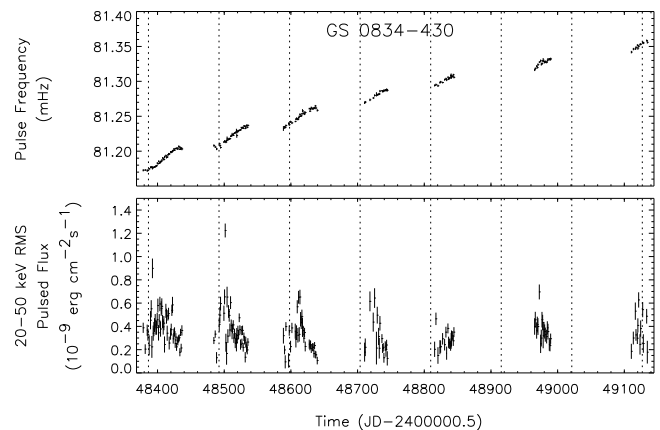


FIG. 21.—GS 0834–430 frequency and flux measurements from BATSE. The intrinsic spin frequencies, which have been orbitally corrected using parameters from Wilson et al. (1997), were determined at 1 day intervals from the power spectra of the 20–70 keV CONT data (see Appendix B, § 1.1). The pulsed fluxes were determined at 1 day intervals by assuming an exponential spectrum with an e -folding energy of 14 keV (see Appendix B, § 2.3).

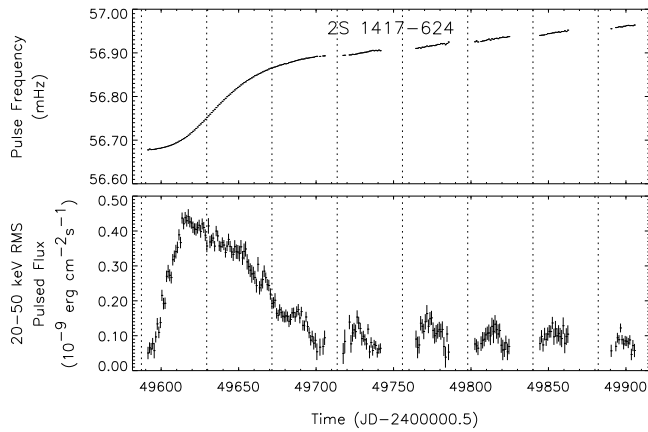


FIG. 22.—2S 1417–624 frequency and pulsed flux measurements from BATSE. The intrinsic spin frequencies, which have been orbitally corrected using parameters from Finger et al. (1996b), were determined at 1 day intervals by epoch-folding the 20–50 keV DISCLA data (see Appendix B, §1.2). The pulsed fluxes were determined at 1 day intervals by assuming a Comptonized spectrum model of the form $F(E) = AE^2 \exp(-E/kT)$, with $\lambda = 1.6$ and $kT = 11.9$ keV (Finger et al. 1996b) (see Appendix B, § 2.3). The orbit was determined assuming a correlation between pulsed flux and accretion torque, which could potentially introduce modulations in the apparent rate of spin-up during the sequence of outbursts following the main outburst.

and two later outbursts (not shown). At the peak of the initial outburst, pulsations were detected up to 100 keV. The pulse profile is double peaked, and the ratio of the flux in the two peaks changed systematically during the initial outburst. The binary orbit was measured by a pulse-timing analysis, assuming that the accretion torque was correlated with the measured pulsed flux. During the large outburst, the spin-up rate reached $\dot{\nu} \simeq 4 \times 10^{-11} \text{ Hz s}^{-1}$.

GRO J1948+32.—BATSE discovered and observed a single, 35 day outburst from the 18.7 s X-ray pulsar GRO J1948+32 from 1994 April 6 to May 12 (MJD 49,448–49,482) and localized the source to within 10 deg^2 (Chakrabarty et al. 1995a). See Figure 23. The pulse frequency showed a modulation suggestive of orbital variation over less than a full cycle. The 20–75 keV pulsed flux

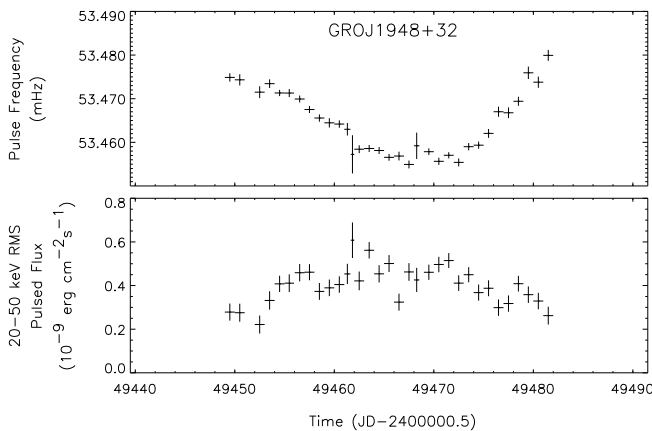


FIG. 23.—GRO J1948+32 frequency and pulsed flux measurements from BATSE. The pulse frequencies, which have not been orbitally corrected as the orbital parameters are unknown, were determined at 1 day intervals from the power spectra of the 20–70 keV CONT data (see Appendix B, § 1.1). The pulsed fluxes were obtained by assuming an exponential spectrum with an e -folding energy of 15 keV (see Appendix B, § 2.3).

reached a maximum of 50 mcrab on the fifth day of the outburst. There is evidence for spectral variability uncorrelated with time or intensity (Chakrabarty et al. 1995a). The system is probably a Be transient, although an orbit could not be uniquely measured and the companion has not been identified.

EXO 2030+375.—*EXOSAT* discovered 41.7 s pulsations from EXO 2030+375 during a strong outburst of ~ 80 day duration starting in 1985 May and observed a smaller outburst in 1985 October (Parmar et al. 1989). See Figure 24. The companion was later identified as a B0 Ve star (Coe et al. 1988). The *EXOSAT* observations found an orbital period of ≈ 46 days and a strong correlation of both the accretion torque and pulse shape with luminosity, although the orbit and accretion torque could not be separately measured.

Detailed discussions of the BATSE observations of EXO 2030+375 have appeared elsewhere (Stollberg et al. 1993a, 1994). During the interval 1992 February 8–1993 August 26 (MJD 48,661–49,226), 13 consecutive outbursts of EXO 2030+375 were seen with durations of 7–19 days, spaced at approximately 46 day intervals (Wilson et al. 1992; Stollberg et al. 1994). A few detections of marginal statistical significance preceded and followed the sequence of outbursts. Over these 13 outbursts, EXO 2030+375 spun up at a mean rate of $\dot{\nu}_s \simeq 1.3 \times 10^{-13} \text{ Hz s}^{-1}$. The pulse profile is double peaked with no evidence for spectral differences between the two peaks (Stollberg et al. 1993a) and no pulse profile variations as were seen by *EXOSAT* (Parmar, White, & Stella 1989). This sequence of outbursts has allowed the first unambiguous determination of the orbital parameters (Stollberg et al. 1994), shown in Table 3, which indicates that the outbursts all began at or shortly after periastron passage. The orbit measured with BATSE has been used to determine the correlation between luminosity, L , and accretion torque, N , in the *EXOSAT* 1985 May–August outburst, yielding a functional dependence $N \propto L^{1.2}$ (Reynolds et al. 1996).

The source was quiescent for 2.5 yr before being detected by BATSE again in 1996 April and May (Stollberg et al. 1996). These two outbursts occurred ~ 5 days prior to

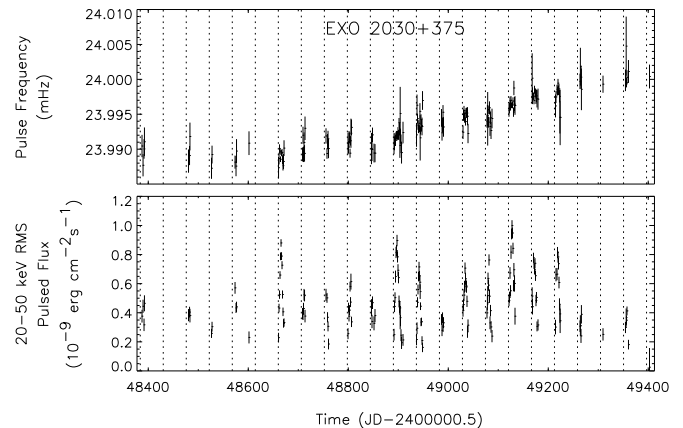


FIG. 24.—EXO 2030+375 frequency and pulsed flux measurements from BATSE. The intrinsic spin frequencies, which have been orbitally corrected using parameters from Stollberg et al. (1994), were determined at 1 day intervals from the power spectra of the 20–70 keV CONT data (see Appendix B, § 1.1). The pulsed fluxes were determined at 1 day intervals by assuming an exponential spectrum with an e -folding energy of 20 keV (see Appendix B, § 2.3).

periastron passage. The latest outbursts were detected in 1996 July and November. The spin frequency of the latest outbursts indicate that during quiescence EXO 2030+375 had spun down at a rate $\dot{\nu} \simeq -3.4 \times 10^{-14} \text{ Hz s}^{-1}$. Simultaneous 30–70 keV pulsed and Earth occultation DC flux measurements on MJD 49,120–49,131 yielded a peak-to-peak pulsed fraction of 0.36(5) (Stollberg et al. 1994).

GRO J1008–57.—BATSE discovered 93.5 s pulsations and observed a 33 day outburst from GRO J1008–57 (Stollberg et al. 1993b) from 1993 July 14 to August 16 (MJD 49,182–49,215). See Figure 25. A preliminary discussion of the BATSE observations of GRO J1008–57 appeared in Wilson et al. (1994b). The source was localized to $2^{\circ}5$ by the Earth-occultation technique (Stollberg et al. 1993b) and later by *OSSE* (Grove et al. 1993), *ASCA* (Tanaka 1993), and *ROSAT* (Petre & Gehrels 1993) to $15'$. Coe et al. (1994a) later identified the companion to be a Be star. GRO J1008–57 has a hard spectrum, with pulsations observed from 20 to 160 keV. The peak-to-peak pulsed fractions, averaged over the interval MJD 49,186–49,195, are 0.66(9) (20–30 keV), 0.65(7) (30–40 keV), 0.69(7) (40–50 keV), and 0.76(15) (50–70 keV). Four additional outbursts, not shown in Figure 25, were observed during 1994 March, 1994 November, and 1996 March. The very weak and short duration later outbursts occurred at multiples of ≈ 248 days, which indicates that this may be the orbital period of the system.

A0535+26.—*Ariel 5* discovered 103 s pulsations from A0535+26 in 1975 (Rosenberg et al. 1975; Coe et al. 1975), and its companion is the Be star HDE 245770 (Stier & Liller 1976; Hutchings et al. 1978). See Figure 26. The 111 day orbital period of A0535+26 was first inferred from the spacing of X-ray outbursts (Nagase et al. 1982). The binary undergoes frequent outbursts with a wide range of intensities, the brightest reaching 3 crab in the 2–10 keV band (Giovannelli & Graziati 1992).

Detailed discussions of BATSE observations of A0535+26 have appeared elsewhere (Finger et al. 1994a, 1996c). BATSE has observed six outbursts spaced roughly at the orbital period, the fourth of which is a “giant” outburst that occurred from 1994 January 28 to March 20

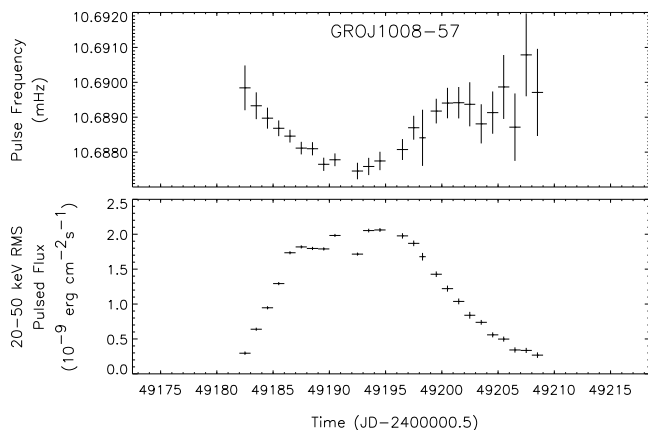


FIG. 25.—GRO J1008–57 frequency and pulsed flux measurements from BATSE. The pulse frequencies, which have not been orbitally corrected as the orbital parameters are unknown, were determined at 1 day intervals from the power spectra of the 20–70 keV CONT data (see Appendix B, § 1.1). The pulsed fluxes were determined at 1 day intervals by assuming an exponential spectrum with an e -folding energy of 20 keV (see Appendix B, § 2.3).

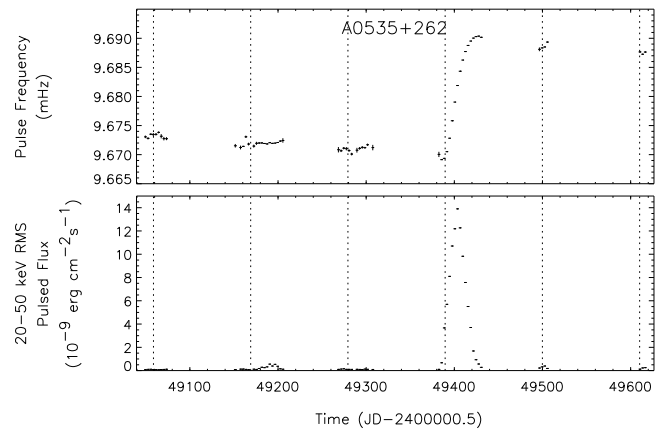


FIG. 26.—A0535+262 frequency and pulsed flux measurements from BATSE. The frequencies, which have been orbitally corrected using orbital parameters from Finger et al. (1994a), were determined at 3 day intervals from fits to phase measurements made using the 20–50 keV DISCLA data (see Appendix B, § 1.3). The pulsed fluxes were measured at 1 day intervals by assuming an exponential spectrum with an e -folding energy of 20 keV (see Appendix B, § 2.3).

(MJD 49,380–49,430) and reached a peak flux of 8 crab in the BATSE energy band. There was little or no spin-up during the normal outbursts, spin-down between outbursts, but rapid spin-up during the giant outburst, suggesting accretion from a disk. The giant outburst showed enough dynamic range that the relation between accretion torque and pulsed flux could be tested directly (see § 5.2).

BATSE has provided the first measurement of the binary orbit, and detection of quasi-periodic oscillations (QPOs) during the giant outburst (Finger et al. 1994a; Finger et al. 1996c). A cyclotron absorption line at 110 keV was reported by *OSSE* (Grove et al. 1995), which is also evident in the BATSE pulsed flux spectrum. The pulse shape is complex and highly variable with both energy and intensity as shown in Figure 27. Fluxes could be measured with the occultation method only during the giant outburst, and these yielded a 20–50 keV peak-to-peak pulsed fraction of > 0.8 at low flux and decreased to about 0.3 at the highest flux.

GRO J2058+42.—BATSE discovered 198 s pulsations and observed an initial 46 day outburst from GRO J2058+42 (Wilson et al. 1995a) from 1995 September 14 to October 30 (MJD 49,974–50,020). The source was localized to a $1^{\circ} \times 4^{\circ}$ error box with BATSE using both pulsed and Earth occultation data. *OSSE* scans further reduced the size of the error box to $30' \times 60'$ (Grove 1995), and a target-of-opportunity scan with the *RXTE* PCA in 1996 November reduced the error region to a $4'$ circle (Wilson, Strohmayer, & Chakrabarty 1996). The optical counterpart has not been determined. The total flux, as measured by Earth occultation, peaked at about 300 mcrab (20–50 keV). The large initial outburst was followed by a sequence of four much smaller outbursts with pulsed 20–50 keV fluxes peaking at 15–20 mcrab, the first three of which are shown in Figure 28. The outbursts were spaced by ≈ 110 days, which is likely to be the orbital period.

4U 1145–619.—*Ariel 5* discovered 292.5 s pulsations from 4U 1145–619 in 1977 (White et al. 1978). See Figure 29. The companion is the ninth mag Be star Hen 715 (Dower et al. 1978; Hammerschlag-Hensberge et al. 1980; Bianchi & Bernacca 1980), which exhibits emission lines

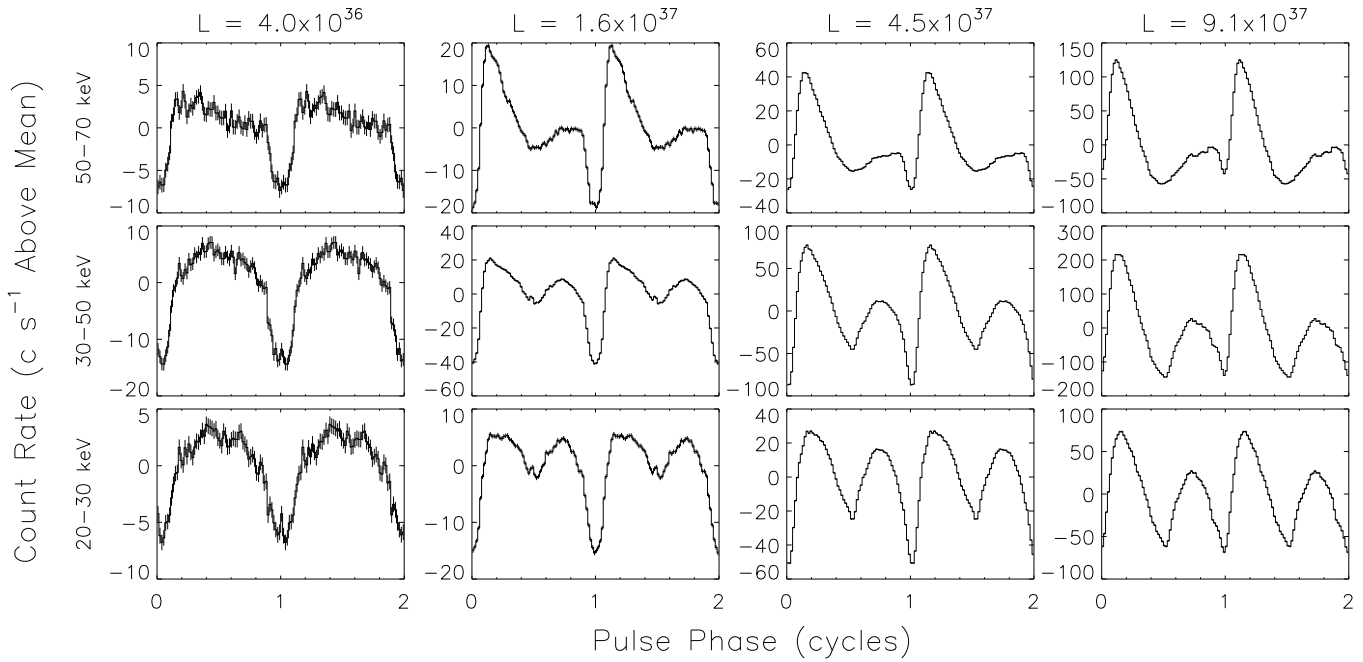


FIG. 27.—Pulse profile as a function of pulsed flux and energy for A0535+26. Pulse profiles of A0535+262 during the giant outburst in 1994 February–March, obtained by epoch-folding CONT data. Profiles in three energy bands are given for four time intervals. The mean luminosity L in ergs s^{-1} is given for each time interval. The time intervals are February 15.1–17.6 ($L = 9.1 \times 10^{37}$), February 25.0–March 1.5 ($L = 4.5 \times 10^{37}$), March 5.0–8.6 ($L = 1.6 \times 10^{37}$), and March 13.1–15.6 ($L = 4.0 \times 10^{36}$). Luminosities were calculated from 20–100 keV fluxes based on occultation measurements by assuming a distance of 2 kpc and assuming the 20–100 keV band contains 45% of the bolometric flux.

and has an equatorial rotational velocity of $v \sin i = 290 \text{ km s}^{-1}$ (Hammerschlag-Hensberge et al. 1980; Bianchi & Bernacca 1980). An orbital period of 186.5 days was inferred from the recurrence times of outbursts, which typically last ≈ 10 days (Watson, Warwick, & Ricketts 1981; Priedhorsky & Terrell 1983). Pulse frequency variations over multiple EXOSAT observations imply an eccentricity of $e \gtrsim 0.6$ (Cook & Warwick 1987). To date, BATSE has observed seven outbursts, of which three are shown. The separation between the BATSE outbursts is in good agreement with the 186.5 day period.

A1118–616.—*Ariel 5* discovered 406.5 s pulsations from A1118–616 in 1974 (Ives, Sanford, & Bell-Burnell 1975), and the optical companion was later identified to be the Be star He 3-640/Wray 793 (Chevalier & Ilovaisky 1975; Heinze 1976; Wray 1976). See Figure 30. Since the initial discovery, no outbursts were observed until BATSE detected one from 1991 December 30 to 1992 January 10 (MJD 48,621–48,633). This outburst reached a 20–70 keV pulsed intensity of $\approx 14 \text{ counts s}^{-1}$ on 1992 January 3, followed by approximately 50 days of erratic flaring behavior with a maximum on 1992 February 1 (MJD 48,654) (Coe

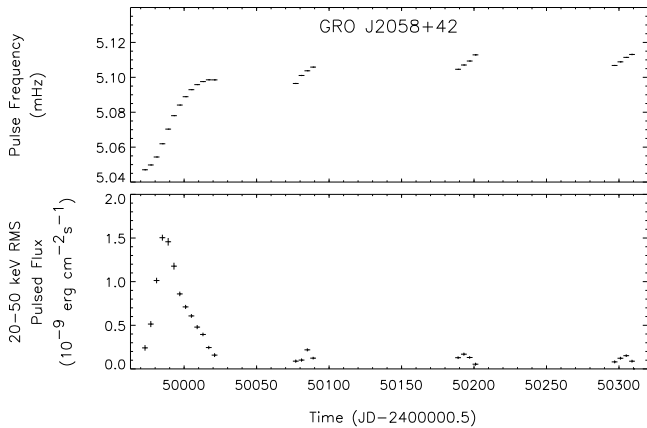


FIG. 28.—GRO J2058+42 frequency and pulsed flux measurements from BATSE. The spin frequencies, which have not been orbitally corrected as the orbital parameters are unknown, were determined at 4 day intervals by epoch-folding the 20–50 keV DISCLA data at a range of trial frequencies (see Appendix B, § 1.2). The pulsed fluxes were determined at 4 day intervals by assuming an exponential spectrum with an e -folding energy of 20 keV (see Appendix B, § 2.3).

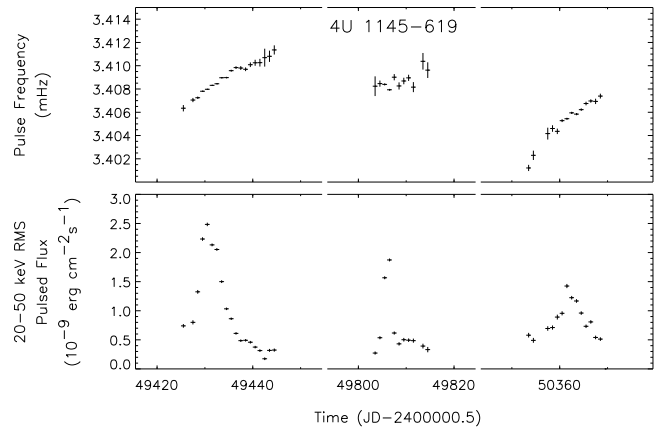


FIG. 29.—4U 1145–619 frequency and pulsed flux measurements from BATSE. The pulse frequencies, which have not been orbitally corrected as not all the orbital parameters are known, were determined at 1 day intervals from the power spectra of the 20–70 keV CONT data (see Appendix B, § 1.1). The pulsed fluxes were determined at 1 day intervals by assuming an exponential spectrum with an e -folding energy of 15 keV (see Appendix B, § 2.3).

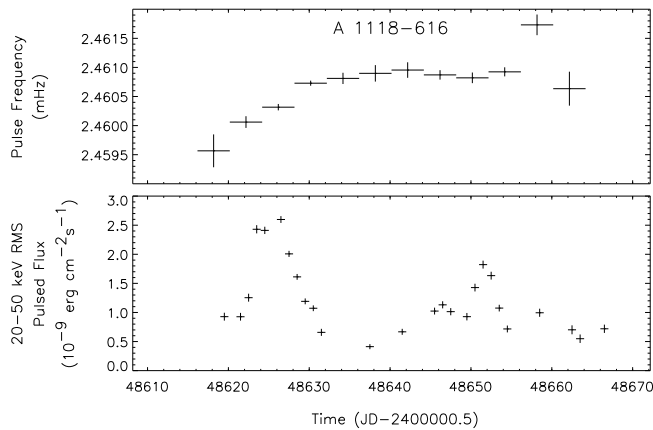


FIG. 30.—A118–616 frequency and pulsed flux measurements from BATSE. The spin frequencies, which have not been orbitally corrected as the orbital parameters are unknown, were determined by Coe et al. (1994b) at 4 day intervals by epoch-folding the 20–50 keV DISCLA data at a range of trial frequencies (see Appendix B, § 1.2). The pulsed fluxes were determined at 1 day intervals by assuming an exponential spectrum with an e -folding energy of 15 keV (see Appendix B, § 2.3).

et al. 1994b). The WATCH experiment on *Granat* independently detected and monitored the outburst (Lund, Brandt, & Castro-Tirado 1994), which was also observed by the *IUE* and ground-based telescopes (Coe et al. 1994b). The X-ray outburst was accompanied by an increase in H α emission and an IR excess, indicative of an extended disk around the companion star (Coe et al. 1994b). Pulsed emission is detected from 20 to 100 keV at the peak of the outburst.

5. DISCUSSION

The long-term, continuous all-sky monitoring of accreting pulsars by BATSE is providing new insight into these systems. In § 5.1, we show how BATSE observations have yielded a qualitatively different picture of the spin behavior of disk-fed pulsars on long timescales (\sim years) than understood from earlier measurements. BATSE has also been able to test theories of accretion torque on short timescales (\sim days) in transient pulsars (§ 5.2). BATSE observations of accretion torques in transient and wind-fed systems show evidence of spin-down during quiescence and of disk formation in a predominantly wind-fed binary (§ 5.3). Continuous monitoring of persistent systems makes it possible to quantify the variability of accretion torques on timescales of months to years using power spectra (§ 5.4). BATSE's continuous monitoring capability has also provided new insights into the properties of binaries containing pulsars that undergo transient outbursts (§ 5.5), the population of Be-transient pulsars (§ 5.6), and the evolution of B-star binaries into Be-transient accreting binary pulsars (§ 5.7).

5.1. The Long-Term Spin Evolution of Disk-fed Pulsars

The picture of long-term pulsar spin evolution developed in the mid-1970s was based on sparse measurements provided by pointed observations of ~ 10 objects (Rappaport & Joss 1977a; Ghosh & Lamb 1979). In particular, the spin behavior of Cen X-3 and Her X-1 at that time suggested that the simple spin-up torque estimate in equation (3) was sometimes inadequate: these pulsars were apparently spinning up on a timescale much longer than predicted by

equation (8). Moreover, both sources also underwent short episodes of spin-down, which indicates that angular momentum was actually being lost by the pulsar while it continued to accrete. The continuous pulse monitoring by BATSE, however, reveals that these early observations sometimes gave a false impression of the strength and continuity of the accretion torque.

The frequency history of the 4.8 s pulsar Cen X-3, shown in Figure 31, is an example of where BATSE observations reveal a strikingly different picture of pulsar spin behavior than had been previously hypothesized. Prior to 1991, the long-term frequency evolution (Fig. 31a) had been described as secular spin-up at $\dot{\nu} \simeq 8 \times 10^{-13}$ Hz s $^{-1}$ (a factor of ~ 5 slower than predicted by eq. [3]), superposed with fluctuations and short episodes of spin-down. In contrast, the more frequently sampled BATSE data (Fig. 31b) show that Cen X-3 exhibits 10–100 day intervals of steady spin-up and spin-down at a much larger rate, consistent with equation 3. Figure 32 is a histogram of torques observed in Cen X-3 showing a roughly bimodal distribution of torque states, with the average spin-up torque ($\sim +7 \times 10^{-12}$ Hz s $^{-1}$) larger in magnitude than the average spin-down torque (about -3×10^{-12} Hz s $^{-1}$). Transitions between spin-up and spin-down occur on a timescale more rapid than BATSE can resolve ($\lesssim 10$ days). The long-term spin-up rate inferred from the pre-BATSE data is not representative of the instantaneous torque; its small value is a consequence of the frequent transitions between spin-up and spin-down.

Interestingly, this switching behavior is very common. At least four of the eight persistent pulsars observed by BATSE show torque reversals between steady spin-up and steady spin-down. The 7.6 s pulsar 4U 1626–67 underwent a reversal to smooth spin-down at a rate $\dot{\nu} \simeq -7 \times 10^{-13}$ Hz

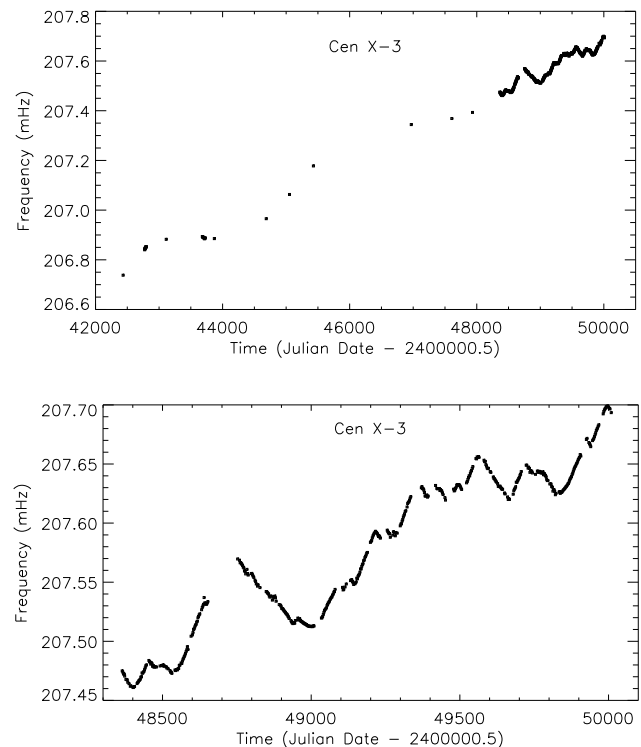


FIG. 31.—Frequency histories of Cen X-3. *Upper panel*: The long-term frequency history of Cen X-3. *Lower panel*: High-resolution BATSE measurement of the intrinsic spin frequencies of Cen X-3.

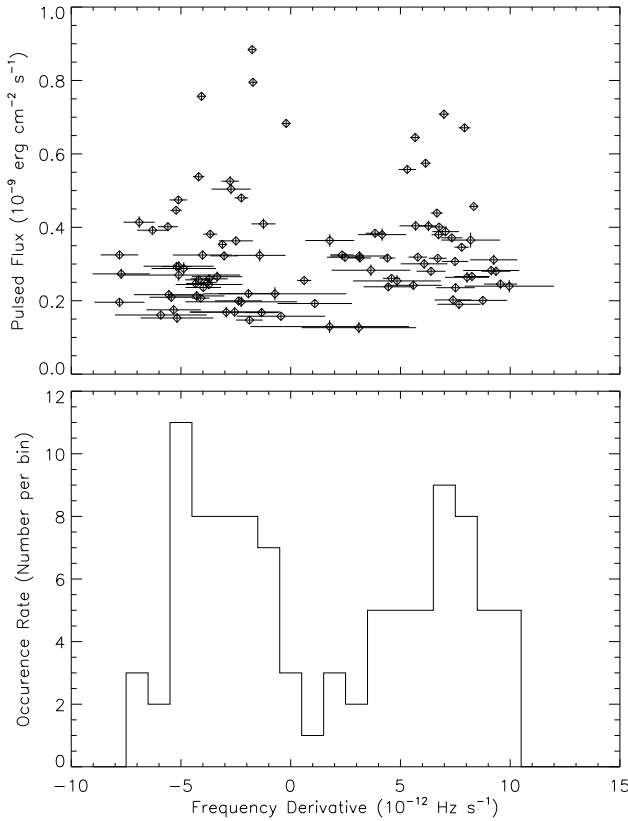


FIG. 32.—The Cen X-3 spin-up is plotted vs. the 20–50 keV pulsed flux in the top panel. The bottom panel shows the Cen X-3 spin-up rate distribution. The fluxes used are 10 day averages. The spin-up rates are from linear fits to the frequency measurements within the same 10 day intervals. No clear correlation is seen between spin-up rate and flux. The spin-up rate distribution is clearly bimodal.

s^{-1} in 1991 after two decades of smooth spin-up with $\dot{\nu} \simeq +8.5 \times 10^{-13} \text{ Hz s}^{-1}$ (Chakrabarty et al. 1997a). Most surprisingly, the final torque is nearly equal in magnitude but opposite in sign. A similar transition to spin-down was observed in the 120 s pulsar GX 1+4 in 1988 (Makishima et al. 1988) after more than a decade of steady spin-up (Fig. 6). Again, the spin-down rate ($\sim 3.7 \times 10^{-12} \text{ Hz s}^{-1}$) is close in magnitude to the spin-up rate. In the 38 s pulsar OAO 1657–415, both the duration and strength of torque episodes are very close to those seen in Cen X-3 (Chakrabarty et al. 1993). Of the remaining four systems, Her X-1 is sampled infrequently at 35 day intervals so that we cannot measure its torque on short timescales, while the other three (4U 1538–52, GX 301–2, Vela X-1) are wind-fed pulsars.

There are at least two classes of models that might explain instantaneous spin-down in disk-fed pulsars, and both involve the magnetic interaction between the accretion disk and the stellar magnetosphere. Ghosh & Lamb (1979) argued that Her X-1 and Cen X-3 must be near an equilibrium at which the star rotates at a spin frequency nearly equal to the Keplerian frequency of the magnetosphere, $\Omega_{\text{spin}} \simeq \Omega_{\text{K}}(r_m) = (GM/r_m^3)^{1/2}$. They found that additional *negative* torques would then act on the star: magnetic field lines that thread the disk beyond the corotation radius (where the disk rotates more slowly than the star) are swept back in a trailing spiral and transport angular momentum outward. Stars sufficiently close to equilibrium can spin down while continuing to accrete. Other models attempt to

explain spin-down via the loss of angular momentum in a magnetohydrodynamic outflow (Anzer & Borner 1980; Arons et al. 1984; Lovelace, Romanova, & Bisnovatyi-Kogan 1995). Outflowing material moves along rigid magnetic field lines like beads on a wire, gaining angular momentum from the star as it is forced to corotate. This results in a stellar spin-down torque $N \sim \dot{M}_w (GM r_\alpha)^{1/2}$, where \dot{M}_w is the loss rate in the wind and r_α is the Alfvén radius in the flow beyond which the magnetic field is dynamically unimportant.

The BATSE observations pose a number of difficulties for these models. To produce the bimodal torque behavior we observe, most if not all near-equilibrium models apparently require step function–like changes in the mass accretion rate—finely tuned just so that the two torques states have comparable magnitude but opposite sign. The many transitions in Cen X-3, for example, *always* alternate between torques of opposite sign: How does the companion star know just how to change its mass transfer rate so that transitions between two torques of the same sign never occur? It seems especially implausible in a system like 4U 1626–67, in which the average mass accretion rate is likely determined by the loss of orbital angular momentum via gravitational radiation, that the companion would switch to such a finely tuned mass transfer rate that the spin-down torque would have nearly the same magnitude as the previous spin-up torque (Chakrabarty et al. 1997a). Since the timescale for angular-momentum loss via gravitational radiation is much longer than the timescale of BATSE observations, changes in mass accretion rate must be due to physical changes in the star or accretion disk.

Our observations suggest that disk-accreting pulsars are subject to instantaneous torques of magnitude $\approx N_0 \equiv \dot{M}(GM r_{\text{co}})^{1/2}$ (see eq. [6]) and differentiate themselves only by the timescale for reversals of sign. We see some (e.g., Cen X-3) that switch within ~ 10 –100 days, whereas others (e.g., 4U 1626–67 and GX 1+4) switch once in 10–20 yr. The primary theoretical issues are then identifying the physics that sets this timescale and understanding why the magnitudes of the spin-up and spin-down torques are so similar.

It is intriguing to apply our picture of the long-term evolution of disk-fed pulsars to those we cannot observe with BATSE. First, it makes it more plausible that one of the class of pulsars that are spinning down (1E 2259+586, 1E 1048.1–5937, and 4U 0142+61; see Mereghetti & Stella 1995) might eventually switch to spin-up. The pulsar 1E 1048.1–5937 has the shortest spin-down time among these ($t_{\text{sd}} \simeq 10^4$ yr) and might be the most likely one to undergo a torque reversal. There is already some evidence for a brief torque reversal in 1E 2259+586 (Baykal & Swank 1996). The long-term torque inferred for LMC X-4 is nearly a factor of 100 lower than N_0 , which suggests that this pulsar may be undergoing rapid switching like Cen X-3.

5.2. Torque and Luminosity of Transient Pulsars

Short-term instantaneous torque measurements—not long-term averages—are necessary to test accretion torque theory. All such theories predict that the magnetospheric radius should decrease as \dot{M} increases, and the simplest version (eq. [4]) predicts $r_m \propto \dot{M}^{-2/7}$ for $r_m < r_{\text{co}}$. This implies that a pulsar should spin up at a rate $\dot{\nu} \propto \dot{M}^{6/7}$. In principle, we can test this prediction by measuring the correlation between torque and bolometric luminosity. Luminous outbursts in GRO J1744–28 and A0535+262

seen with BATSE showed enough dynamic range that the relation between torque and *observed* flux could be tested directly (Finger et al. 1996a, 1996b). In addition, the orbital parameters of EXO 2030+375 measured with BATSE made it possible to compute the accretion torque from a luminous 1985 outburst seen by *EXOSAT* (Reynolds et al. 1996). Figure 33 shows the spin-up rate of A0535+26 versus 20–100 keV flux (*upper panel*) and the spin-up rate of GRO J1744–28 versus 20–50 keV rms pulsed flux (*lower panel*). Also plotted are the power laws $\dot{\nu} \propto F_{\text{obs}}^\gamma$ with $\gamma = \frac{6}{7}$ (*dotted line*) and the best-fit power laws (*dashed line*). The best-fit index for A0535+262 is 0.951(26) and that for GRO J1744–28 is 0.957(26). A similar fit to the 1985 outburst of EXO 2030+375 gave $\gamma \simeq 1.2$ (Reynolds et al. 1996).

All three systems suggest a larger γ than the naive prediction of $\gamma = \frac{6}{7}$. In particular, the system with $\gamma > 1$, indicates an *increase* in r_m with \dot{M} , if it is proportional to the measured flux. However, one must remember that BATSE does not measure bolometric flux but only the 20–50 keV pulsed flux. In addition, the large changes in beaming fraction implied by the changing pulse profiles need to be modeled and accounted for. The observed flux may thus be related

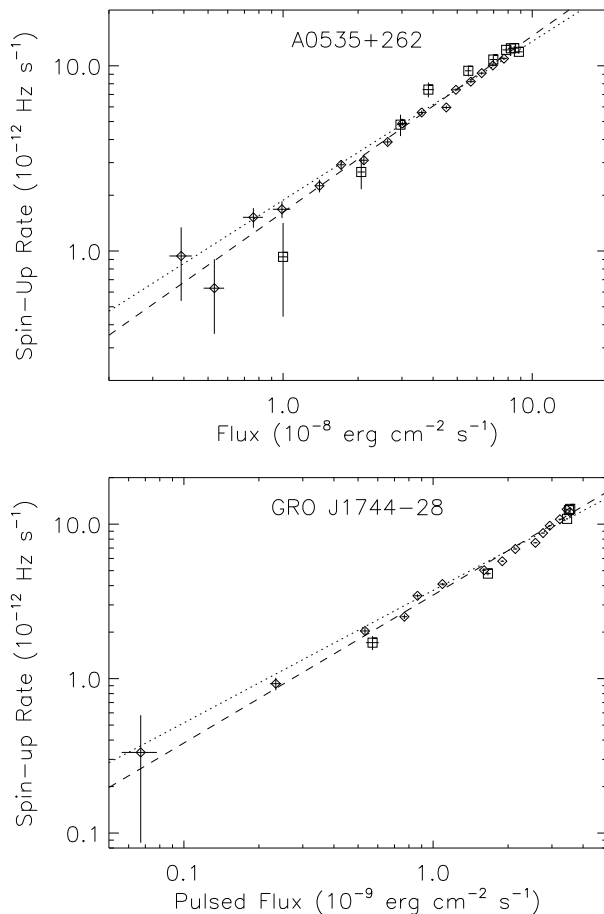


FIG. 33.—Observed relationships between flux and pulsar spin-up rate $\dot{\nu}$. The upper panel shows the spin-up rate of A0535+262 during the 1994 giant outburst vs. the measured total 20–100 keV flux, determined from Earth occultation measurements. The bottom panel shows the spin-up rate of GRO J1744–28 during the 1995 December–1996 March outburst vs. the 20–50 keV rms pulsed flux. For both sources, the square symbols are from the outburst rise, and the diamond symbols are from the outburst decline. The dotted curves are power laws with the expected index of 6/7, while the dashed curves are best-fit power laws. The best-fit index for A0535+262 is 0.951(26), and that for GRO J1744–28 is 0.957(26).

nonlinearly to the mass accretion rate and thus contaminate the measurement of γ . *EXOSAT* measured the 1–10 keV flux from EXO 2030+375; since this should be a good tracer of the bolometric flux, changing only the beaming could have affected their measured γ .

The difficulties in determining the mass accretion rate from the observed flux point out the necessity for testing the scaling $r_m \propto \dot{M}^{-2/7}$ in a way that does not depend on the uncertain bolometric corrections. An indirect test was possible during a giant outburst in A0535+26, when a simultaneous QPO was detected (Finger et al. 1996c). The centroid frequency of the QPO was strongly correlated with the observed spin-up torque and luminosity, varying in the range $\nu_{\text{QPO}} = 30\text{--}70$ mHz. Interpreting the QPO frequency as the Kepler frequency at the inner disk boundary (Alpar & Shaham 1985; Lamb et al. 1985), we expect $\nu_{\text{K}} = (GM/4\pi^2 r_m^3)^{1/2} \propto \dot{M}^{3/7}$. Consequently, with this interpretation for the QPO, one expects $\dot{\nu} = \dot{M}(GMr_m)^{1/2} \propto \nu_{\text{QPO}}^2$. This predicted relationship agrees with the observed trend in the data (Finger et al. 1996c). An alternative interpretation of the QPO as the beat frequency between the inner disk and the rotating magnetosphere, $\nu_{\text{QPO}} = \nu_{\text{K}} - \nu$, gives an equally good fit. This correlation between the torque and QPO frequency is the strongest evidence to date supporting the simple spin-up accretion torque model described in § 3.

To summarize, the observational evidence supporting the simplest picture of accretion torques described in § 3 is mixed. In all cases of persistent disk-fed pulsars, the *magnitude* of the accretion torque is consistent with the large lever arm of an extended magnetosphere. The observed correlation between torque and flux, however, does not confirm the expected scaling $\dot{\nu} \propto \dot{M}^{6/7}$. It is presently unclear if this disagreement can be due to bolometric and/or beaming corrections. On the other hand, if one presumes that the observed QPO in the outburst of A0535+26 scales with the Keplerian frequency at the magnetosphere, then the data are consistent with the expected magnetosphere relationship, $r_m \propto \dot{M}^{-2/7}$. Further progress on these important issues requires simultaneous torque, bolometric flux, and pulse profile measurements. Since BATSE continuously monitors the torque, a series of well-timed observations with a broadband X-ray telescope for many of these objects is needed.

5.3. Accretion Torques in Transient and Wind-fed Pulsars

Before BATSE, it was already known that the spin frequency in some transients decreases between outbursts. We have unambiguously seen spin-down between outbursts in A0535+26 at a rate $\dot{\nu} = -2.2(6) \times 10^{-13} \text{ Hz s}^{-1}$ (Finger et al. 1994a). This may be due to the propeller effect (Illarionov & Sunyaev 1975), when \dot{M} becomes small enough so that the magnetospheric radius exceeds the corotation radius. Accretion is then centrifugally inhibited, and material may become attached to magnetic field lines and flung away, removing angular momentum and causing the star to spin down. Unfortunately, we can make these measurements only in those binaries for which the orbit is known, which among the Be transients are still few.

In 1984, after a decade of erratic spin behavior, the persistently accreting pulsar GX 301–2 appeared to be spinning up steadily at $\dot{\nu} \simeq 2 \times 10^{-13} \text{ Hz s}^{-1}$. This trend was based on only three measurements, however. Continuous BATSE observations found that GX 301–2 was generally undergoing the stochastic torque fluctuations expected

from a wind accretor. However, two dramatic episodes of spin-up of ~ 20 days duration at $\approx 5 \times 10^{-12}$ Hz s $^{-1}$, comparable to the spin-up rates in the disk-fed systems Cen X-3 and GX 1+4, occurred accompanied by enhanced luminosity (Koh et al. 1997). Moreover, these two spin-up events produced a net change in spin frequency consistent with the long-term trend previously reported. These observations strongly suggest that GX 301–2 is primarily a wind-fed pulsar and that the secular trend is due to a few short but large spin-up episodes, possibly caused by the creation of transient accretion disks. This result blurs the common distinction between disk-fed and wind-fed pulsars.

5.4. Power Spectra of Torque Fluctuations

The power density spectrum of torque fluctuations in accreting pulsars can potentially provide a probe of both the accretion flow and the internal structure of neutron stars (Lamb, Pines, & Shaham 1978). The most crucial requirement for this type of study is a lengthy time baseline of precise timing observations, with sampling over a wide range of timescales. Pre-BATSE estimates have been made of the power spectrum of the spin frequency derivative, $\dot{\nu}$, of Vela X-1 (Deeter et al. 1989), a wind accretor, and of Her X-1 (Deeter 1981), a low-mass disk-fed system. Both showed the power spectrum of $\dot{\nu}$, $P_{\dot{\nu}}(f)$, to be flat, which indicates white torque noise with the neutron star responding as a solid body in the range of accessible analysis frequencies, f . To avoid confusion with the spin frequency, ν , we use the term “analysis frequency” for the argument of the power spectrum. The power spectral density $P_{\dot{\nu}}(f)$ gives the contribution to the variance of $\dot{\nu}$ per unit analysis frequency at analysis frequency f . White torque noise is expected in wind-fed systems, where simulations show that transient accretion disks with alternating rotational sense form and dissipate on timescales of approximately hours (Taam, Fryxell, & Brown 1988; Fryxell & Taam 1988).

Studies of torque noise have also been made using time domain analyses, which are equivalent to estimating simple power spectral models. A study was made by Baykal & Ögelman (1993) applying a time domain model of the frequency noise, a first-order Markov process, to the published frequency histories of a wide range of accretion-powered pulsars. This model has two parameters, the noise strength and the correlation time. For a correlation time of zero, the model represents white noise in spin frequency or equivalently blue noise ($P_{\dot{\nu}} \propto f^2$) in $\dot{\nu}$. For an infinite correlation time, the model represents a random walk in spin frequency, or equivalently white noise in $\dot{\nu}$. For the systems Her X-1, Cen X-3, and Vela X-1, they concluded that the $\dot{\nu}$ noise was white. Applying this assumption to the other sources, they found the noise strength correlated with source luminosity and long-term spin-up rate. De Kool & Anzer (1993) studied how the size of frequency changes in accretion pulsars depended on the time between measurements. They concluded the frequency behavior of Vela X-1 was consistent with a random walk in spin frequency or equivalently that the power spectrum of frequency fluctuations was $P_{\dot{\nu}}(f) \propto f^{-2}$. They found the frequency behavior of Her X-1 and Cen X-3 consistent with random walks plus long-term linear trends.

For each of the eight persistent sources monitored by BATSE, we have estimated the power spectrum of the spin frequency derivative by applying the Deeter polynomial estimator method (Deeter 1984) to our frequency measure-

ments. These power spectra are shown in Figure 34. We plot $P_{\dot{\nu}}(f)$, the contribution per hertz to the variance in $\dot{\nu}$ as a function of analysis frequency, f . $P_{\dot{\nu}}(f)$ is normalized such that $\int_0^\infty P_{\dot{\nu}}(f)df = \langle(\dot{\nu} - \bar{\dot{\nu}})^2\rangle$. The power due to measurement noise has been subtracted from the estimates and is shown independently by the square symbols.

The square root of the integrated power over a range in analysis frequency gives the root mean square (rms) amplitude of variations in $\dot{\nu}$ in that frequency range. This is shown in Table 5, where the integration range $[f_1, f_2]$ in analysis frequency is chosen as the range in which measurement errors do not dominate.

Each estimate is made by dividing the spin frequency measurements into intervals of duration T and fitting the frequencies with a quadratic polynomial in time. The square of the second-order term is divided by the value it would have for unit strength white noise in $\dot{\nu}$, defined as $P_{\dot{\nu}}(f) = 1$. The average over intervals is the power estimate. The procedure is repeated for different durations T to obtain a power spectrum. This polynomial estimation technique is essentially equivalent to using a polynomial instead of a sinusoid to estimate the power at each timescale T . While correctly addressing the difficulties cause by nonuniformly sampled data and red-noise power spectral components, this technique produces power spectra of low resolution.

The frequency response of this estimate of $P_{\dot{\nu}}(f)$ peaks near an analysis frequency $f \sim 1/T$. We plot $P_{\dot{\nu}}(f)$ at the logarithmic mean analysis frequency of the estimator response.

These quadratic estimators are by design independent of linear trends in frequency. Chakrabarty et al. (1997a) found a quadratic trend in the frequency of 4U 1626–67, which was too large to be due to the measured torque noise. For 4U 1626–67 we have therefore instead used cubic estimators, making the power spectral estimates independent of quadratic trends in the frequency.

For Vela X-1 and Her X-1, we find $P_{\dot{\nu}}$ consistent with white torque noise in agreement with previous results (Deeter et al. 1989; Deeter 1981). The power spectra of 4U 1538–52 (Rubin et al. 1997) and GX 301–2 are also consistent with white torque noise. In contrast, the power spectra of Cen X-3 (Finger 1994b), OAO 1657–415, and GX 1+4 (Chakrabarty et al. 1997b) show red torque noise with $P_{\dot{\nu}}$ varying approximately as f^{-1} . These red power spectra imply long-term correlations in the torque, which

TABLE 5
ROOT MEAN SQUARE SPIN DERIVATIVES FOR PERSISTENTLY ACCRETING NEUTRON STARS

Source	f_1^a	f_2^b	$\dot{\nu}_{\text{rms}}^c$
Cen X-3	3.4	60.0	65.7(35)
OAO 1657–415	12.0	19.0	55.8(36)
GX 1+4	7.3	20.0	26.2(31)
GX 301–2	5.0	21.0	13.9(8)
Her X-1	3.4	3.8	3.7(9)
Vela X-1	6.9	6.6	1.2(3)
4U 1538–52	4.0	6.0	1.0(1)
4U 1626–67	11.0	0.38	0.06(3)

^a Lower analysis frequency for calculation of $\dot{\nu}_{\text{rms}}$, in units of 10^{-9} Hz.

^b Upper analysis frequency for calculation of $\dot{\nu}_{\text{rms}}$, in units of 10^{-7} Hz.

^c Root mean squares frequency derivative in units of 10^{-13} Hz s $^{-1}$, obtained by integrating the power spectral density, $P_{\dot{\nu}}(f)$, from f_1 to f_2 .

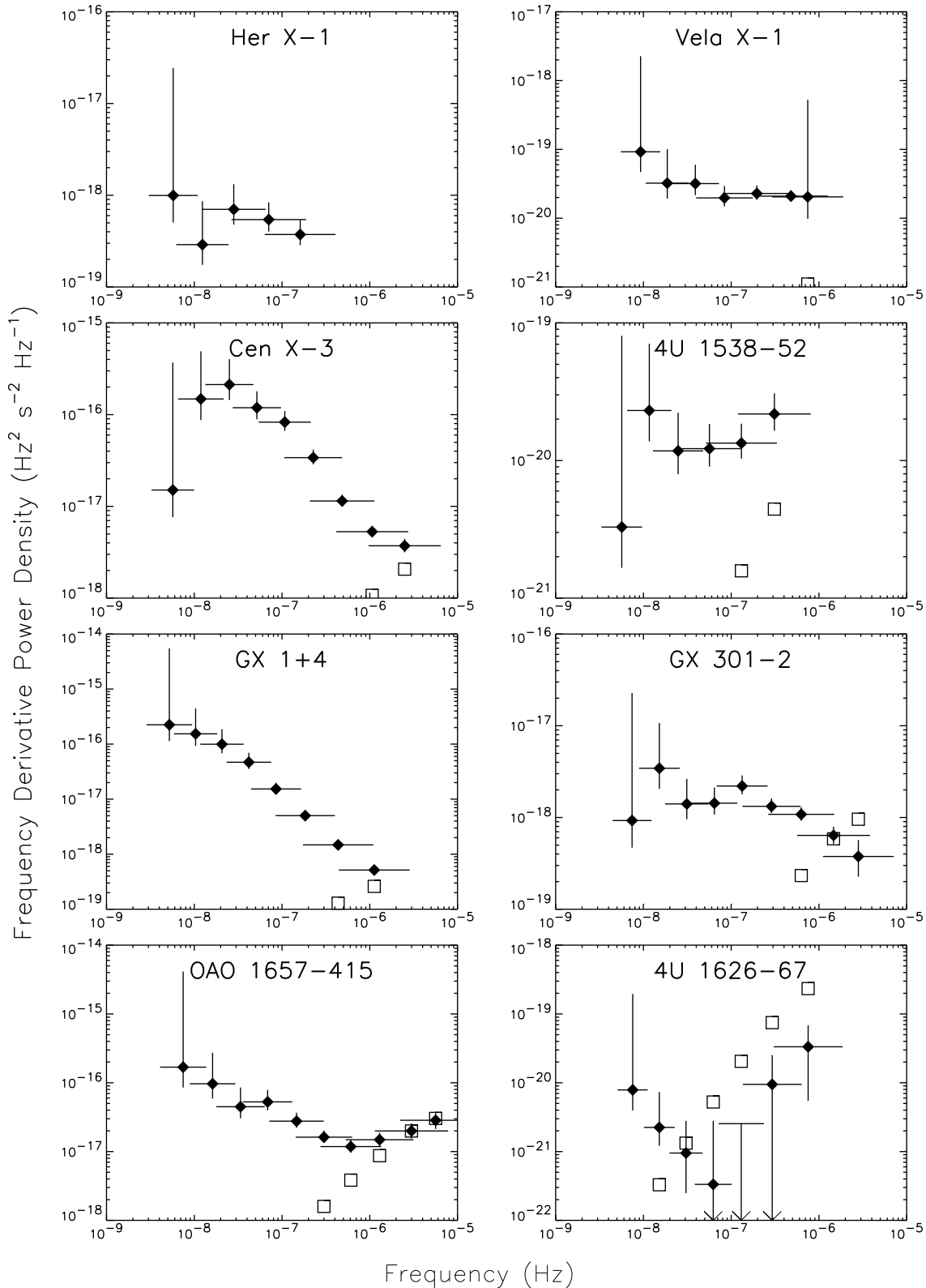


FIG. 34.—Power density spectra of torque fluctuations in persistent pulsars, computed using methods described in Deeter et al. (1987). Open squares indicate power from apparent torque variations introduced by counting noise, which have been subtracted from all measured values. The integrated rms torque variations for these observations are provided in Table 5.

are evident in the BATSE frequency histories. Owing to the low noise level in 4U 1626–67, only limited conclusions can be reached about the shape of its power spectrum (Chakrabarty et al. 1997a). Because Her X-1 is sampled only

once per 35 day cycle, we can only measure $P_{\dot{\nu}}$ for $f \lesssim 2 \times 10^{-7}$ Hz. These power spectra have poor frequency resolution, and unresolved narrow features may be present, affecting the continuum shape.

The measured red torque noise in Cen X-3 contradicts the conclusions based on time domain analyses of published frequencies. In retrospect, it is clear that the model used by Baykal & Ögelman (1993) cannot represent a red \dot{v} spectrum and therefore cannot discriminate between white and red torque noise. The de Kool & Anzer (1993) result may just be due to the poor sampling in the published frequency history. Since many of the power spectra we have measured have red torque noise, the meaning of the noise strengths determined by Baykal & Ögelman (1993), which assumed a random walk in \dot{v} , is now unclear. The sampling in the frequency histories of the pulsars they examined differs from source to source, and hence $P_{\dot{v}}$ is being addressed in a different range of analysis frequencies for each source. The results for sources can thus only be intercompared if the power spectra are all white. For red power spectra, correlations between luminosity and sampling density could lead to correlations between luminosity and estimated noise strength.

As a probe of the nature of the accretion flow, the low-resolution power spectra presented here are a mixed success. The sources known to be wind accretors (Vela X-1, 4U 1538–52, and GX 301–2) have power spectra consistent with white torque noise with strengths in the range 10^{-20} to 10^{-18} $\text{Hz}^2 \text{s}^{-2} \text{Hz}^{-1}$. For disk-fed pulsars with low-mass companions (Her X-1 and 4U 1626–67), the power spectra are consistent with white \dot{v} noise with strengths in the range 10^{-21} to 10^{-18} $\text{Hz}^2 \text{s}^{-2} \text{Hz}^{-1}$. However, we cannot rule out red noise in either system. The low power in 4U 1626–67 precludes our determining the slope of $P_{\dot{v}}$. In the case of Her X-1, the power spectrum does not span as large a range in analysis frequency as in the other sources. The one known disk-fed pulsar with a supergiant companion, Cen X-3, has a red \dot{v} power spectrum, reaching powers of 10^{-16} to 10^{-18} $\text{Hz}^2 \text{s}^{-2} \text{Hz}^{-1}$ at low frequencies. For GX 1+4 and OAO 1657–415, there is no evidence independent of their frequency histories that reveal the presence or absence of accretion disks.

5.5. Transients Outbursts in Be Systems

More than 50 outbursts from 12 transient pulsars were detected with BATSE in the first 5 years of observations, the times of which are shown in Figure 17. One of these transient sources, GRO J1744–28, has a low-mass companion. Seven of the remaining pulsars have known Be star companions. No optical counterparts have been identified for four of the other sources; however, their temporal behavior suggests that the companions are Be stars. Accreting neutron stars in Be systems typically have long periods and eccentric orbits. The source of accreting material is the slow, dense, stellar wind that is thought to be confined to the equatorial plane of the rapidly rotating Be star. Evidence for this equatorial disk in Be stars comes from observations of hydrogen and helium emission lines and an IR continuum excess. For a review of these Be/X-ray binary systems, see van den Heuvel & Rappaport (1987) or Apparao (1994).

A striking feature of the long-term light curves of these pulsars is the frequent occurrence of a series of outbursts. An example is the long series of outbursts from EXO 2030+375 shown in Figure 24, each outburst beginning soon after periastron (shown by dotted lines). Other examples are A0535+262 (shown in Fig. 26), GRO J2058+42 (Fig. 28), 2S 1417–624 (Fig. 22), and the series of outbursts of GS 0834–430 (Fig. 21) that begin with orbital spacing

but do not end with it. Another feature of the light curves is the occasional “giant” outburst. An example is the giant outburst of A0535+262 (Fig. 26) that occurred in 1994 February/March. Other examples are the first outburst observed from 2S 1417–624 (Fig. 22) and the first outburst observed from GRO J2058+42. As well as being bright, these giant outbursts have high spin-up rates and longer durations, and while often beginning at the same orbital phase as the smaller outburst, they tend to peak at a later phase.

These two types of outbursts have been noticed previously. Stella et al. (1986) contrasted the 1973 outburst of V0332+53 (which lasted over three binary orbits) with a series of three smaller outbursts detected in 1983–1984. They defined two classes of outburst activity: class I was periodically occurring outbursts associated with periastron passage, and class II was irregular transient activity, with higher luminosity and outbursts peaking at arbitrary orbital phases. Motch et al. (1991) classified outbursts of A0535+262 as giant, normal, or missing (i.e., no detection at the expected X-ray maxima). The more luminous giant outbursts peak at a phase delayed relative to the mean normal outburst X-ray maximum by up to 0.3 orbital cycles and were associated with large pulse period changes. Prior to BATSE, no association had been observed between giant and normal outbursts. BATSE has found that many of the giant outbursts are in the middle of, or followed by, a series of normal outbursts. A sequence of normal outbursts from 4U 0115+634 has now been seen by both BATSE and *RXTE*. Prior to these observations, only isolated giant outbursts had been seen.

Several authors have suggested that transient accretion disks are formed during the giant or class II outbursts (Kriss et al. 1983; Stella, White, & Rosner 1986; Motch et al. 1991). This helps explain the large and steady spin-up rates seen during the giant outbursts, which are difficult to explain with direct wind accretion. BATSE has observed peak spin-up rates of 4.3×10^{-11} Hz s^{-1} (2S 1417–624), 3.8×10^{-11} Hz s^{-1} (GRO J1750–27), 1.2×10^{-11} Hz s^{-1} (A0535+26), and 8×10^{-12} Hz s^{-1} (4U 0115+634). The discovery outburst of EXO 2030+375 found it spinning up at a rate of 2.2×10^{-11} Hz s^{-1} (Reynolds et al. 1996). Additional evidence for disk accretion occurring during giant outbursts is provided by the BATSE observations of beat or Keplerian frequency QPO during a giant outburst of A0535+262 (Finger et al. 1996c). Optical observations have so far been unable to provide evidence of accretion disks during the giant outbursts.

Given that an accretion disk seems to be present, it is natural to ask about its fate. Is it completely consumed at the end of a giant outburst, or is some portion of it left? Accretion may be centrifugally inhibited at the end of the outburst, when the magnetosphere lies outside of the corotation radius. It is unclear how efficient this mechanism is when the magnetosphere is still close to the corotation radius (Spruit & Taam 1993). If the ejected material does not acquire escape velocity, it might not leave the system but may continue to circulate around the neutron star.

If a disk can be sustained between giant outbursts, then it is plausible that one is present during normal outbursts. In this case, the repeating normal outbursts might be explained by the large tidal torques experienced by the disk during periastron passage. The angular momentum of material flowing into a disk must eventually be removed by

tidal torques from the companion, and these torques increase rapidly with decreasing pulsar-companion separation (Papaloizou & Pringle 1977). The enhanced torque in the outer disk shrinks the disk and increases the mass accretion rate there. This results in a wave of new material that will reach the inner disk on a global viscous timescale (\sim weeks for typical binary parameters). This could explain the series of normal outburst that were observed following the giant outburst in 2S 1417–624 (all of which peaked near apastron) as well as the sequence of outbursts in GRO J2058+42. It may also explain series of normal outbursts that are not preceded by a giant outburst, such as those seen from EXO 2030+375.

What causes the giant outbursts? Possibilities that have been investigated are episodes of enhanced Be disk density, or reduced Be disk expansion velocity. However, these should result in consistent correlations between optical and hard X-ray activity, which is typically not seen. For example, *UBVR*JHK band photometry of the HD 245770/A0535+262 system over the past decade (Clark et al. 1997) reveals no correlation between the photometric light curves and hard X-ray outbursts. Recently it has been proposed that the thermal disk instability thought to cause dwarf nova outbursts also is at work in soft X-ray transients (Smak 1983; van Paradijs 1996; King, Kolb, & Burderi 1996). This instability should also affect accretion disks around Be/X-ray pulsars and could be the cause of the giant outbursts. For an accretion disk to be vulnerable to this instability, the outer portion of the disk must be below the hydrogen ionization temperature ($T_H \approx 6500$ K) while the disk accumulates. For A0535+262, we find that for a steady accretion rate of $3 \times 10^{-10} M_\odot \text{ yr}^{-1}$, which corresponds to the average luminosity during the 600 day interval during which outbursts were observed by BATSE, the portion of the (X-ray-heated) disk beyond 10^{11} cm would still be neutral. The disk would extend to approximate 90% of the Roche lobe at periastron, or 2×10^{12} cm, and would therefore be subject to this instability once a critical amount of matter has accumulated.

5.6. The Population of Be Transients

The Galactic population of Be transients has been estimated before by Rappaport & van den Heuvel (1982) and Meurs & van den Heuvel (1989), who both arrived at a number of several thousand. However, the sparse and non-uniform coverage of pre-BATSE instruments resulted in several nonquantifiable ambiguities in their analysis. The continuous, uniform, and all-sky coverage provide by BATSE alleviated some of these problems and enables us to check previous estimates of the Galactic Be-transient population.

BATSE has detected 11 transients with high-mass companions (mostly Be stars) between 1991 April and 1997 January (MJD 48,370–50,464). This is a complete sample at 20–50 keV of transient sources with pulsed fluxes in excess of $F_{\min} \approx 2 \times 10^{-10} \text{ ergs cm}^{-2} \text{ s}^{-1}$. They have a mean Galactic latitude of 1.3° , a mean absolute Galactic longitude, ℓ , of 81.3° , and are concentrated at Galactic longitudes $60 \lesssim \ell \lesssim 90$. This may be due to clustering in nearby spiral arms. Of these 11, seven have exhibited giant outbursts as described in the previous section, and their Galactic locations are plotted in Figure 35. Of these seven, giant outbursts in A0355+26, 2S 1417–624, 4U 0115+63, 4U 1145–619, and GRO J2058+42 were identified by their

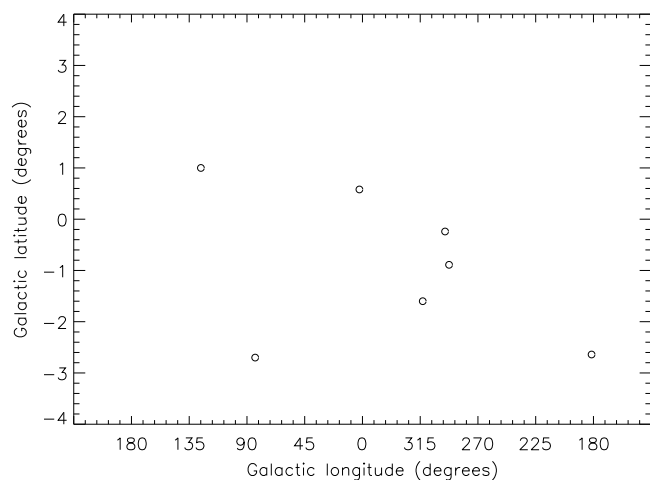


FIG. 35.—Galactic location of BATSE-detected giant outbursts from Be transients. The circles denote the location within the galaxy of those Be transients that were detected by BATSE during giant outbursts.

high pulsed flux and spin-up rate relative to other outbursts from these sources. The single outburst from GRO J1750–27 was identified as a giant from its peak spin-up rate ($\dot{\nu} \sim 4 \times 10^{-11} \text{ Hz s}^{-1}$), and the single outburst from A1118–616 from its duration (~ 50 days) and its large $\dot{\nu} \sim 2 \times 10^{-12} \text{ Hz s}^{-1}$ compared with the largest expected orbital signature (the orbit is unknown), although comparable rates are seen in normal outbursts of 2S 1417–624 and GS 0834–430. Using the distances inferred from the optical counterparts where they are available (see Nagase 1989), we find that the peak 20–50 keV pulsed luminosities of these outbursts are in the range of $(3\text{--}10) \times 10^{36} \text{ ergs s}^{-1}$. This implies that we can detect giant outbursts at distances of at least 11.5 kpc, roughly consistent with the giant outburst detection of GRO J1750–27, near the Galactic center.

Although these outbursts may not be standard candles, it is interesting to ask what sampling distance one would infer from their distribution in ℓ and b , shown in Figure 36, if they are standard candles. Given the limited data set, we take a simple model for the Galactic distribution. We assume that the Be transients are distributed as $\exp(-|z|/z_0)$ in the direction perpendicular to the plane and, like the matter in the Galaxy, fall off radially $\exp(-r/r_0)$ away from the Galactic center, where $r_0 = 3.5$ kpc (de Vaucouleurs & Pence 1978).

For a Galactic center distance of 8.5 kpc, we find that the acceptable fits ($\geq 90\%$ confidence) to the cumulative b distribution require a sampling distance in the range of $(35\text{--}50)z_0$ (see Fig. 36). If the Be binaries have the scale height $z_0 = 100$ pc of massive stars (Miller & Scalo 1979), then the sampling distance inferred from the latitude distribution is 3–5 kpc. This is consistent with the observed excess of objects in the direction of the Galactic center versus the anticenter, as the sampling distance is of order the exponential scale length in the disk population, r_0 . However, kick velocities of $v \sim 450 \pm 90 \text{ km s}^{-1}$ are typically imparted to neutron stars during the supernova (Lyne & Lorimer 1994), which potentially increases the scale height of those that remain in binaries up to ≈ 140 pc (Brandt & Podsiadlowski 1995). This helps to make the sampling distance more consistent with our first estimate but still a bit short. The resolution of this discrepancy may

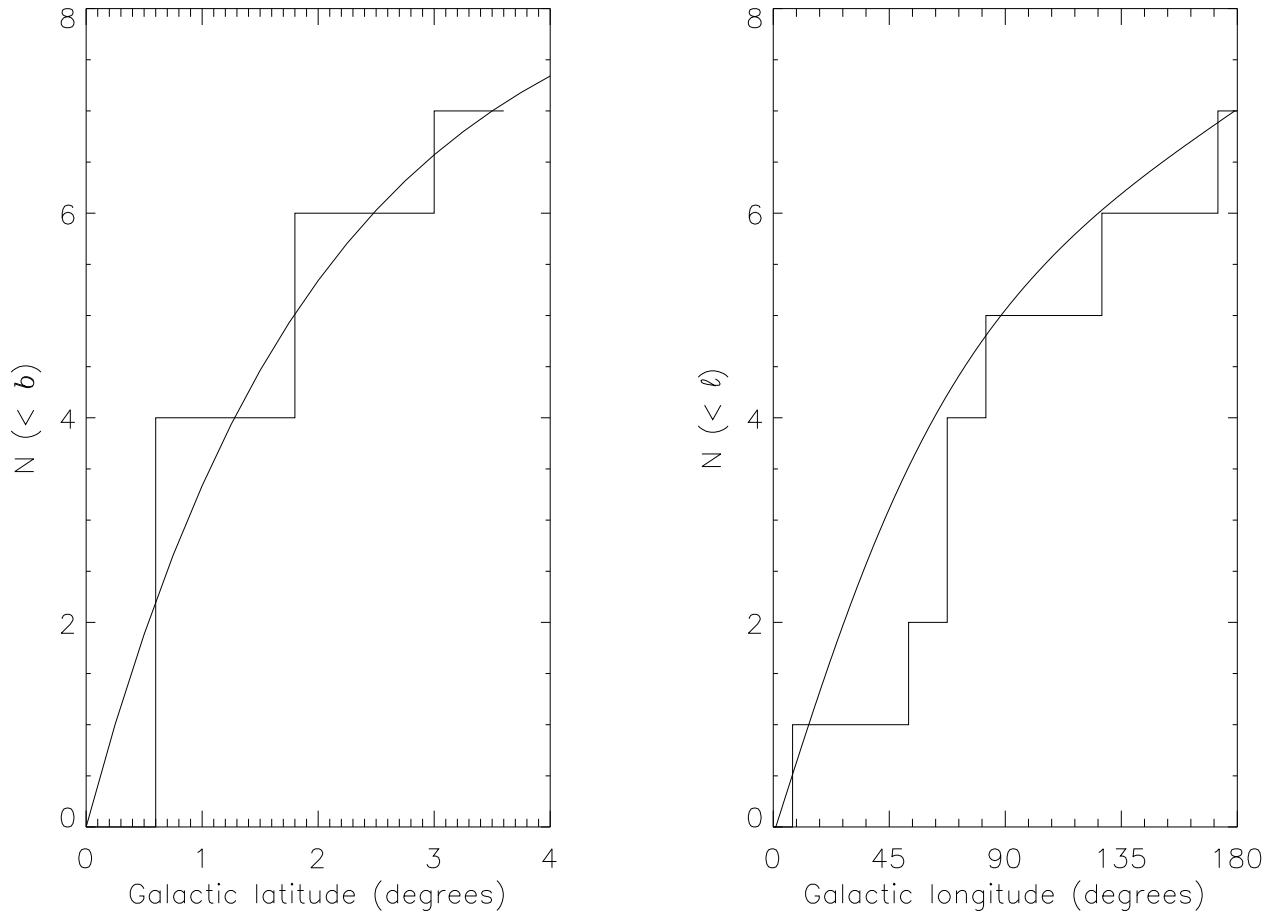


FIG. 36.—Cumulative b distribution (*left-hand panel*) and cumulative ℓ distribution (*right-hand panel*) of the seven Be-transient systems detected by BATSE during giant outbursts: A0535+262, A1118–61, GRO J1750–27, GRO J2058+42, 2S 1417–624, 4U 0115+634, and 4U 1145–619. The histogram and solid line respectively represent the actual data and the model prediction. Since our modeling has $\pm\ell$ and $\pm b$ symmetry, we use the absolute values of ℓ and b in this analysis. A sampling distance of $40z_0$, with $z_0 = 100$ pc gives the best fit to the b distribution and yields an acceptable Kolmogorov-Smirnov statistic. The relatively poor correspondence between the ℓ distribution and the model is due to the clustering of transients at $60^\circ \lesssim \ell \lesssim 90^\circ$.

be that the giant outbursts are not standard candles. We note also that our assumption of $\pm b$ symmetry is not strictly correct because the Sun is known to lie a vertical distance of $z_\odot \approx 15$ pc above the Galactic plane (Cohen 1995). Nevertheless, since z_\odot is small compared to both the sampling distance and the expected scale height of Be transients, including the effects of z_\odot will negatively shift the peak of the latitude distribution to $b \lesssim 0.2$, which does not affect our results, especially in light of other larger uncertainties.

BATSE detected eight giant outbursts from seven Be transients in 4 yr. The repetition by one of these sources enables us to estimate the recurrence timescale of giant outbursts. Define N_{loc} to be the total number of transients that exist within a distance R_{loc} of Earth, and assume that all the seven systems from which BATSE had detected giant outbursts are within distance R_{loc} of Earth. By modeling the frequency of giant outbursts as a Poisson process, we inferred that the most probable recurrence timescale of giant outbursts in each transient ≈ 12.5 yr, which implies that $N_{\text{loc}} \approx 25$. This allows us to compute the proportionality constant in the density distribution of Be transients that, when integrated over the Galactic disk, yields an estimate of the total number of Be transients in the Galaxy,

N_{tot} . As shown in Figure 36, $R_{\text{loc}} = 40z_0$ provides the best fit to the observed cumulative b distribution. For $z_0 = 100$ pc, $R_m = 4$ kpc, we obtain $N_{\text{tot}} \approx 1300$, while for $z_0 = 200$ pc, $R_m = 8$ kpc, we obtain $N_{\text{tot}} \approx 250$. If BATSE could indeed sample out to $R_{\text{loc}} = 11.5$ kpc, the estimated distance to GRO J1750–27, $N_{\text{tot}} \approx 130$ for $z_0 = 100$ pc. Since our estimate of the recurrence timescale hinges upon a single transient that exhibited more than one outburst, these estimates should be considered crude. However, they are consistent with estimates from evolutionary models of the total number of Be/neutron star binaries, $\sim 10^4$, most of which are quiescent (Meurs & van den Heuvel 1989).

5.7. Be/X-Ray Pulsar Orbits

BATSE has more than doubled the number of orbits that have been determined for Be/X-ray binaries, increasing the number from four to eight. See Table 3. We include in this classification GRO J1750–27, 2S 1553–54, and GS 0834–430, which we suspect have Be star companions. With this size sample, we can begin to make comparisons between the observed distribution of orbital elements and our expectations.

A main-sequence B star has a mass in the range of 4–16 M_\odot . The measured X-ray mass functions $f_X(M)$ for the Be/

X-ray pulsars should be consistent with masses in this range. If we assume a common neutron star mass of $1.4 M_{\odot}$, we can use the mass function, $f_x(M)$, to determine lower limits to the masses of the companions. If we further assume that the systems we see have randomly distributed orientations relative to our line of sight, we can use the distribution of mass functions to determine the distribution of companion masses. In Figure 37, we compare the cumulative mass-function distribution, $N[<f_x(M)]$ with the distribution we would get assuming a constant companion mass, M_c , a constant neutron star mass, $M_x = 1.4 M_{\odot}$, and random orientation. With the observed distribution is plotted the theoretical distributions for $4 M_{\odot}$, $6 M_{\odot}$, and $10 M_{\odot}$ companions. None of these curves can be said to fit the data; however, masses in the $6\text{--}12 M_{\odot}$ range are clearly called for. To explore the width of the companion mass distribution, a maximum likelihood fit was made to the observed mass functions, using a companion mass distribution that was uniform in log between two limiting masses. The best model had masses in the range of $6.7\text{--}13.1 M_{\odot}$; however, owing to the limited statistics, the distribution width was poorly constrained, with the 50% confidence region containing lower mass limits from 2 to $8 M_{\odot}$ and upper mass limits from 12.2 to $21 M_{\odot}$.

Be/X-ray binaries are thought to be the result of the evolution of a binary system of two B stars (van den Heuvel & Rappaport 1987). The progenitor of the neutron star is initially more massive. First, it transfers mass to its companion by Roche lobe overflow due to hydrogen-shell burning, which results in a helium star orbiting a rapidly rotating Be star. Then, the helium star transfers mass due to helium-shell burning. Finally, the helium star undergoes a supernova explosion. The velocity kick and the mass loss experienced in the supernova explosion can result in a wide eccentric orbit (or a disrupted system). Since the orbits are wide, orbital changes are slow compared to the evolutionary timescale of the Be star. The observed Be/X-ray system orbits are therefore fossils of supernovae in Be/helium binaries.

The widest resulting orbits (and those of longest period)

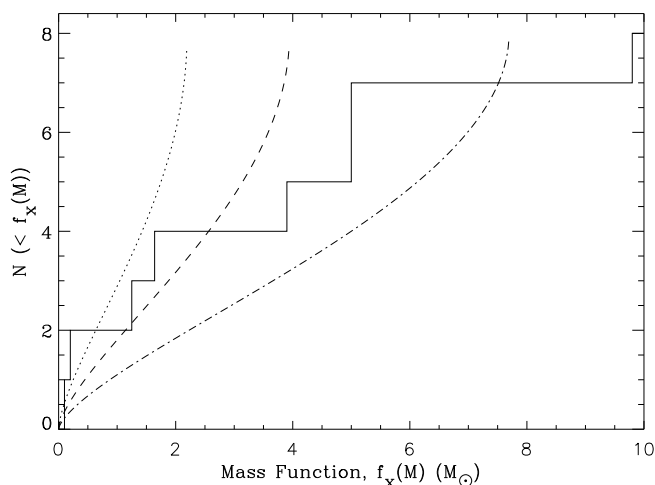


FIG. 37.—Cumulative distribution of the mass functions of the Be-transient pulsars. The measurements are given by the staircase curve. The remaining curves give the expected distribution for random orientation and a constant companion mass of $4 M_{\odot}$ (dotted line), $6 M_{\odot}$ (dashed line), and $10 M_{\odot}$ (dot-dashed line).

should be the most eccentric, and we therefore expect eccentricity to be correlated with orbital period. In Figure 38, we plot the orbital periods and eccentricities of the Be systems for which these have been determined. Only a weak correlation is present. The possible range of the orbital period P_{init} of the presupernova system, assuming an initial circular orbit and an asymmetric supernova explosion, is $P_{\text{orb}}(1 - e)^{3/2}\beta^{1/2} < P_{\text{init}} < P_{\text{orb}}(1 + e)^{3/2}\beta^{1/2}$, where β is the ratio of the current system mass to the presupernova system mass. This is shown in Figure 38 for each source, assuming $\beta = 0.9$. The initial period distribution could have been much narrower than the distribution of P_{orb} but must still have significant width. This may explain the weakness of the correlation.

The kick velocities are likely to be larger than the orbital velocities in the presupernova systems ($\approx 100 \text{ km s}^{-1}$). Lyne & Lorimer (1994) found from a study of radio pulsar proper motions a mean kick velocity of $450 \pm 90 \text{ km s}^{-1}$. The majority of systems are therefore disrupted. Kalogera (1996) gives analytic expressions for the distribution of orbital parameters of the undisrupted systems, assuming an initially circular orbit and a Gaussian kick velocity distribution. The form of the eccentricity distribution in the limit of large kick velocity relative to orbital velocity is found to be independent of all other parameters. In Figure 39, the cumulative distribution of the observed eccentricities is

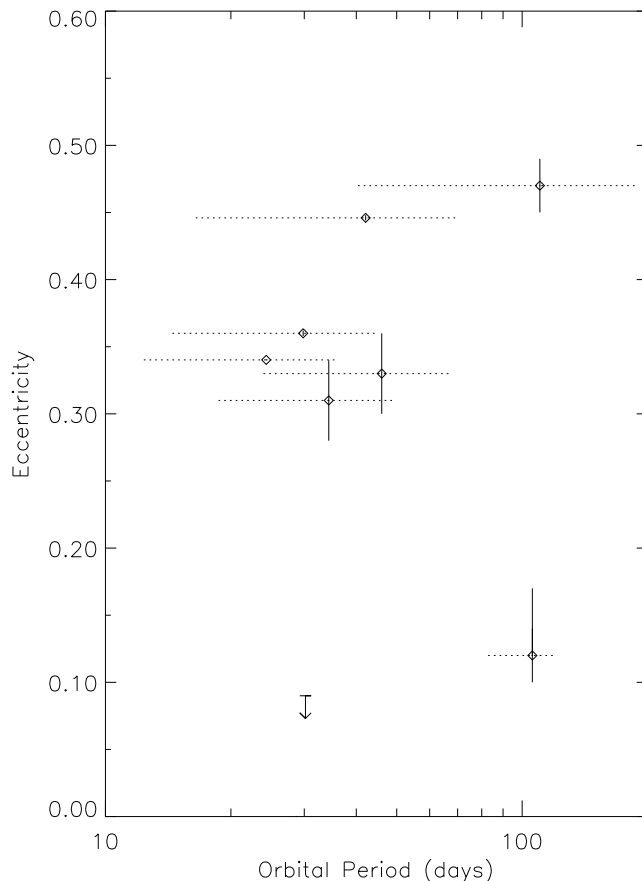


FIG. 38.—Eccentricities of Be/X-ray pulsars systems plotted against the orbital period. The dotted lines give the possible range of the orbital period for each system prior to the supernova that formed the neutron star, assuming an initially circular orbit and an asymmetric supernova explosion.

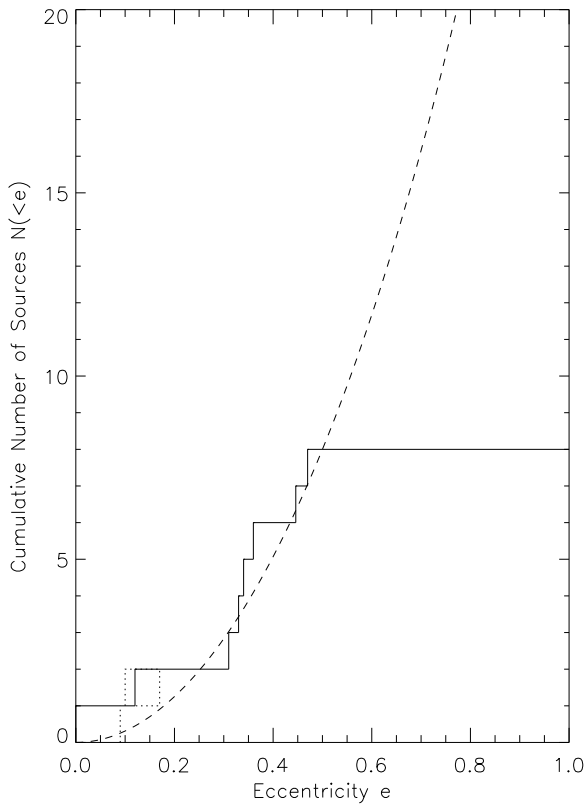


FIG. 39.—Cumulative distribution of Be/X-ray pulsar binary eccentricities. The observed distribution is given by the solid line. The predicted distribution, normalized for a total of eight sources with $e < 0.5$, is given by the dashed line (see text). The dotted lines give the eccentricity range allowed by the upper limit for the eccentricity of 2S 1553–54 and the errors on the eccentricity of GS 0834–430.

compared to the predicted cumulative distribution, which has been normalized to a mean of eight sources with $e < 0.5$.

The observations and predicted distribution agree reasonably for $e < 0.5$ but poorly above this value. No sources with $e > 0.5$ are observed, but 30 are expected. We think it unlikely that this is due to an error in our assumptions about the kick distribution. More likely this is evidence for strong selection effects against high eccentricities. High-eccentricity orbits will typically undergo outbursts only near periastron and may be observed only in isolated outbursts, which makes orbit determination difficult or impossible. If this is the explanation, then nearly all of the Be/X-ray pulsar for which no orbit has been determined (20 sources) must have high eccentricity ($e > 0.5$). It is also interesting to note that the eccentricities are high in PSR B1259–63 ($e = 0.8698$; Johnston et al. 1992) and PSR J0045–7319 ($e = 0.8080$; Kaspi et al. 1994), the two known Be/radio pulsar binaries.

6. SUMMARY

We have presented 5 years of continuous pulse timing and flux observations of accreting binary pulsars with the BATSE instrument on *CGRO*. This is the most detailed and complete history of spin frequency behavior and outburst activity in accreting pulsars to date and presents a qualitatively different picture of accreting binary pulsars than understood from the sparse histories previously available. Frequencies and fluxes presented in this paper, along with

daily folded pulse profiles, are being made available through the *Compton Observatory* Science Support Center.

The standard picture of accreting pulsars was developed over 20 years ago and has been largely accepted and applied to other systems containing accreting magnetic stars. The BATSE data allow us to test these theories critically, and in many cases the observed behavior is unexpected and difficult to explain. The accretion torque behavior seen in persistent disk-fed systems was particularly surprising. The slow, long-term spin-up trend in Cen X-3, long considered an example of a pulsar near equilibrium (§ 5.1; Fig. 31, *upper panel*), is, in fact, the result of alternating 10–100 day intervals of steady spin-up and spin-down (§ 5.1; Fig. 31, *lower panel*; § 4.2; Fig. 12). The torque displays rapid transitions between spin-up and spin-down with a magnitude ~ 5 times larger than the long-term spin-up torque (§ 5.1; Fig. 32). This switching behavior is also seen in OAO 1657–415 (Fig. 13) and in the long-term behavior of 4U 1626–67 and GX 1+4 (Fig. 6). We propose that this behavior is common in disk-fed pulsars (§ 5.1).

Observing the predicted correlation between spin-up rate and bolometric luminosity, $\dot{\nu} \propto L^{6/7}$, has long been considered a critical test of accretion torque theory (§ 3). We have observed $\dot{\nu}$ and 20–50 keV pulsed flux, F_{pulsed} , in outbursts of two transients, A0535+26 (Fig. 26) and GRO J1744–28 (Fig. 11). We find $\dot{\nu} \propto F_{\text{pulsed}}^\gamma$ with $\gamma = 0.951(26)$ for A0535+26 and $\gamma = 0.957(26)$ for GRO J1744–28 (Fig. 33; § 5.2). *EXOSAT* observations of EXO 2030+375, using the orbit measured with BATSE, yielded $\gamma \simeq 1.2$ (Reynolds et al. 1996). This disagrees with the predicted scaling of magnetospheric radius with mass accretion rate, $r_m \propto \dot{M}^{-2/7}$. However, the apparent contradiction may be that F_{pulsed} is not a good indicator of bolometric luminosity or \dot{M} . In fact, an indirect test of the r_m - \dot{M} relation is provided by the observed correlation between the frequency of quasi-periodic oscillations seen with BATSE in A0535+26 and $\dot{\nu}$ and is consistent with the predicted scaling (§ 5.2; Finger et al. 1996c).

Power density spectra of torque fluctuations in the eight persistently bright pulsars monitored with BATSE (Fig. 34) show that pulsars known to be wind-fed (Vela X-1, GX 301–2, and 4U 1538–52) are flat. Their spin-frequency behavior can be described as a random sequence of independent torque fluctuations. In contrast, the disk-fed pulsar Cen X-3 has an approximately $1/f$ power spectrum of torque fluctuations, as do GX 1+4 and OAO 1657–415, which indicates the presence of correlations between accretion torques on long timescales (§ 5.4). It is unclear if such correlations are a signature of disk accretion however, as both 4U 1626–67 and Her X-1 show flat power spectra, and the accretion mechanism in GX 1+4 and OAO 1657–415 is unknown. Furthermore, two dramatic spin-up episodes in GX 301–2 of ~ 20 days duration (Fig. 16) suggest that transient accretion disks sometimes form in primarily wind-fed pulsars (§ 5.3). The $1/f$ power spectrum of Cen X-3 is in conflict with previous measurements and calls for a reexamination of the relation of noise strength with luminosity and spin-up rate observed prior to BATSE.

Most of the Be-transient pulsars observed with BATSE show a sequence of “normal” outbursts spaced at the orbital period (Fig. 17; § 4.3). Also observed are occasional “giant” outbursts, characterized by high spin-up rates, strongly correlated with flux and of longer duration (e.g., Figs. 26, 22, and 28), which suggests accretion from a tran-

sient disk (§ 5.5). The repeating normal outbursts might be explained by the large tidal torques experienced by the disk during periastron passage (§ 5.5).

We have estimated the total number of Be/X-ray transients in the Galaxy and find there are ~ 100 – 1000 such systems, depending upon their assumed Galactic scale height and the BATSE sampling radius (§ 5.6). BATSE observations have doubled the number of measured Be/X-ray pulsar binary orbits, from four to eight (Table 3). The distribution of orbital eccentricities (Fig. 39) agrees well with predictions from radio pulsar proper motions for $e < 0.5$ and suggests that nearly all of the Be/X-ray pulsars for which no orbit has been determined must have high eccentricity (§ 5.7).

There are several important topics, not touched upon here, which will eventually benefit from BATSE observations. These include the time evolution of orbital param-

eters (e.g., orbital decay and apsidal motion), a more complete analysis of the population of Be transients, and searches for rapidly rotating pulsars from analysis of higher time resolution data.

We acknowledge John Grunsfeld for important contributions to the early stage of this project and Ed Brown for helpful comments and for carefully proofreading the manuscript. We also thank the referee, Saul Rappaport, for a careful review of our manuscript. This work was funded in part by NASA grants NAG 5-1458, NAG 5-3293, and NAGW-4517. D. C. was supported at Caltech by a NASA GSRP Graduate Fellowship under grant NGT-51184. The NASA Compton Postdoctoral Fellowship program supported D. C. (NAG 5-3109), L. B. (NAG 5-2666), and R. W. N. (NAG 5-3119). L. B. was also supported by Caltech's Lee A. DuBridge Fellowship, funded by the Weingart Foundation, and by the Alfred P. Sloan Foundation.

APPENDIX A

PULSED OBSERVATIONS WITH BATSE

The *Compton Gamma-Ray Observatory* (*CGRO*) was launched on 1991 April 5 into a 400 km orbit inclined $28^{\circ}5$ with respect to Earth's equator that precesses about Earth's polar axis with a period of ≈ 53 days. BATSE consists of eight identical uncollimated detector modules arranged on the corners of the *CGRO* spacecraft (Fishman et al. 1989; Horack 1991). Each detector module contains a large-area detector (LAD) and a smaller spectroscopy detector. Our pulsar studies deal entirely with data from the LADs, each of which contains a NaI(Tl) scintillation crystal 1.27 cm thick and 50.8 cm in diameter, viewed in a light collection housing by three 12.7 cm diameter photomultiplier tubes. The LADs are shielded in front by a 1 mm aluminum window and a plastic scintillator for charged particle detection and have an effective energy range of 20 keV–1.8 MeV and an energy resolution of about 35% at 100 keV. Below 30 keV, the sensitivity is severely attenuated by the aluminum and plastic shielding.

Scintillation pulses from the LADs are processed in two parallel paths: a fast, four-channel discriminator circuit and a slower, multichannel pulse-height analyzer. Energy calibration is maintained during flight by an automatic correction scheme that adjusts the detector gain so as to keep the 511 keV line from the gamma-ray background in the same channel. There are many different BATSE data products available. The three that we use for pulsar investigations are as follows:

DISCLA data.—Count rate samples for each detector from the discriminator circuit in four energy channels at a time resolution of 1.024 s.

CONT data.—Count rate samples for each detector from the pulse-height analyzer in 16 energy channels at a time resolution of 2.048 s.

PSR data.—Count rate samples for a programmable combination of detectors folded into 64 phase bins with a programmable folding period in 16 energy channels and a programmable collection time, typically 8–16 s.

The CONT and DISCLA data types are available continuously and are used for slowly rotating pulsars. We use the PSR data for pulsars with spin periods less than or comparable to the DISCLA and CONT sampling rates (e.g., Her X-1 and GRO J1744–28). Approximate energy channel boundaries for the DISCLA and CONT data and the typical count rates (for background-dominated observations) are given in Table 6. Figure 40 shows the variation of the energy channel boundaries over the various LADs for CONT channels 0–7.

Most of our accreting pulsar studies are carried out below 100 keV, so we principally use DISCLA channel 1 (20–60 keV) and CONT channels 1–6 (25–125 keV). Pendleton et al. (1995) have determined the response of the LADs to monochromatic photons of various energies. The effective area at normal incidence for full energy deposition peaks near 1500 cm^2 around 100 keV. The effective area drops below 100 keV owing to the absorption of low-energy photons in the aluminum window and the charged-particle detector and above 100 keV owing to the increased transparency of the LAD detector. Each of the LADs has slightly different energy channels (see Fig. 40) which we take into account when constructing the response matrices.

Prior to scientific analysis, the BATSE data undergo four stages of processing. Each step except the first must be performed separately for each source.

1. *Background subtraction.*—The detector background is removed using a phenomenological model. In addition, quality flags are applied at this stage, and spikes removed.

2. *Detector weighting.*—Detectors with significant projected area to the source are weighted and summed to optimize the signal-to-noise ratio for timing analysis.

3. *Barycenter correction.*—Photon arrival times are corrected for spacecraft orbital motion to barycentric dynamical time (TDB) using the Jet Propulsion Laboratory DE-200 solar-system ephemeris (Standish et al. 1992). The orbit of the pulsar is also removed for systems where it is known.

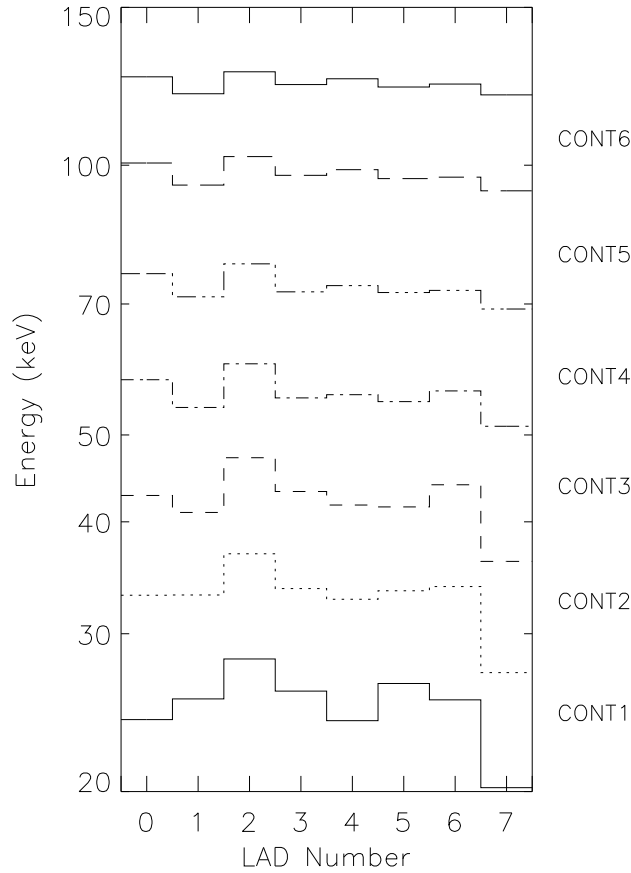


FIG. 40.—The energies of the Large Area Detector (LAD) channel boundaries for the CONT data. We display the lower and upper boundaries of CONT channels 1–6 for all detectors. The gain is stabilized on board using the 511 keV background feature. These bin energies apply to two different intervals, MJD 48,406.11–49400.69 and MJD 49,419.69 – 50062.82, which together comprise most of the *CGRO* mission.

TABLE 6
ENERGY CHANNELS IN BATSE DISCLA AND CONT DATA

Channel	Energy Range (keV)	Background Rate (counts s ⁻¹)
DISCLA 1.....	20–60	1500
DISCLA 2.....	60–110	1200
DISCLA 3.....	110–320	1000
DISCLA 4.....	> 320	700
CONT 0.....	20–24	250
CONT 1.....	24–33	450
CONT 2.....	33–42	500
CONT 3.....	42–55	500
CONT 4.....	55–74	500
CONT 5.....	74–99	450
CONT 6.....	99–124	300
CONT 7.....	124–165	300
CONT 8.....	165–232	300
CONT 9.....	232–318	200
CONT 10.....	318–426	130
CONT 11.....	426–590	130
CONT 12.....	590–745	50
CONT 13.....	745–1103	80
CONT 14.....	1103–1828	80
CONT 15.....	> 1828	200

NOTE.—These channel boundaries are *approximate* and are averaged over the eight detectors. Each detector has slightly different edges, as shown in Fig. 40. The CONT edges are programmable; the displayed values are typical, and are computed using the calibration discussed in Preece et al. 1997. We have made use of CONT data through channel 7 in our analyses.

4. *Earth occultation windowing.*—Intervals where the source is occulted by the Earth are removed. Steps 1 and 2 are particular to the BATSE data, so we describe them in detail here.

Background subtraction is not performed on PSR data, and the selected detectors are uniformly weighted. Barycentric corrections are applied once per collection (8–16 s) using the midpoint time, with the times of phase bin edges computed relative to the midpoint time.

A1. BACKGROUND SUBTRACTION

Because the LADs are uncollimated and nonimaging, the background count rate includes contributions from the diffuse Galactic and cosmic background, atmospheric gamma rays, a prompt local background caused by interactions of primary cosmic rays with detector materials, activation of radionuclides in the detectors by particles during passages through the South Atlantic magnetic anomaly (SAA) that results in a delayed internal background, and discrete source contributions. A detailed review of the gamma-ray background for low-Earth orbit instruments in general is given by Dean, Lei, & Knight (1991), while a discussion of the background for BATSE in particular is given by Rubin et al. (1996).

The diffuse cosmic gamma-ray background is the strongest component below 300 keV. It is isotropic and varies for each detector depending on the fraction of the field of view that is occulted by Earth. The atmospheric and prompt backgrounds depend upon the position of the spacecraft in Earth's magnetic field and vary with the local geomagnetic cutoff rigidity. Primary cosmic-ray protons below the local cutoff energy do not penetrate Earth's field at a given geomagnetic latitude. Bombardment by cosmic rays and trapped protons in the SAA produce radionuclides that decay with various lifetimes, notably ^{128}I ($\tau_{1/2} = 25$ minutes), which creates a delayed internal background. Sharp changes in the count rate also occur when bright, discrete sources cross the limb of Earth. In addition, there are data gaps that occur because of brief telemetry outages or errors and from turning off the detector high voltage during SAA passages.

These background variations introduce power at a wide range of Fourier frequencies and reduce the sensitivity to pulsed signals relative to the Poisson counting limit. Strong quasi-sinusoidal variations with ≈ 93 minute period are mainly due to orbital modulation of sky area visible to the detectors. In addition, the spikes (mainly due to charged particle-induced phosphorescence in the NaI) and gaps in the data introduce variability at all analysis frequencies and are one of the major sources of noise power. Data quality flags set by the BATSE operation team are initially used to reject data containing gamma-ray bursts, phosphorescence events, and other rapid background variations. Additional quality control that identifies spikes and gaps is a crucial step in our analysis of BATSE data. Three separate background subtraction techniques have been developed, each of which involves modeling the background variations.

The most sophisticated technique is the use of a phenomenological model that includes each of the known contributions (Rubin et al. 1996). The atmospheric and prompt components of the background depend upon the geomagnetic rigidity. The cosmic, atmospheric, and prompt components all vary with the direction of the detector relative to Earth. The delayed component can be modeled as an exponential decay following each SAA passage. Finally, discrete sources contribute a component that we approximate as the product of the effective area to the source and a step function that is zero when the source is occulted by Earth and unity when it is not. The resulting explicit form of the function used to fit the background independently for each LAD is

$$M(t_i) = \sum_{j=0}^3 (a_j + b_j L) P_j(\cos \theta_i) + f_k \exp \left[\frac{-(t_i - t_{\text{SAA}})}{\tau_k} \right] + \sum_{l=1}^{n_{\text{occ}}} g_l T_{li}, \quad (\text{A1})$$

where i labels the time bin corresponding to t_i , L is the McIlwain L -shell parameter (a measure of the location in Earth's magnetosphere; see, e.g., Rossi & Olbert 1970), P_j is the Legendre polynomial of order j , t_{SAA} is the end time of the most recent SAA passage, τ_k is the decay time of ^{128}I , and T_{li} is the atmospheric transmission function of source l at the mean energy of bin i . The coefficients a_j , b_j , f_k , and g_l are determined by a linear least-squares fit to the raw data. We obtain acceptable fits for segments of length 0.125 day and then subtract the best-fit model from the raw data. This technique assumes the presence of periodic behavior at harmonics of the orbital period, so some attenuation of low-frequency signals is inevitable in the fitting process.

Figure 41 shows the power spectrum of the CONT channel 1 data before and after this background subtraction. Following background subtraction, the noise power is consistent with the Poisson level on timescales $\lesssim 80$ s. This background model performs somewhat better than the other techniques at longer timescales and allows us to probe deeper at lower pulse frequencies than would otherwise be possible. Histories of OAO 1657–415, Vela X-1, 4U 1538–52, GX 301–2, GS 0834–430, GRO J1948+32, EXO 2030+375, 4U 1145–619, and GRO J1008–57 in § 4 were constructed using this background subtraction technique, as were data sets at the COSSC.

A model that is more ad hoc for the background can be produced by applying a simple frequency-domain digital filter to the data (Chakrabarty et al. 1993; Chakrabarty 1996). To construct the background model, we first remove impulsive spikes and interpolate over gaps in the raw data and then perform smoothing in the frequency domain by multiplying the Fourier transform of the interpolated time series by a low-pass filter defined as $R(\nu < \nu_0) = [1 + \cos(\pi\nu/\nu_0)]/2$ for $\nu < \nu_0$ and $R(\nu > \nu_0) = 0$ for $\nu > \nu_0$, with $\nu_0 = 1.6 \times 10^{-3}$ Hz. The inverse transform of this product is a good approximation to the orbital background variation, which is then subtracted from the raw data after reintroducing the original gap structure. Histories of 4U 1626–67 and GX 1+4 in § 4 were constructed using this background subtraction technique.

Finally, an empirical background model is often used in analysis of the DISCLA data. This is a spline function with quadratics in time, in segments normally of 300 s length, connected with continuity in value and slope at segment boundaries within contiguous sets of data. This model is fitted simultaneously with a Fourier representation of the pulsed signal, described further in Appendix B, § B1.2. Histories of GRO J1744–28, Cen X-3, 4U 0115+63, 2S 1417–624, A0535+26, 4U 1145–619, and A1118–616 in § 4 were constructed using this technique.

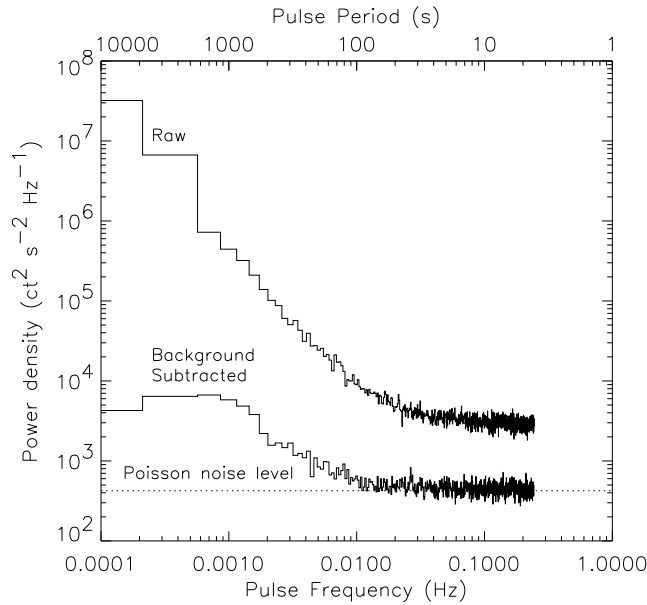


FIG. 41.—Typical power spectrum of the BATSE LAD background in the 25–33 keV range. The data shown are for CONT Channel 1 (25–33 keV) from LAD 2 on MJD 48,851–48,852 when the mean count rate was $423.7 \text{ counts s}^{-1}$. The top curve is the unprocessed raw data, while the bottom curve is after background subtraction.

A2. OPTIMAL COMBINATION OF DETECTORS

The octahedral arrangement of the BATSE detector planes makes a pulsar visible to four BATSE detectors during any given spacecraft pointing (which typically changes every 2 weeks). The sensitivity to a given pulsar then depends on the angular response of the detectors. A discussion of techniques for extracting signals from multiple BATSE detectors appears in Chakrabarty (1996). We summarize that discussion here and then present an optimal scheme for weighting detectors when the energy spectrum of the source is known.

The dominant effect is the projected detector area along the line of sight to the source, which varies as $\cos \theta$ (where θ is the viewing angle between the detector normal and the source). The response to 100 keV photons is approximately $\cos \theta$ but diverges from this for energies both above and below 100 keV for different reasons. At higher energies, the photon attenuation length in NaI becomes comparable to the thickness of the crystal, so that not all incident photons are captured. Hence, the decrease in projected geometric area with increasing θ is partially offset by the increase in path length through the detector, both of which have a $\cos \theta$ dependence. This results in a relatively flat angular response for $\theta \gtrsim 50^\circ$ at high energies. At low energies, the attenuation length in NaI is very short, which makes the detector thickness irrelevant. However, the path length through the shielding in this case increases with θ , and the resulting attenuation, $\exp[-\tau(E)/\cos \theta]$, where $\tau(E)$ is the optical thickness of the shield at energy E , of flux incident on the LAD causes the response to fall more steeply than $\cos \theta$.

A consequence of the variation of angular response with energy is that the response to a pulsar depends upon its energy spectrum. Typical accreting pulsar spectra can be represented as $dN/dE \propto E^{-\alpha}$, where $2 < \alpha < 5$ in the 20–100 keV range. Figure 42 shows the angular response to a 20–75 keV photon power-law spectrum for $\alpha = 2$ and $\alpha = 5$. For comparison, $\cos \theta$

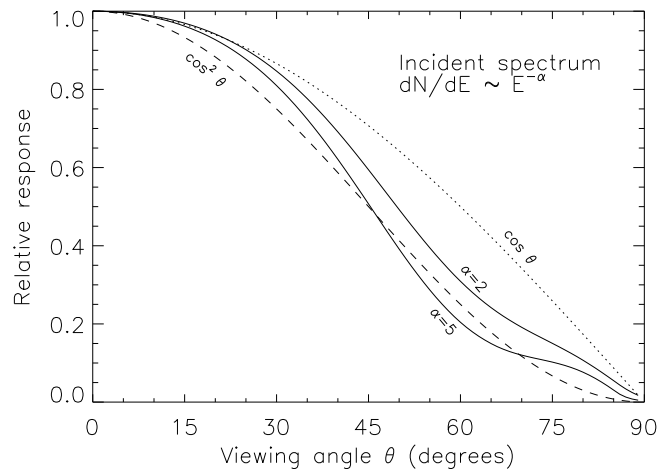


FIG. 42.—The 20–75 keV BATSE LAD angular response to an incident photon power-law spectrum $dN/dE \propto E^{-\alpha}$, for $\alpha = 2$ and $\alpha = 5$. For comparison, $\cos \theta$ response (dotted line) and $\cos^2 \theta$ response (dashed line) are also shown.

and $\cos^2 \theta$ are also plotted. The response falls off more quickly than $\cos \theta$ since the large number of low-energy photons dominate despite the attenuation by the shield. As expected, this effect is more pronounced for the steeper power-law index, where the proportion of incident lower energy photons is even higher. In general, the integrated response varies $\approx \cos \theta$ for small angles ($\theta \lesssim 25^\circ$), independent of photon index. At larger angles, $\cos^2 \theta$ is a more conservative general assumption when the source spectrum is unknown.

Our timing analysis uses a weighted sum of the count rates from the four detectors exposed to the source. If we consider a background-limited observation and make the approximation that the background rate is the same in all detectors, is isotropic, and is governed by Poisson statistics, then the resulting signal-to-noise ratio (SNR) is

$$\text{SNR} = \frac{C_S T \sum w_i(\theta_i) r_i(\theta_i)}{\sqrt{C_B T \sum w_i^2(\theta_i)}}, \quad (\text{A2})$$

where C_S is the source count rate in a single detector at normal incidence, C_B is the background count rate in each detector, T is the exposure time, θ_i is the source viewing angle for the i th detector, $r_i(\theta_i)$ is the angular response function of the i th detector, and $w_i(\theta_i)$ is the detector weighting function that we are optimizing.

BATSE is more sensitive to some areas of the sky than others. The highest sensitivity at low energies is at the eight points in the sky that lie on the BATSE detector normals (i.e., the direction vector for normal incidence), while the lowest sensitivity is at the six points in the sky that lie equidistant from the eight detector normals. The weighting function for summing detectors that maximizes the signal-to-noise ratio as parameterized in equation (A2) depends upon where in the sky the source is relative to the detector normals. Because the angular response, $r(\theta)$, depends upon the intrinsic energy spectrum of the source and is different for each detector, determining the optimal weighting coefficients requires the full response matrix of each exposed detector and an assumed incident energy spectrum. For DISCLA data, where we utilize a single energy channel, we use an optimal detector weighting given by

$$w_i = r_i(E_f) \left[\sum_j r_j^2(E_f) \right]^{-1}. \quad (\text{A3})$$

Here $r_i(E_f)$ is the predicted count rate in DISCLA channel 1 for detector i assuming that the source has a photon spectrum $F(E) = (A/E) \exp(-E/E_f)$. This weighting scheme takes into account differences between detectors (see Fig. 40), unlike the weighting scheme described below, which assumes identical detectors and $\cos^2 \theta$ response. The e -folding energies E_f were selected based on published spectra.

We also use a weighting scheme that is independent of the source spectrum by approximating the angular response function as $r(\theta) = \cos^2 \theta$ and calculating sensitivity as a function of sky position for weighting functions of the form $w(\theta) = \cos^n \theta$, with $n = 0, 1, 2, 3, 4$. The best overall sensitivity is achieved by choosing the detector weighting adaptively [i.e., selecting whichever cosine power law optimizes sensitivity for a given source location with respect to the detectors, rather than using a single form of $w(\theta)$ for all source locations]. However, $w(\theta) = \cos^2 \theta$ weighting provides both reasonable average sensitivity and spatial uniformity, is $\sim 15\%$ more sensitive on average than an unweighted sum of exposed detectors and is at worst $\sim 5\%$ poorer than adaptive weighting. We use $w(\theta) = \cos^2 \theta$ weighting for most frequency measurements with CONT data.

APPENDIX B

BATSE DATA ANALYSIS

In this Appendix we discuss how frequency and flux are computed following the preprocessing described in Appendix A. Frequency estimation is covered first, followed by pulsed flux.

B1. FREQUENCY ESTIMATION

B1.1. Frequency Estimation using Power Spectra

Power spectra were used to compute the frequency histories of 4U 1626–67, GX 1+4, OAO 1657–415, GX 301–2, GS 0834–430, GRO J1948+32, EXO 2030+375, and GRO J1008–52 displayed in § 4, as well as in data files at the COSSC. Power spectra are computed using the fast Fourier transform (FFT). Given a contiguous data set of duration T seconds in N uniform bins of duration T/N , the FFT returns $N/2 + 1$ statistically independent estimates, a_j , of the amplitude and phase of the variability at frequencies $\nu_j = j/T$, where $0 \leq j \leq N/2$. The normalized power at ν_j is $P_j \equiv |a_j|^2 / \bar{P}(\nu_j)$, where $\bar{P}(\nu)$ is the average power, $\langle |a_j|^2 \rangle$, in the vicinity of ν_j (excluding frequencies immediately adjacent to ν_j). This normalization is important because the background power is strongly frequency dependent (see Fig. 41). Thus defined, $\langle P_j \rangle = 1$. Data collected by BATSE are in uniform bins of duration 2.048 s (CONT data), 1.024 s (DISCLA data), or shorter (PSR data). However, corrections of spacecraft times to the solar system barycenter causes the bins to become nonuniform. We therefore define a new array with bins equispaced in arrival time at the solar system barycenter (or in the frame of the neutron star if the orbit is known). An individual time series bin from the spacecraft will generally overlap two such bins. We can either treat each bin as a delta function at the bin center and add all counts to the appropriate bin in the new array (*whole binning*) or split counts

between overlapping bins in proportion to the degree of overlap (*bin splitting*). We choose bin splitting because it performs significantly better than whole binning when $\nu \gtrsim N/2T$ while introducing negligible corrections to the power spectrum.

The response, $R^2(\nu)$, of the power spectrum to a sinusoid of frequency ν decreases with increasing frequency and also depends upon the separation, $\Delta\nu$, between ν and the nearest Fourier frequency, falling off as

$$R^2(\nu) = \text{sinc}^2(\pi\nu/2\nu_{\text{Nyq}}) \text{sinc}^2(\pi\Delta\nu T) \quad (\text{B1})$$

where $\text{sinc}(x) = \sin(x)/x$ and $\nu_{\text{Nyq}} = N/2T$ is the Nyquist frequency. Attenuation at high frequency is intrinsic to binned data and constrains us to use DISCLA and/or PSR data for fast pulsars, but attenuation with $\Delta\nu$ can be circumvented by computing the power at a denser set of frequencies. By appending an array of zeros of length $(m-1)N$ to the array of data and computing the FFT, we obtain an overresolved Fourier transform with m times finer frequency spacing, but with frequency bins that are no longer statistically independent. The signature of a sinusoid is no longer in one or two bins but is distributed over $\sim m$ bins. To preserve the definition $\nu_j = j/T$, we allow j to take on $m(N/2) + 1$ values in increments of $\epsilon \equiv 1/m$. If the highest power occurs in frequency bin j , then Middleditch (1976) has shown that the best estimate of the signal frequency is given by

$$\nu = \nu_j + \frac{3}{4\pi^2\epsilon T} \left(\frac{P_{j+\epsilon} - P_{j-\epsilon}}{\bar{P}_j} \right). \quad (\text{B2})$$

The uncertainty in the frequency (Middleditch 1976; Middleditch & Nelson 1976) is given by

$$\sigma_\nu \simeq \frac{1}{2\pi T} \sqrt{\frac{6}{P_j}}. \quad (\text{B3})$$

In all cases we use the dominant harmonic for frequency estimation. For double-peaked pulsars (see Fig. 7), the second harmonic usually dominates.

It is worth noting that $\sigma_\nu \propto T^{-3/2}$ (since $P \propto T$), and hence N_d -day power spectra are $N_d^{3/2}$ times more precise than 1 day estimates. However, transform length cannot be increased indefinitely because variations in ν will eventually cause a loss of coherence when $T^2 \geq \langle |\dot{\nu}| \rangle$. We call this the *decoherence timescale* (see Appendix A of Chakrabarty et al. 1997a).

The frequency histories in this paper for OAO 1657–415, GS 0834–430, GRO J1948+32, EXO 2030+375, and GRO J1008–52 were made from daily power spectra of CONT data. These histories and others made from daily power spectra are available in the data sets at the COSSC. For the sources 4U 1626–67, GX 1+4, and GX 301–2, multiday power spectra were used.

B1.2. Frequency Estimation using Epoch Folding

Spin frequencies were also estimated by epoch-folding data at a range of trial frequencies. We use the term “epoch folding” to describe any technique in which a pulse phase is assigned to each time bin based upon a model of the spin frequency. In some cases, we implement epoch folding as a fitting procedure. This technique was used with DISCLA data for the histories of Cen X-3, 4U 1538–52, 4U 0115+634, GRO J1750–27, 2S 1417–624, GRO J2058+42, 4U 1145–619, and A1118–616 shown in § 4. Detection and determination of the pulse frequency are based on the Z_m^2 test (Buccheri et al. 1983), which measures the significance of the first m Fourier amplitudes of the epoch-folded pulse profile.

Rather than rebinning the data into uniform phase bins and then folding them, we fit the data using a background model and a low-order Fourier expansion in the pulse phase model. Fitting does not require rebinning and hence avoids the loss of phase resolution inherent to rebinning techniques, which is important when the low time resolution is $\gtrsim P_{\text{spin}}$ (Deeter & Boynton 1986). The data are divided into intervals of about 1 to 10 days, and each interval is fitted with a model $C(t)$ of the form

$$C(t) = M(t) + \sum_{k=1}^n [A_k \cos 2\pi k\phi(t) + B_k \sin 2\pi k\phi(t)], \quad (\text{B4})$$

where $M(t)$ is a model of the background rate, the harmonic sum is a Fourier representation of the pulse profile, and $\phi(t)$ is the pulse phase, where we generally assume a constant frequency for each interval and use $n = 3$. The background is modeled as a quadratic spline, with segments every 300 s and with value and slope continuous across segment boundaries (but not across gaps). This background modeling procedure is approximately equivalent to applying a high-pass filter with ν^6 roll-off and a roll-off frequency of ~ 0.002 Hz (500 s). The Z_3^2 statistic is determined for each trial frequency for the best set of fit parameters, $\{A_k, B_k\}$, and values of Z_3^2 near the peak value fit to determine the frequency. In the case of 4U 1538–52, because of its low frequency, we use the phenomenological background model described in Appendix A, § A1, rather than a quadratic spline.

B1.3. Frequency Estimation from Fits to Pulse-Phase Measurements

The frequencies histories of GRO J1744–28, Her X-1, Vela X-1, GRO J1750–27, and A0535+26 shown in § 4 were determined from fits to pulse phase measurements. Phases were determined (for orbital analyses) by epoch-folding data over short intervals (~ 0.5 days) and correlating the resulting pulse profiles with pulse templates to determine phase offsets from the epoch-folding phase model. The total phases were then divided into intervals of several days and a linear fit in emission time made to the total phases (model plus offset) in each interval to obtain frequencies.

B2. PULSED FLUX ESTIMATION

B2.1. *What Is Pulsed Flux and Pulsed Fraction?*

Pulsed flux is the periodically varying part of the flux from a source. Unlike average flux, pulsed flux is not uniquely defined, and we employ two separate definitions for different purposes and for different sources. Let $F(\phi)$ be the flux of a pulse profile at phase ϕ , $0 \leq \phi \leq 1$, let $\bar{F} = \int_0^1 F(\phi) d\phi$ be the average flux, and let $F_{\min} = \min [F(\phi)]$ be the minimum flux. We define peak-to-peak pulsed flux as $F_{\text{pulsed}} = \int_0^1 [F(\phi) - F_{\min}] d\phi$, and root mean square (rms) flux as $F_{\text{RMS}} = \left\{ \int_0^1 [F(\phi) - \bar{F}]^2 d\phi \right\}^{1/2}$. Their relative values depend upon pulse shape. For a square wave, they are equal. For a sinusoid, which is a good approximation to most accreting pulsars, $F_{\text{pulsed}} = (2)^{1/2} F_{\text{RMS}}$. Peak-to-peak pulsed flux has intuitive appeal, but it is more difficult to measure since F_{\min} is harder to determine than \bar{F} . We generally use peak-to-peak pulsed flux for average spectra of many days (see Table 4), where S/N is large, and rms flux for daily estimates, as displayed in § 4. *Pulsed fraction* is the ratio of the pulsed flux to the mean flux (pulsed + unpulsed). It is in general energy dependent.

B2.2. *Peak-to-Peak Pulsed Spectra and Flux*

Average energy spectrum and flux using CONT data.—To estimate the energy spectrum of the pulsed emission, we first compute the pulsed count rate in each energy channel by epoch-folding ~ 1 day of data at a time into $N \lesssim P_{\text{spin}}/\tau$ phase bins, where $\tau = 2.048$ s (CONT data) or 1.024 s (DISCLA data) and P_{spin} is determined from overresolved power spectra or from folding, as discussed in § B1. A running average pulse profile is constructed by aligning each day's profile with and adding it to the existing running sum, weighted by its exposure (area times exposure time). Alignment is performed by maximizing the cross correlation between the daily profile and the running sum or using the cross spectrum (see Koh et al. 1997). The end result is an average profile in each energy channel (for DISCLA, we use only channel 1). Channels with a significant detection are used for spectral fitting. Prior to fitting, the profiles are Fourier transformed, and all harmonics higher than $n_H \sim 6$ set to zero to reduce the counting noise (see Deeter & Boynton 1986) and then inverse transformed. The rate in the minimum phase bin is subtracted from each bin, and the resulting rates are averaged to obtain the pulsed count rate in each energy channel.

In the following discussion, we denote the intrinsic strength of the pulsar signal as s , and the amplitude we measure as a . If the signal-to-noise ratio is low, then the measured amplitude, a , of the pulsar signal, s , is significantly biased by the measurement noise, n , such that $\langle a \rangle > s$. To account for this bias and rigorously estimate the measurement uncertainty, we use the probability distribution of the measured amplitude (Thomas 1969; Goodman 1985)

$$p(a | s, n) = \frac{2a}{n^2} \exp \left[\frac{-(a^2 + s^2)}{n^2} \right] I_0 \left(\frac{2as}{n^2} \right) \quad (a > 0), \quad (\text{B5})$$

where I_0 is the zeroth-order Bessel function of the first kind. This can be inverted to yield the probability distribution of s (Chakrabarty 1996):

$$p(s | a, n) = \frac{2}{n} \sqrt{\frac{1}{\pi}} \exp \left[\frac{-(a^2 + 2s^2)}{2n^2} \right] \frac{I_0(2as/n^2)}{I_0(a^2/2n^2)} \quad (s > 0). \quad (\text{B6})$$

If $a \gg n$, the probability distribution approaches a Gaussian with variance $\sigma^2 = n^2/2$. Because the noise varies with time and energy, we determine n separately for each energy channel by averaging the power in frequencies in the vicinity of the dominant harmonic in each of the daily power spectra of all days used to construct the average profile.

We determine the incident spectrum by folding standard models through the detector response matrix and varying the model parameters to fit the pulsed count rate in each energy channel. Pendleton et al. (1995) have computed BATSE detector response matrices as a function of viewing angle, θ . The energy edges of the CONT channels are independent of θ but vary with detector (see Fig. 40). Because a single average profile may contain data from multiple spacecraft orientations (a typical viewing period lasts 1–2 weeks), we compute an average response matrix and average channel edges for the spectral fitting. A photon power-law model, $dN/dE = C_{30}(E/30 \text{ keV})^{-\alpha}$, and an exponential (EXP) model, $dN/dE = C_0/E \exp(-E/E_f)$, provide reasonable fits to the data. In most cases the EXP model is superior.

An alternative to aligning and averaging daily profiles is to perform a *long coherent fold*. This is possible only for consistently bright, noneclipsing systems in which gaps in the data are short compared with the decoherence timescale or in which the torque history is smooth. Spectra have been constructed for 4U 1626–67 and GX 1+4 in such a way (Chakrabarty et al. 1997a, 1997b).

On-peak minus off-peak pulsed spectra and flux.—In another approach to pulsed flux estimation, 5–10 days of CONT data are folded using a phase model determined by fitting pulse phases measured using epoch-folded DISCLA data. An “on-pulse” and “off-pulse” phase interval are chosen by eye, and the average rate in the off-pulse interval is subtracted from each phase bin, which yields a rate differences in each energy channel for each phase bin.

B2.3. *Daily RMS Flux*

Unlike profiles constructed from intervals of 10–200 days, daily profiles have low S/N for most sources most of the time. Rather than attempting to fit a spectral model, we generally assume a spectral shape and determine the normalization. Although we use an exponential model in some cases and a power law in others, daily flux histories are not particularly sensitive to the choice of model.

Daily RMS flux from CONT and DISCLA data.—For most sources, an rms flux, F_{RMS} , is estimated daily by constructing pulse profiles in flux units. First, the average rate is subtracted from the folded profile from each detector and energy channel.

Next, each phase bin, ϕ , of each daily pulse profile for each exposed detector and energy channel is modeled as a phase-dependent exponential spectrum

$$F(E, \phi) = F_0(\phi)(E_0/E) \exp [-(E - E_0)/E_f], \quad (\text{B7})$$

where $F_0(\phi)$ is the flux at E_0 , which depends upon phase, and where E_f is assumed independent of phase. The e -folding energy is not adjusted in the daily fits but rather is taken from longer term analysis. The flux as a function of phase is parameterized in terms of a small number m (three to six) of Fourier amplitudes:

$$F_0(\phi) = F_0^{\text{avg}} + \sum_{k=1}^m [A_k \cos(2\pi k\phi) + B_k \sin(2\pi k\phi)], \quad (\text{B8})$$

with the Fourier coefficients A_k and B_k determined in the fit. Finally, the rms flux F_{rms} is determined as

$$F_{\text{RMS}} = \left[0.5 \sum_{k=1}^m (A_k^2 + B_k^2) \right]^{1/2}. \quad (\text{B9})$$

This procedure assumes that the pulse shape is independent of energy, which is not in general true. Fluxes in the data sets at the COSSC are determined using this procedure.

Flux histories have been determined for 4U 1626–67 and GX 1+4 by computing 1–5 day power spectra of the X-ray light curves in DISCLA channel 1 and using the amplitude of the dominant harmonic, in both cases the fundamental, to estimate the pulsed amplitude. The flux is determined by convolving either a power-law or exponential model with the detector response matrix, assuming a power-law index or e -folding energy. This technique assumes a constant spectral shape and pulse profile and can be used with nonsinusoidal profiles by computing a correction factor between the amplitude of the dominant harmonic and the pulsed flux.

Frequencies and fluxes from PSR data.—PSR data were used in the analysis of GRO J1744–28 because of its short 0.467 s pulse period. As well as data collected explicitly for GRO J1744–28, all applicable PSR data that were collected in a single-sweep mode (with no folding on board) were used. On the ground, the 20–40 keV rates from these data were divided into intervals of ~ 200 s. For each interval, an empirical background model quadratic in time was fitted to the rates and subtracted. Then the rates in each interval were fit with a sixth-order Fourier pulse model. These (harmonically represented) profiles were then combined over ~ 0.5 day intervals using a phase model, obtained by bootstrapping. The frequencies shown in § 4 were obtained by fitting pulse phase measurements based on these profiles. To obtain fluxes, a conversion factor from pulsed count rate to pulsed flux was calculated with the detector response matrices by assuming a spectral form $dN/dE = AE^{-2} \exp(-E/E_{\text{fold}})$ with $E_{\text{fold}} = 15$ keV.

REFERENCES

- Alpar, M. A., Ruderman, M. A., Cheng, A. F., & Shaham, J. 1982, *Nature*, 300, 728
- Alpar, M. A. & Shaham, J. 1985, *Nature*, 316, 239
- Anzer, U., & Borner, G. 1980, *A&A*, 83, 133
- Aoki, T., et al. 1992, *PASJ*, 44, 641
- Apparao, K. M. V. 1994, *Space Sci. Rev.*, 69, 255
- Arons, J. 1993, *ApJ*, 408, 160
- Arons, J., Burnard, D., Klein, R. I., McKee, C. F., Pudritz, R. E., & Lea, S. M. 1984, in *High Energy Transients in Astrophysics*, ed. S. E. Woosley (New York: AIP), 215
- Arons, J., & Lea, S. M. 1976, *ApJ*, 207, 914
- . 1980, *ApJ*, 235, 1016
- Baykal, A., & Ögelman, H. 1993, *A&A*, 267, 119
- Baykal, A., & Swank, J. 1996, *ApJ*, 460, 470
- Bhattacharya, D., & Srinivasan, G. 1995, in *X-Ray Binaries*, ed. W. H. G. Lewin, J. Van Paradijs, & E. P. J. van den Heuvel (Cambridge: Cambridge Univ. Press), 495
- Bianchi, L., & Bernacca, P. L. 1980, *A&A*, 89, 214
- Bildsten, L., Chakrabarty, D., Chiu, J., Finger, M. H., Grunsfeld, J. M., Koh, T., Prince, T. A., & Wilson, R. B. 1994, in *Second Compton Symposium*, ed. N. Gehrels, C. E. Fichtel, & J. P. Norris (New York: AIP), 290
- Blondin, J. M., Stevens, I. R., & Kallman, T. R. 1991, *ApJ*, 371, 684
- Brandt, N., & Podsiadlowski, P. 1995, *A&A*, 274, 461
- Buccheri, R., et al. 1983, *A&A*, 128, 245
- Chakrabarty, D. 1996, Ph.D. thesis, California Inst. of Technology
- . 1998, *ApJ*, in press
- Chakrabarty, D., et al. 1993, *ApJ*, 403, L33
- . 1997a, *ApJ*, 474, 414
- . 1997b, *ApJ*, 481, L101
- Chakrabarty, D., Bildsten, L., Chiu, J., Grunsfeld, J. M., Koh, T., Prince, T. A., Finger, M. H., & Wilson, R. B. 1994a, in *Second Compton Symposium*, ed. C. E. Fichtel, N. Gehrels, & J. P. Norris (New York: AIP), 285
- Chakrabarty, D., Koh, T., Bildsten, L., Prince, T. A., Finger, M. H., Wilson, R. B., Pendleton, G. N., & Rubin, B. C. 1995a, *ApJ*, 446, 826
- Chakrabarty, D., Koh, T., Prince, T. A., Vaughan, B., Finger, M. H., Scatt, M., & Wilson, R. B. 1995b, *IAU Circ.* 6153
- Chakrabarty, D., Prince, T. A., Finger, M. H., & Wilson, R. B. 1994b, *IAU Circ.* 6105
- Chakrabarty, D., & Roche, P. 1997, *ApJ*, 489, 254
- Chevalier, C., & Ilovaisky, S. A. 1975, *IAU Circ.* 2778
- Clark, J. S., et al. 1997, in preparation
- Coe, M. J., et al. 1994a, *MNRAS*, 270, L57
- . 1994b, *A&A*, 289, 784
- Coe, M. J., Carpenter, G. F., Engel, A. R., & Quenby, J. J. 1975, *Nature*, 256, 630
- Coe, M. J., Longmore, A., Payne, B. J., & Hanson, C. G. 1988, *MNRAS*, 232, 865
- Cohen, M. 1995, *ApJ*, 444, 874
- Cominsky, L., Clark, G. W., Li, F., Mayer, W., & Rappaport, S. 1978, *Nature*, 273, 367
- Cominsky, L., Roberts, M., & Finger, M. 1994, in *Second Compton Symposium*, ed. C. E. Fichtel, N. Gehrels, & J. P. Norris (New York: AIP), 294
- Cominsky, L., et al. 1997, in preparation
- Cook, M. C., & Page, C. G. 1987, *MNRAS*, 225, 381
- Cook, M. C., & Warwick, R. S. 1987, *MNRAS*, 225, 369
- Corbet, R. H. D. 1986, *MNRAS*, 220, 1047
- Corbet, R. H. D., Woo, J. W., & Nagase, F. 1993, *A&A*, 276, 52
- Crampton, D., Hutchings, J. B., & Cowley, A. P. 1978, *ApJ*, 225, L63
- Davidson, A., Malina, R., & Bowyer, S. 1977, *ApJ*, 211, 866
- Davidson, K., & Ostriker, J. P. 1973, *ApJ*, 179, 585
- Davidson, P. J. N., Watson, M. G., & Pye, J. P. 1977, *MNRAS*, 181, 73P
- Dean, A. J., Lei, F., & Knight, P. J. 1991, *Space Sci. Rev.*, 57, 109
- Deeter, J. E. 1981, Ph.D. thesis, Univ. of Washington
- . 1984, *ApJ*, 281, 482
- Deeter, J. E., & Boynton, P. E. 1986, in *Proc. of Inuyama Workshop on the Timing Studies of X-Ray Sources*, ed. S. Hayakawa & F. Nagase (Nagoya: Nagoya Univ.), 29
- Deeter, J. E., Boynton, P. E., Lamb, F. K., & Zylstra, G. 1989, *ApJ*, 336, 376
- Deeter, J. E., Boynton, P. E., Miyamoto, S., Kitamoto, S., Nagase, F., & Kawai, N. 1991, *ApJ*, 383, 324
- Deeter, J. E., Boynton, P. E., & Pravdo, S. H. 1981, *ApJ*, 247, 1003
- Deeter, J. E., Boynton, P. E., Shibasaki, N., Hayakawa, S., Nagase, F., & Sato, N. 1987, *AJ*, 93, 887

- de Kool, M., & Anzer, U. 1993, *MNRAS*, 262, 726
- de Vaucouleurs, G., & Pence, W. D. 1978, *AJ*, 83, 1163
- Dotani, T., Fujimoto, R., Nagase, F., & Inoue, H. 1995, *IAU Circ.*, 6241
- Dower, R. G., Apparao, K. M. V., Bradt, H. V., Doxsey, R. E., Jernigan, J. G., & Kulik, J. 1978, *Nature*, 273, 364
- Doxsey, R., Bradt, H. V., Levine, A., Murthy, G. T., Rappaport, S., & Spada, G. 1973, *ApJ*, 182, L25
- Elsner, R. F., Ghosh, P., & Lamb, F. K. 1980, *ApJ*, 241, L155
- Elsner, R. F., & Lamb, F. K. 1977, *ApJ*, 215, 897
- Finger, M. H., et al. 1995, *IAU Circ.* 6266
- Finger, M. H., Cominsky, L. R., Wilson, R. B., Harmon, B. A., & Fishman, G. J. 1994a, in *The Evolution of X-Ray Binaries*, ed. S. S. Holt & C. S. Day (New York: AIP), 459
- Finger, M. H., Koh, D. T., Nelson, R. W., Prince, T. A., Vaughan, B. A., & Wilson, R. B. 1996a, *Nature*, 381, 291
- Finger, M. H., Wilson, R. B., & Chakrabarty, D. 1996b, *A&AS*, 120, C209
- Finger, M. H., Wilson, R. B., & Fishman, G. J. 1994b, in *Second Compton Symposium*, ed. C. E. Fichtel, N. Gehrels, & J. P. Norris (New York: AIP), 304
- Finger, M. H., Wilson, R. B., & Harmon, B. A. 1996c, *ApJ*, 459, 288
- Finger, M. H., Wilson, R. B., Harmon, B. A., Fishman, G. J., Meegan, C. A., & Paciasas, W. S. 1993, in *Compton Gamma Ray Observatory*, ed. M. Friedlander, N. Gehrels, & D. J. Macomb (New York: AIP), 386
- Finger, M. H., Wilson, R. B., Meegan, C. A., Paciasas, W. S., & Fishman, G. J. 1992, in *Compton Observatory Science Workshop*, ed. C. R. Shrader, N. Gehrels, & B. Dennis (NASA CP-3137) (Washington: NASA), 185
- Finger, M. H., et al. 1997, in preparation
- Fishman, G. J., et al. 1989, in *Proc. of the GRO Science Workshop*, ed. W. N. Johnson (Greenbelt: NASA/GSFC), 2-39
- Fryxell, B. A., & Taam, R. E. 1988, *ApJ*, 335, 862
- Ghosh, P., & Lamb, F. K. 1979, *ApJ*, 234, 296
- Giacconi, R., Gursky, H., Kellogg, E., Levinson, R., Schreier, E., & Tananbaum, H. 1973, *ApJ*, 184, 227
- Giacconi, R., Gursky, H., Kellogg, E., Schreier, E., & Tananbaum, H. 1971, *ApJ*, 167, L67
- Giovannelli, F., & Graziati, L. S. 1992, *Space Sci. Rev.*, 59, 1
- Goodman, J. W. 1985, *Statistical Optics* (New York: Wiley)
- Gottwald, M., Steinle, H., Graser, U., & Pietsch, W. 1991, *A&AS*, 89, 367
- Grindlay, J. E., Petro, L. D., & McClintock, J. E. 1984, *ApJ*, 276, 621
- Grove, J. E. 1995, *IAU Circ.* 6239
- Grove, J. E., et al. 1993, *IAU Circ.* 5838
- . 1995, *ApJ*, 438, L25
- Haberl, F., Pietsch, W., Motch, C., & Buckley, D. A. H. 1996, *IAU Circ.* 6445
- Hammerschlag-Hensberge, G., et al. 1980, *A&A*, 85, 119
- Harmon, B. A., et al. 1992, in *Compton Observatory Science Workshop*, ed. C. R. Shrader, N. Gehrels, & B. Dennis (NASA CP-3137) (Washington: NASA), 69
- Hayakawa, S. 1985, *Phys. Rep.*, 121, 317
- Heinze, K. G. 1976, *ApJS*, 30, 491
- Hellier, C. 1994, *IAU Circ.* 5994
- Hiltner, W. A., Werner, J., & Osmer, P. 1972, *ApJ*, 175, L19
- Horack, J. M. 1991, *Development of the Burst and Transient Source Experiment (BATSE)* (NASA Ref. Pub. 1268) (Washington: NASA)
- Hughes, J. P. 1994, *ApJ*, 427, L25
- Hutchings, J. B., Bernard, J. E., Crampton, D., & Cowley, A. P. 1978, *ApJ*, 223, 530
- Hutchings, J. B., Cowley, A. P., Crampton, D., van Paradijs, J., & White, N. E. 1979, *ApJ*, 229, 1079
- Illarionov, A. F., & Sunyaev, R. A. 1975, *A&A*, 39, 185
- Ilovaisky, S. A., Chevalier, C., & Motch, C. 1982, *A&A*, 114, L7
- Israel, G. L., Mereghetti, S., & Stella, L. 1994, *ApJ*, 433, L25
- Israel, G. L., Stella, L., Angelini, L., White, N. E., & Giommi, P. 1995, *IAU Circ.* 6277
- Ives, J. C., Sanford, P. W., & Bell-Burnell, S. J. 1975, *Nature*, 254, 578
- Iwasawa, K., Koyama, K., & Halpern, J. P. 1992, *PASJ*, 44, 9
- Johns, M., Koski, A., Canizares, C., & McClintock, J. 1978, *IAU Circ.* 3171
- Johnston, S., et al. 1992, *ApJ*, 387, L37
- Joss, P. C., & Rappaport, S. A. 1984, *ARA&A*, 22, 537
- Kalogera, V. 1996, *ApJ*, 471, 352
- Kaper, L., Lamers, H. J. G. L. M., Ruymaekers, E., van den Heuvel, E. P. J., & Zuiderwijk, E. J. 1995, *A&A*, 300, 446
- Kaspi, V. M., Johnston, S., Bell, J. F., Manchester, R. N., Bailes, M., Bessell, M., Lyne, A. G., & D'Amico, N. 1994, *ApJ*, 423, L43
- Kelley, R. L., Apparao, K. M. V., Doxsey, R. E., Jernigan, J. G., Naranan, S., & Rappaport, S. 1981a, *ApJ*, 243, 251
- Kelley, R. L., Rappaport, S., & Ayasli, S. 1983, *ApJ*, 274, 765
- Kelley, R. L., Rappaport, S., Brodheim, M. J., Cominsky, L., & Strothers, R. 1981b, *ApJ*, 251, 630
- Kelley, R. L., Rappaport, S., Clark, G. W., & Petro, L. D. 1983, *ApJ*, 268, 790
- King, A. R., Kolb, U., & Burderi, L. 1996, *ApJ*, 464, L127
- Koh, D. T., et al. 1997, *ApJ*, 479, 933
- Koh, T., Chakrabarty, D., Prince, T. A., Vaughan, B. A., Zhang, S. N., Scott, M., Finger, M. H., & Wilson, R. B. 1995, *IAU Circ.* 6222
- Königl, A. 1991, *ApJ*, 370, L39
- Kouveliotou, C., van Paradijs, J., Fishman, G. J., Briggs, M. S., Kommers, J., Harmon, B. A., Meegan, C. A., & Lewin, W. H. G. 1996, *Nature*, 379, 799
- Koyama, K., et al. 1991a, *ApJ*, 366, L19
- Koyama, K., Kawada, M., Takeuchi, Y., Tawara, Y., Ushimaru, N., Dotani, T., & Takizawa, M. 1990a, *ApJ*, 356, L47
- Koyama, K., Kunieda, H., Takeuchi, Y., & Tawara, Y. 1990b, *PASJ*, 42, L59
- Koyama, K., Kunieda, H., Takeuchi, Y., & Tawara, Y. 1991b, *ApJ*, 370, L77
- Kriss, G. A., Cominsky, L. R., Remillard, R. A., Williams, G., & Thorstensen, J. R. 1983, *ApJ*, 266, 806
- Krzeminski, W. 1974, *ApJ*, 192, L135
- Lamb, F. K., Pethick, C. J., & Pines, D. 1973, *ApJ*, 184, 271
- Lamb, F. K., Pines, D., & Shaham, J. 1978, *ApJ*, 224, 969
- Lamb, F. K., Shibazaki, N., Alpar, M. A., & Shaham, J. 1985, *Nature*, 317, 681
- Lapshov, I. Y., Drenim, V. V., Sunyaev, R. A., Brandt, S., & Lund, N. 1992, *Soviet Astron. Lett.*, 18, 12
- Levine, A., Ma, C. P., McClintock, J., Rappaport, S., van der Klis, M., & Verbunt, F. 1988, *ApJ*, 327, 732
- Levine, A., Rappaport, S., Deeter, J. E., Boynton, P. E., & Nagase, F. 1993, *ApJ*, 410, 328
- Levine, A., Rappaport, S., Putney, A., Corbet, R., & Nagase, F. 1991, *ApJ*, 381, 101
- Lewin, W. H. G., Ricker, G. R., & McClintock, J. E. 1971, *ApJ*, 169, L17
- Lovelace, R. V. E., Romanova, M. M., & Bisnovatyi-Kogan, G. S. 1995, *MNRAS*, 275, 244
- Lund, N., Brandt, S., & Castro-Tirado, A. J. 1994, *IAU Circ.* 5448
- Lyne, A. G., & Lorimer, D. R. 1994, *Nature*, 369, 127
- Makishima, K., et al. 1988, *Nature*, 333, 746
- Makishima, K., Kawai, N., Koyama, K., Shibazaki, N., Nagase, F., & Nakagawa, M. 1984, *PASJ*, 36, 679
- Makishima, K., Koyama, K., Hayakawa, S., & Nagase, F. 1987, *ApJ*, 314, 619
- McClintock, J. E., et al. 1976, *ApJ*, 206, L99
- McClintock, J. E., Canizares, C. R., Bradt, H. V., Doxsey, R. E., Jernigan, J. G., & Hiltner, W. A. 1977, *Nature*, 270, 320
- Mereghetti, S., & Stella, L. 1995, *ApJ*, 442, L17
- Meurs, E. J. A., & van den Heuvel, E. P. J. 1989, *A&A*, 226, 88
- Middleditch, J. 1976, Ph.D. thesis, Univ. of California, Berkeley
- Middleditch, J., Mason, K. O., Nelson, J. E., & White, N. E. 1981, *ApJ*, 244, 1001
- Middleditch, J., & Nelson, J. 1976, *ApJ*, 208
- Mihara, T. 1995, Ph.D. thesis, Univ. of Tokyo
- Miller, G. E., & Scalo, J. M. 1979, *ApJS*, 41, 513
- Motch, C., Stella, L., Janot-Pacheco, E., & Mouchet, M. 1991, *ApJ*, 369, 490
- Murakami, T., Ikegami, T., Inoue, H., & Makishima, K. 1987, *PASJ*, 39, 253
- Nagase, F. 1989, *PASJ*, 41, 1
- Nagase, F., et al. 1982, *ApJ*, 263, 814
- Nagase, F., Corbet, R. H. D., Day, C. S. R., Inoue, H., Takeshima, T., Yoshida, K., & Mihara, T. 1992, *ApJ*, 396, 147
- Ostriker, E. C., & Shu, F. H. 1995, *ApJ*, 447, 813
- Papaloizou, J., & Pringle, J. E. 1977, *MNRAS*, 181, 441
- Parkes, G. E., Mason, K. O., Murdin, P. G., & Culhane, J. L. 1980, *MNRAS*, 191, 547
- Parkes, G. E., Murdin, P. G., & Mason, K. O. 1978, *MNRAS*, 184, 73P
- Parmar, A. N., White, N. E., & Stella, L. 1989, *ApJ*, 338, 373
- Parmar, A. N., White, N. E., Stella, L., Izzo, C., & Ferri, P. 1989, *ApJ*, 338, 359
- Patterson, J. 1994, *PASP*, 106, 209
- Pendleton, G. N., et al. 1995, *Nucl. Instrum. Methods A*, 364, 567
- Petre, R., & Gehrels, N. 1993, *IAU Circ.* 5877
- Pravdo, S. H., Day, C. S. R., Angelini, L., Harmon, B. A., Yoshida, A., & Saraswat, P. 1995, *ApJ*, 454, 872
- Preece, R. D., Pendleton, G. N., Briggs, M. S., Mallozzi, R. S., Paciasas, W. S., Band, D. L., Matteson, J. L., & Meegan, C. A. 1997, *ApJ*, submitted
- Priedhorsky, W. C., & Terrell, J. 1983, *ApJ*, 273, 709
- Pringle, J. E., & Rees, M. J. 1972, *A&A*, 21, 1
- Rappaport, S., Clark, G. W., Cominsky, L., Joss, P. C., & Li, F. 1978, *ApJ*, 224, L1
- Rappaport, S., & Joss, P. 1977a, *Nature*, 266, 123
- . 1977b, *Nature*, 266, 683
- Rappaport, S., Joss, P. C., & McClintock, J. E. 1976, *ApJ*, 206, L103
- Rappaport, S., Markert, T., Li, F. K., Clark, G. W., Jernigan, J. G., & McClintock, J. E. 1977, *ApJ*, 217, L29
- Rappaport, S., & van den Heuvel, E. P. J. 1997, in preparation
- Raubenheimer, B. C. 1990, *A&A*, 234, 172
- Ravenhall, D. G., & Pethick, C. J. 1994, *ApJ*, 424, 846
- Reynolds, A. P., Parmar, A. N., Stollberg, M. T., Verbunt, F., Roche, P., Wilson, R. B., & Finger, M. H. 1996, *A&A*, 312, 872
- Rickard, J. 1974, *ApJ*, 189, L113
- Ricketts, M. J., Hall, R., Page, C. G., & Pounds, K. A. 1981, *Space Sci. Rev.*, 30, 399

- Rosenberg, F. D., Eyles, C. J., Skinner, G. K., & Willmore, A. P. 1975, *Nature*, 256, 628
- Rossi, B., & Olbert, S. 1970, *Introduction to the Physics of Space* (New York: McGraw-Hill)
- Rubin, B. C., et al. 1994, in *Evolution of X-Ray Binaries*, ed. S. S. Holt & C. S. Day (New York: AIP), 455
- Rubin, B. C., et al. 1996, *A&AS*, 120(4), C687
- Rubin, B. C., Finger, M. H., Scott, D. M., & Wilson, R. B. 1997, *ApJ*, 488, 413
- Safi-Harb, S., Ögelman, H., & Dennerl, K. 1996, *ApJ*, 456, L37
- Sato, N., Nagase, F., Kawai, N., Kelley, R. L., Rappaport, S., & White, N. W. 1986, *ApJ*, 304, 241
- Sazonov, S., & Sunyaev, R. 1995, *IAU Circ.* 6272
- Schmidtke, P. C., Cowley, A. P., McGrath, T. K., & Anderson, A. L. 1995, *PASP*, 107, 450
- Schreier, E., Levinson, R., Gursky, H., Kellogg, E., Tananbaum, H., & Giacconi, R. 1972, *ApJ*, 172, L79
- Schwentker, O. 1994, *A&A*, 286, L47
- Scott, D. M., Finger, M. H., Wilson, R. B., Koh, D. T., Prince, T. A., Vaughan, B. A., & Chakrabarty, D. 1997, *ApJ*, 488, 831
- Scott, D. M., Finger, M. H., Wilson, R. B., & Prince, T. A. 1994, *IAU Circ.* 5990
- Scott, D. M., Finger, M. H., Wilson, R. B., Prince, T. A., & Vaughan, B. 1996, *IAU Circ.* 6450
- Seward, F. D., Charles, P. A., & Smale, A. P. 1986, *ApJ*, 305, 814
- Shore, S. N., Livio, M., & van den Heuvel, E. 1994, *Interacting Binaries* (Berlin: Springer)
- Skinner, G. K. 1981, *Space Sci. Rev.*, 30, 441
- Smak, J. 1983, *ApJ*, 272, 234
- Soong, Y., Gruber, D. E., Peterson, L. E., & Rothschild, R. E. 1990, *ApJ*, 348, 634
- Spruit, H. C., & Taam, R. E. 1993, *ApJ*, 402, 593
- Standish, E. M., Newhall, X. X., Williams, J. G., & Yeomans, D. K. 1992, in *Explanatory Supplement to the Astronomical Almanac*, ed. P. K. Seidelmann (Mill Valley: University Science), 279
- Stella, L., White, N. E., Davelaar, J., Parmar, A. N., Blissett, R. J., & van der Klis, M. 1985, *ApJ*, 288, L45
- Stella, L., White, N. E., & Rosner, R. 1986, *ApJ*, 308, 669
- Stier, M., & Liller, W. 1976, *ApJ*, 206, 257
- Stollberg, M. T., et al. 1993a, in *Compton Gamma-Ray Observatory*, ed. M. Friedlander, N. Gehrels, & D. J. Macomb (New York: AIP), 371
- Stollberg, M. T., Finger, M. H., Wilson, R. B., Harmon, B. A., Rubin, B. C., Zhang, N. S., & Fishman, G. J. 1993b, *IAU Circ.* 5836
- Stollberg, M. T., Paciesas, W. S., Finger, M. H., Fishman, G. J., Wilson, R. B., Harmon, B. A., & Wilson, C. A. 1994, in *The Evolution of X-Ray Binaries*, ed. S. S. Holt & C. S. Day (New York: AIP), 255
- Stollberg, M. T., Wilson, R. B., Finger, M. H., & Prince, T. A. 1996, *IAU Circ.* 6413
- Stollberg, M. T., et al. 1997, in preparation
- Strickman, M. S., et al. 1996, *ApJ*, 464, L131
- Strohmayer, T. E., et al. 1996, *ApJ*, 469, L9
- Taam, R. E., Fryxell, B. A., & Brown, D. A. 1988, *ApJ*, 331, L117
- Tamura, K., Tsunemi, H., Kitamoto, S., Hayashida, K., & Nagase, F. 1992, *ApJ*, 389, 676
- Tanaka, Y. 1993, *IAU Circ.* 5851
- Tananbaum, H., Gursky, H., Kellogg, E. M., Levinson, R., Schreier, E., & Giacconi, R. 1972, *ApJ*, 174, L143
- Tawara, Y., Yamauchi, S., Awaki, H., Kii, T., Koyama, K., & Nagase, F. 1989, *PASJ*, 41, 473
- Thomas, J. B. 1969, *Introduction to Statistical Communication Theory* (New York: Wiley)
- Tjemkes, S. A., Zuiderwijk, E. J., & van Paradijs, J. 1986, *A&A*, 154, 77
- van den Heuvel, E. P. J., & Rappaport, S. 1987, in *Physics of Be Stars*, ed. A. Slettebak & T. P. Snow (Cambridge: Cambridge Univ. Press), 291
- van Kerkwijk, M. H., van Paradijs, J., Zuiderwijk, E. J., Hammerschlag-Hensberge, G., Kaper, L., & Sterken, C. 1995, *A&A*, 303, 483
- van Paradijs, J. 1996, *ApJ*, 464, L139
- van Paradijs, J., & McClintock, J. E. 1995, in *X-Ray Binaries*, ed. W. H. G. Lewin, J. Van Paradijs, & E. P. J. van den Heuvel (Cambridge: Cambridge Univ. Press), 58
- Wang, Y. M. 1996, *ApJ*, 465, L111
- Warner, B. 1990, *Ap&SS*, 164, 79
- Waters, L. B. F. M., & van Kerkwijk, M. H. 1989, *A&A*, 223, 196
- Watson, M. G., Warwick, R. S., & Ricketts, M. J. 1981, *MNRAS*, 195, 197
- White, N. E., Mason, K. O., Huckle, H. E., Charles, P. A., & Sanford, P. W. 1976, *ApJ*, 209, L119
- White, N. E., Nagase, F., & Parmar, A. N. 1995, in *X-Ray Binaries*, ed. W. H. G. Lewin, J. Van Paradijs, & E. P. J. van den Heuvel (Cambridge: Cambridge Univ. Press), 1
- White, N. E., Parkes, G. E., Sanford, P. W., Mason, K. O., & Murdin, P. G. 1978, *Nature*, 274, 664
- White, N. E., & Pravdo, S. H. 1979, *ApJ*, 233, L121
- White, N. E., Swank, J. H., & Holt, S. S. 1983, *ApJ*, 270, 711
- Wilson, C. A., et al. 1995a, *IAU Circ.* 6238
- Wilson, C. A., Finger, M. H., Harmon, B. A., Scott, D. M., Wilson, R. B., Bildsten, L., Chakrabarty, D., & Prince, T. A. 1997, *ApJ*, 479, 388
- Wilson, C. A., Strohmayer, T., & Chakrabarty, D. 1996, *IAU Circ.* 6514
- Wilson, R. B., et al. 1992, *IAU Circ.* 5454
- . 1994a, in *Second Compton Symposium*, ed. C. E. Fichtel, N. Gehrels, & J. P. Norris (New York: AIP), 390
- . 1994b, in *Evolution of X-Ray Binaries*, ed. S. S. Holt & C. S. Day (New York: AIP), 451
- Wilson, R. B., Finger, M. H., Pendleton, G. N., Briggs, M., & Bildsten, L. 1994c, in *Evolution of X-Ray Binaries*, ed. S. S. Holt & C. S. Day (New York: AIP), 475
- Wilson, R. B., Finger, M. H., Pendleton, G. N., Briggs, M., & Bildsten, L. 1994d, in *Second Compton Symposium*, ed. C. E. Fichtel, N. Gehrels, & J. P. Norris (New York: AIP), 235
- Wilson, R. B., Finger, M. H., & Scott, D. M. 1994, *IAU Circ.* 5999
- Wilson, R. B., Zhang, S. N., Scott, M., Harmon, B. A., Koh, T., Chakrabarty, D., Vaughan, B., & Prince, T. A. 1995b, *IAU Circ.* 6207
- Wilson, R. B., et al. 1997, in preparation
- Wray, J. D. 1976, Ph.D. thesis, Northwestern Univ.